Development of a multichannel RF field detector for the Low-Level RF control of the Free-Electron Laser at Hamburg

Vom Promotionsausschuss der
Technischen Universität Hamburg-Harburg

zur Erlangung des akademischen Grades

Doktor-Ingenieur (Dr.-Ing.)

genehmigte Dissertation

von
Matthias Hoffmann

aus
Berlin

2008

for Rina

Zusammenfassung

Die in modernen Freien-Elektronen-Lasern erzeugte Synchrotronstrahlung mit immer kürzer werdender Wellenlänge von bis zu 6 nm und einer Pulsdauer von 100 fs erfordert eine immer höhere Stabilität der Energie und Ankunftszeit des Elektronenstrahls am Eingang des am Ende der Beschleunigungskette befindlichen Undulators. Gleichzeitig ergeben sich durch die immer weiter ansteigenden Geschwindigkeiten der digitalen Verarbeitungssysteme und Datenerfassung neue Möglichkeiten für die digitale Hochfrequenzregelung und Felddetektion.

In der vorliegenden Arbeit wird die Entwicklung eines Mehrkanalhochfrequenzfelddetektors für die Hochfrequenzregelung der supraleitenden Beschleunigungsstrukturen des Freien Elektronen Lasers in Hamburg (FLASH) beschrieben. Das hierfür verwendete Verfahren des IF Sampling gilt als bekannt und wird bereits in vielen Bereichen der digitalen Datenübertragung angewendet. Es soll hinsichtlich seiner Anwendbarkeit für die Hochfrequenzregelung untersucht werden.

Zur Bestimmung der Anforderungen an die Messgenauigkeit des zu entwickelnden Felddetektors wurden analytische und numerische Untersuchungen zum Rauschverhalten und -transport im Regelkreis durchgeführt. Hierzu wurden vereinfachte Modelle zum Rauschverhalten der einzelnen Systemkomponenten im Regelkreis, wie z.B. Verstärker, Hochfrequenzmischer und Analog-Digital-Wandler, aufgestellt und anschliessend als Modell des Regelkreises zusammengestellt.

Aufgrund der Anwendung einer Vektorsummenregelung, bei der mehrere einzeln gemessene Feldvektoren zu einer Vektorsumme addiert werden, ergeben sich Anforderungen bezüglich des zulässigen Kompressionsfehlers des Detektors durch Nichtlinearitäten, die ebenfalls analytisch und numerisch untersucht wurden.

Aus den Ergebnissen der Simulation wurden Spezifikationen für die zu entwickelnde Hardware aufgestellt. Bei der Entwicklung des Hochfrequenzfelddetektors wurde ein EMV-gerechtes, modulares Konzept mit einer rein passiven Eingangsstufe und den zur Verbesserung des Signal-Rausch-Abstandes benötigten hohen Signalpegeln zugrunde gelegt.

Die anschliessenden Tests im Labor ergaben für die Messgenauigkeit des Felddetektors die geforderten Werte, während die Linearität des Detektors ausserhalb der Spezifikation lag. Bei der Anwendung des Detektors im Regelkreis am Beschleuniger zeigten sich deutliche Abweichungen von den Messergebnissen im

Labor. Tieffrequentes Rauschen (1/f-Rauschen) des Detektors sowie des verwendeten Lokaloszillators verhindern eine Langzeitstabilisierung des Beschleunigungsfeldes.

Abstract

Modern free electron lasers produce synchrotron radiation with constantly shortening wavelengths of up to 6 nm and pulse widths of up to 100 fs. That requires a constantly increasing stability of the beam energy and arrival time of the electron beam at the undulator entrance which is situated at the end of the accelerator. At the same time, the increasing speed of digital signal processing and data acquisition facilitates new possibilities for the digital radio frequency control and field detection.

In this thesis the development of a multichannel radio frequency field detector for the low level radio frequency (LLRF) control of the superconducting cavities of the Free-Electron Laser at Hamburg (FLASH) is described. The applied method of IF sampling is state of the technology and is utilized in many areas of digital communication. It is evaluated concerning its applicability for the LLRF control.

Analytical and numerical investigations of the noise behavior and transport in the control loop have been accomplished to define the requirements for the measurement accuracy of the field detector that was to be developed. Therefore, simplified models of the noise behavior of each system component of the control loop, e.g. amplifier, radio frequency mixer and analog-to-digital converter, were established and subsequently assorted to a the model of the control loop.

Due to the application of the vectorsum control, where several separately measured field vectors are added to a vectorsum, requirements concerning the allowable compression error of the detector nonlinearity were defined. These were investigated by analytical and numerical methods, as well.

Requirements for the hardware that was to be developed were compiled from the simulation results. For the development of the field detector, a modular and EMC-compatible concept with a high-level passive front-end for an improvement of the signal-to-noise ratio was chosen.

The following tests in the lab delivered the required values for the measurement accuracy of the field detector, while the detector linearity was outside the specification. The application of the detector in the control loop at the accelerator showed noticable deviation from the measurement results reached in the lab. Low frequency noise (1/f-noise) of the detector and the used local oscillator generation set-up prevent a long time stabilization of the accelerating field.

Contents

Abbreviation List

3GEN	Three Generator Set-up
ACB	Analog Carrier Board
ACC	Accelerating Module
ADC	Analog to Digital Converter
AM	Amplitude Modulation
BAM	Beam Arrival Time Monitor
BC2	Bunch Compressor 2
BPM	Beam Position Monitor
CLK	Clock
DAC	Digital to Analog Converter
dBFS	Decibels Full Scale
DIV	Divider Set-up
DNL	Differential Nonlinearity
DRO	Dielectric Resonator Oscillator
DUT	Device Under Test
FFT	Fast Fourier Transform
FIR	Finite Impulse Response Filter
FLASH	Free-Electron Laser at Hamburg
FS	Full Scale
I	Inphase/Real Part
IF	Intermediate Frequency
ILC	International Linear Collider
IM3	Third-order Intermodualtion
IP3	Third-order Intercept Point related to the Input
IQ	Inphase and Quadrature
LCM	Least Common Multiple
LFD	Lorentz Force Detuning
LLRF	Low Level Radio Frequency
LO	Local Oscillator
LSB	Least Significant Bit
LTI	Linear Time-Invariant
MIMO	Multiple Input Multiple Output
MO	Master Oscillator

NF   Noise Figure
OIP3   Third-order Intercept Point related to the Output
PCB   Printed Circuit Board
PLL   Phase Locked Loop
PM   Phase Modulation
Q   Quadrature/Imaginary Part
RF   Radio Frequency
SASE   Self-Amplified Spontaneous Emission
SFDR   Spurious Free Dynamic Range
SNR   Signal to Noise Ratio
TESLA   TeV Energy Superconducting Linear Accelerator
TTF   TESLA Test Facility
VME   VERSA-module Europe
VUV-FEL   Vacuum Ultraviolet Free-Electron Laser
XFEL   X-Ray Free-Electron Laser

Chapter 1

Introduction

The necessity for a control of the high frequency electro-magnetic field of the superconductive cavity is deduced from the requirements of the accelerated electron beam. The energy stability of the electron beam is dependent on the stability of the accelerating voltage. The requirements of the energy stability and the peak current of the electron beam at the entrance of the undulator at the end of the accelerator originate from the dependency of the generation process of the x-ray (SASE) in the undulator on the beam energy and its distribution. Further requirements follow from the first bunch compression behind the injector at the beginning of the accelerator and from the required stability of the arrival-time of the laser pulses at the output of the undulator for experiments with an additional synchronized (pump-probe) laser.

The Free-Electron Laser at Hamburg (FLASH) is operated in a pulsed mode with gradients of the cavity field of up to $25\,\mathrm{MV/m}$ and an RF pulse length of $1\text{-}2\,\mathrm{ms}$ with a repetition rate of $5\text{-}10\,\mathrm{Hz}$. Due to Lorentz forces, which act onto the cavity wall caused by the high gradient of the pulsed RF field, mechanical deformations of the cavity occur. A gradient of $25\,\mathrm{MV/m}$ leads to mechanical deformation of $1\,\mu\mathrm{m}$ which corresponds to a change of the resonance frequency of one bandwidth of the cavity $(300\,\mathrm{Hz})$. These reversible mechanical deformation leads to predictable detuning of the resonance frequency of one bandwidth during one RF pulse. Microphonic effects cause stochastical and periodic detuning with a bandwidth of up to $1\,\mathrm{kHz}$, which result in pulse-to-pulse fluctuations of the center frequency. Changes of the resonance frequency lead to fluctuations of the accelerating voltage in amplitude and phase because of the fixed operating frequency at $1.3\,\mathrm{GHz}$ and the high loaded quality factor of the cavity of $3 \cdot 10^6$.

The beam requirements lead to a required stability of the accelerating voltage for the injector linac in front of the first bunch compressor of 10^{-4} (0.01%) in amplitude and $10^{-4}\,\mathrm{rad}$ $(0.01°)$ in phase.

The implemented Low-Level radio frequency (LLRF) control is a digital vectorsum control based on a driven feedback scheme, where the complex sum of 8 (up to 32) cavities is controlled by one LLRF system. The advantage of the

digital control is the possibility of a flexible configuration of control algorithms, like adaptive feedforward or implementation of a MIMO-controller and the calculation of the vectorsum. Disadvantages are the limited resolution of the required discretization by analog-to-digital converters and the latency of the digital system.

Due to microphonics in the range of 1°, a minimum feedback gain in the range of 100 is needed to reach the required stability of 0.01°. The required field stability demands a measurement accuracy of the field detector of 10^{-4} in amplitude and 0.01° in phase with the specific condition of the vectorsum control of 8 cavities. The limiting effects of the vectorsum control are the limited resolution of the analog-to-digital conversion, slow drifts of the phase shift in cables and detectors, and the calibration of the vectorsum. The application of a vectorsum control requires a higher linearity of the detector than the application of a single cavity control.

The subject-matter of this thesis is the development of a low noise and linear multi channel RF field detector to detect and control the vectorsum of the accelerating voltage of 8 cavities with an accuracy of 10^{-4} in amplitude and 0.01° in phase.

In chapter 2 a short summary of the LLRF system at FLASH is presented and an overview of the behavior of the superconductive cavity is given.

Because of the limited measurement accuracy of the field detector due to noise, models for the noise description of the control loop components are derived in the first part of chaper 3. Afterwards, a simplified model of the control loop is defined and simulations are done for investigations of the noise transport and behavior within the control loop. At the end of chapter 3, the impact of detector linearity on measurement accuracy is discussed, with the attention of the usage of a vectorsum control.

In chapter 4, the requirements for the RF field detector are determined, based on the required measurement accuracy and linearity. Feasible concepts for RF field detection are presented and compared. Furthermore an algorithm for a digital quadrature demodulation is presented.

The development of an RF field detector based on the IF sampling concept is presented in chapter 5. At the end of this chapter, a feasible optimization of the IF sampling detector is discussed.

Chapter 6 presents characterization and measurement results of the RF field detector presented in chapter 5. The characterization in the laboratory is focussed on the noise and linearity performance and the feasibility and applicability of the IF sampling scheme for the chosen operating frequencies. In the second part, the detector is used as multichannel field detector of the vectorsum control loop for one ACC-module at FLASH. To verify the quality of the field control with the new developed multichannel field detector, the stability of the accelerating voltage of the cavities and the energy stability of the electron beam are measured as function of the loop gain.

Chapter 2

LLRF System at FLASH

The linear accelerator of the Free-Electron Laser in Hamburg (FLASH), formerly known as Tesla Test Facility (TTF) or Vacuum Ultra Violet Free-Electron Laser (VUV-FEL), is used as a prototype and test facility for investigations and developments for the new European XFEL in Hamburg and the International Linear Collider (ILC). Furthermore FLASH is a user facility for research programs of medicine, biology, and material sience.
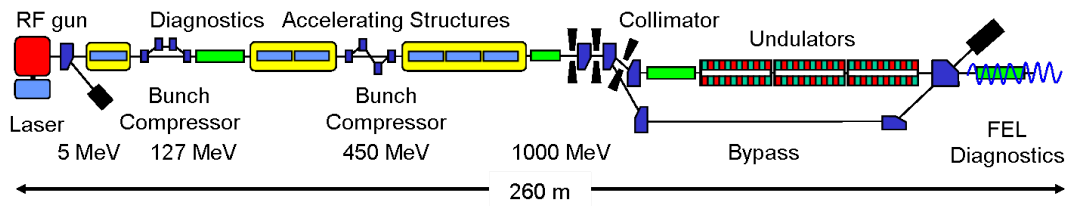

Figure 2.1: Layout of the FLASH facility

The layout of the FLASH facility is depicted in Fig. 2.1. In the RF gun, the electron bunches are generated by a pulsed laser which produces free electrons by the photo-effect. The pulsed laser is focussed on a photo cathode and liberates electrons with a repetition rate of $1\,\mathrm{MHz}$. The electrons are accelerated with a gradient of up to $45\,\mathrm{MV/m}$ in a $1\frac{1}{2}$-cell copper cavity. At the output of the RF gun, the energy of the electron bunches is up to $5\,\mathrm{MeV}$. In the following superconductive accelerating module (ACC-module), the electron bunches are accelerated 'off-crest' (section 2.5) to an energy of up to $127\,\mathrm{MeV}$ at field gradients ranging from 12 to $24\,\mathrm{MV/m}$ for adiabatic acceleration. Due to the 'off-crest' acceleration, an energy profile is impressed on the electron bunches, which is used to achieve a longitudinal compression within the bunch compressor (BC2), which leads to a peak current up to $2.5\,\mathrm{kA}$ [1]. Within the subsequent ACC-modules with field gradients of $25\,\mathrm{MV/m}$, the electron bunches can be accelerated to an energy of up to $1\,\mathrm{GeV}$. The interjacent diagnostic sections are used to measure parameters like energy, charge, arrival-time or shape of single bunches or bunch

trains, and to determine the influence of the properties on the ACC-modules to the measured beam parameters [2]. In the undulator, a structure with consecutive and alternating magnets, the pulsed laser light with a wavelength of down to 7 nm is generated by the SASE process [3]. The laser light is distributed to the experimental hall, where users from different research areas like material research, biology, or chemistry carry out their experiments [4].

2.1 The LLRF System

In the LLRF system at FLASH (Fig. 2.2), the vectorsum of the accelerating field vectors of the ACC-modules consisting of 8 (16, 24, or 32) superconducting nine cell resonators (cavities) has to be stabilized in amplitude and phase to a given set point. Therefore the electrical field vector of each single cavity is picked up with a probe antenna, converted to a lower intermediate frequency (IF) by an RF detector, and digitized in an analog-to-digital converter (ADC).

In the digital controller, the real and imaginary part of the individual field vector is calculated and calibrated by rotation matrices. A control algorithm compares the sum of the measured field vectors with a set point and calculates an error vector, which is minimized by changing the incident field vector of the cavities by an actuator. The actuator is an RF vector modulator, which is driven by the in-phase (I) and quadrature (Q) values generated by a digital-to-analog converter (DAC). At the controller output, an additional rotation matrix is implemented for loop phase und system gain adjustments. A high power chain with preamplifiers, klystron, and a waveguide distribution system provides the RF input for each cavity. For the high power phase adjustment, the incident phase of each single cavity can be changed separately by 3-stub tuners ([5]) in the waveguide distribution system, while the amplitude of each cavity is adjusted by the coupling.

A reference and timing system delivers the local oscillator signal for the RF detectors and actuator, the clock signal for the ADC and DAC, and the trigger signals for the synchronisation of different events in the system (switch on high voltage of the modulator, starting point of RF pulse, timing of the beam, etc.). Furthermore the reference distribution system provides a set of frequencies for the whole accelerator and experiments at the end of the machine (RF gun laser, pump-probe laser, diagnostic, etc.)[6].

The linac of the user facility FLASH is operated in a pulsed mode with an RF pulse width of 1300 μs and a repetition rate of 5 to 10 Hz. The pulse structure can be separated into three sections (Fig. 2.3), filling (500 μs), flat top (800 μs), and decay. During the filling, the cavity is driven by a constant generator forward power, while the cavity voltage increases exponentially. During the flat top, the cavity field is kept constant and the beam is injected into the ACC-modules. The electron beam is separated into 800 bunches with a repetition rate of 1 MHz. If
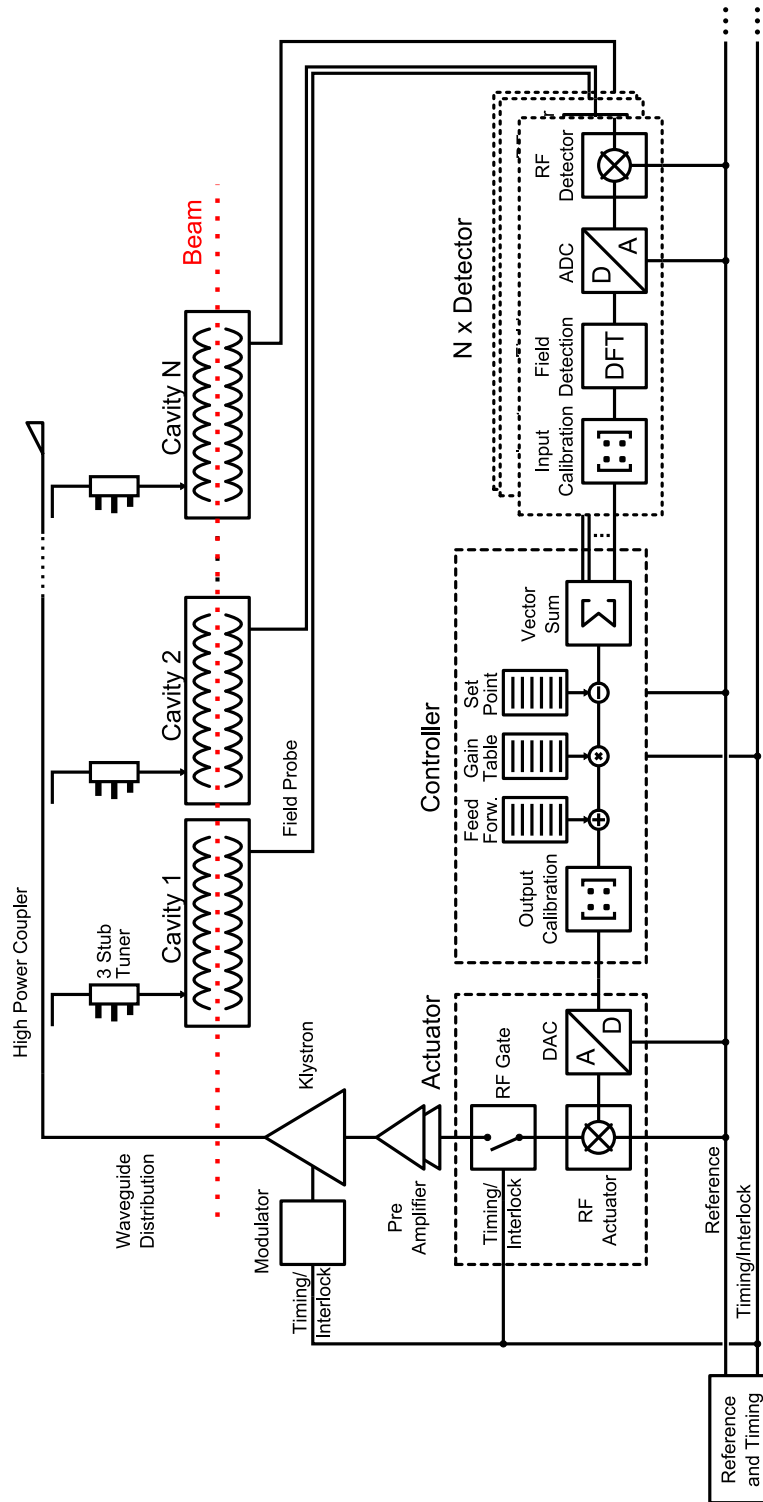
Figure 2.2: Functional block diagram of the LLRF system for the ACC-modules at FLASH
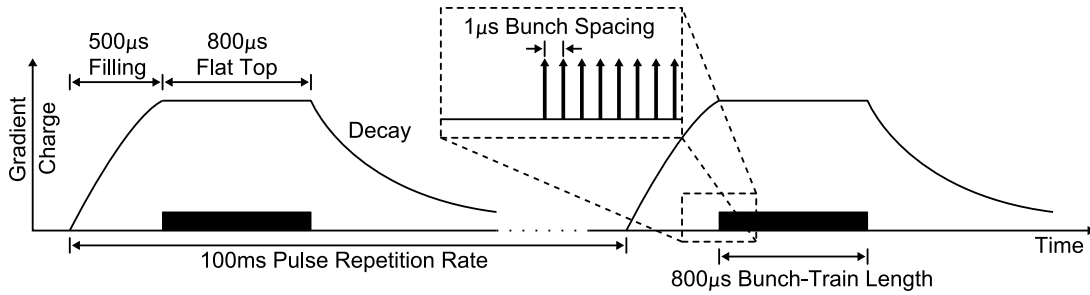
Figure 2.3: RF pulse structure with beam pattern

the beam is injected and accelerated, it extracts energy from the cavity field. For compensation, the forward power of the generator is increased to drive the cavity after each bunch has passed to the previous level. At the end of the pulse, the generator is switched off and the cavity field decays exponentially.

2.2   Vectorsum Control

The principle of vectorsum control is based on the fact that the energy gain of the beam is a result of the integral over the accelerating voltage along the accelerating route. This is emulated in the controller by measuring the field vector of each single cavity in one ACC-module and by calculating the vectorsum to get the accelerating voltage vector of the whole ACC-module. The control loop acts onto this vectorsum and keeps it constant, while each single cavity field within the vectorsum can fluctuate.

The vectorsum control has been chosen to reduce the cost for the LLRF system. One high power klystron (5 to 10 MW) and LLRF system for 8 or more cavities is significantly cheaper than one low power klystron (200 kW) and LLRF system for each cavity.

2.3   Nine Cell Resonator

The plant of the LLRF control loop is a nine cell resonator [7], called cavity, which can be modeled as parallel coupled LCR-circuits. Due to these coupled cells, the resonator has nine normal modes, called pass band modes (Fig 2.5), while each mode is named by the phase shift from cell to cell. The width of this pass band is around 30 MHz, while the highest mode is at 1.3 GHz, which is the accelerating mode. It is called π-mode, because the phase shift between two subsequent cells is $180° = \pi$. The next mode is the $8/9\pi$-mode, which is approximately 800 kHz below the π-mode.

As depicted in Fig. 2.6, the generator is coupled via a transmission line with reference impedance $Z_0 = 50\,\Omega$ and an ideal transformer, which models the high

Figure 2.4: Picture of the cavity

f_π = 1300.091 MHz

$f_{8/9\pi}$= 1299.260 MHz

$f_{7/9\pi}$= 1296.861 MHz

$f_{6/9\pi}$= 1293.345 MHz

$f_{5/9\pi}$= 1289.022 MHz

$f_{4/9\pi}$= 1284.409 MHz

$f_{3/9\pi}$= 1280.206 MHz

$f_{2/9\pi}$= 1276.435 MHz

$f_{1/9\pi}$= 1274.387 MHz
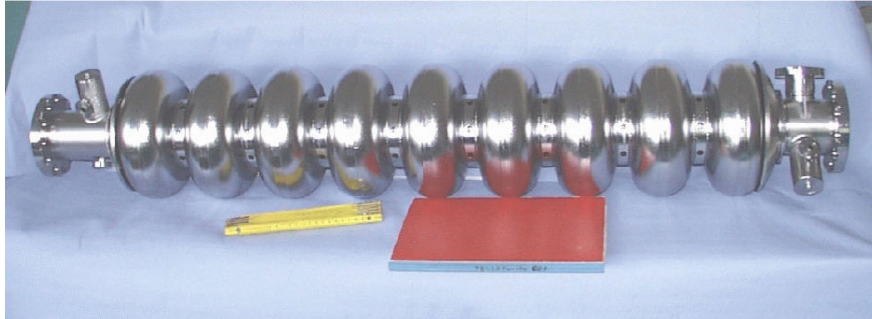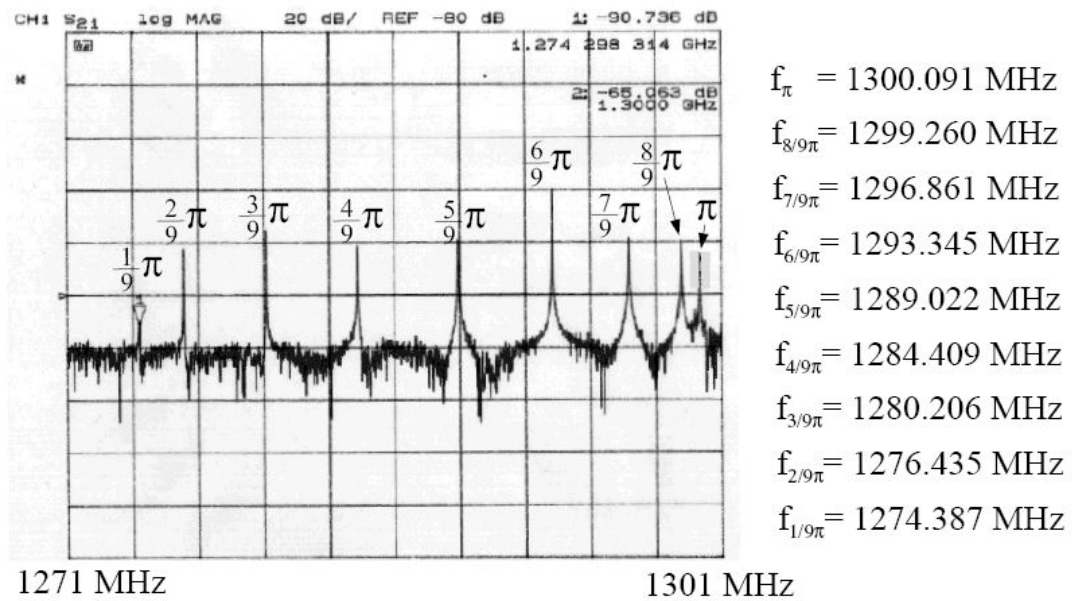
Figure 2.5: Spectrum of the pass band modes of the cavity. The π-mode is the accelerating mode for the beam.

power coupling from the waveguide to the cavity [8]. The coupling factor β is used to adjuste the efficient power transfer to the beam. It depends on the winding ratio N of the transformer.

$$\beta = \frac{R}{N^2 Z_0} = \frac{R}{Z_{\text{ext}}} \tag{2.1}$$

The cavity is loaded by an additional resistive load Z_{ext}.

$$\frac{1}{R_L} = \frac{1}{R} + \frac{1}{Z_{\text{ext}}} \tag{2.2}$$

For superconducting cavities with $Q_0 = 10^9 \gg Q_L$, the coupling factor β is in the range of 10^3 to 10^4. The beam is modeled as a current source. The cavity acts
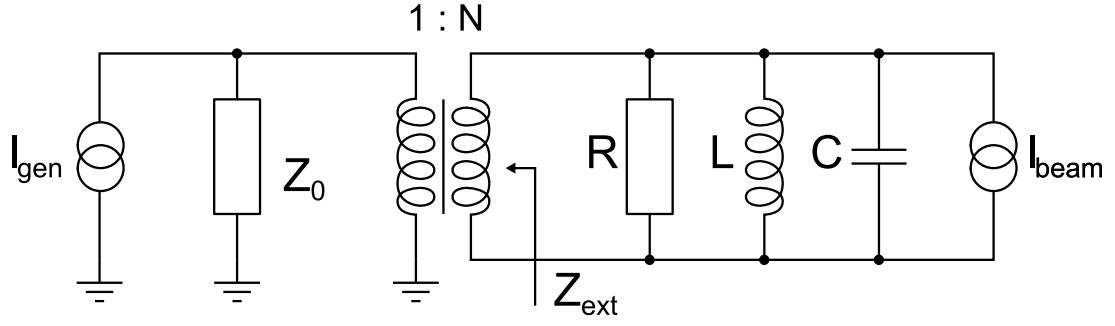
Figure 2.6: Coupling of the generator and beam to the equivalent circuit of the cavity.

as a high quality bandpass filter with a center frequency of $\omega_0 = 1.3\,\text{GHz}$ and a $3\,\text{dB}$-bandwidth of $\omega_{1/2} = 2\pi \cdot 216\,\text{Hz}$. The loaded quality factor is $Q_L = 3 \cdot 10^6$, which is determind by the coupling factor β.

$$Q_L = \frac{Q_0}{1 + \beta} \tag{2.3}$$

The differential equation of the LCR-resonant circuit

$$\ddot{V}(t) + \frac{1}{R_L C}\dot{V}(t) + \frac{1}{LC}V(t) = \frac{1}{C}\dot{I}(t) \tag{2.4}$$

delivers the amplitude and phase response

$$\hat{V} = \frac{R_L \hat{I}_0}{\sqrt{1 + \left[R_L \cdot \left(\frac{1}{\omega L} - \omega C\right)\right]^2}}$$

$$\Phi = \arctan\left(R_L \cdot \left(\frac{1}{\omega L} - \omega C\right)\right). \tag{2.5}$$

With the cavity bandwidth $\omega_{1/2}$ and the detuning $\Delta\omega = \omega_0 - \omega$, it can be simplified to express the gain and phase shift

$$
\begin{aligned}
G_V &= \frac{1}{\sqrt{1 + \left(\frac{\Delta\omega}{\omega_{1/2}}\right)^2}} \\
\Phi &= \arctan\frac{\Delta\omega}{\omega_{1/2}}
\end{aligned}
\tag{2.6}
$$

as function of the detuning $\Delta\omega$. Detuning is achieved by varying the resonance frequency ω_0 by mechanical disturbances instead of changing the generator frequency ω. The angle Φ is called the detuning angle.
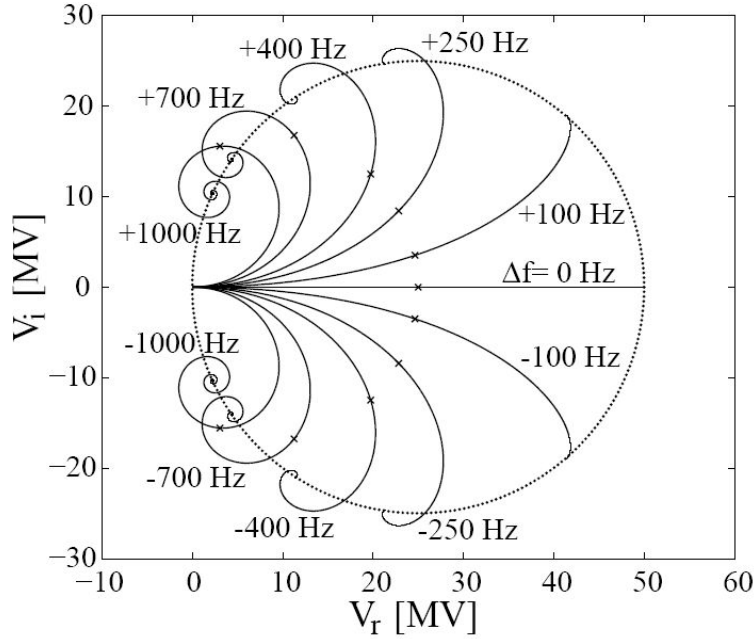
Figure 2.7: Transient behavior of a cavity with constant input power and different detuning $\Delta\omega$. V_r and V_i are the real and imaginary amplitude of the complex voltage vector. The dotted circle indicates the steady-state as function of the detuning angle Φ. [8]

Because the cavity is a high quality resonator, the transient behavior has to be considered. The derivation can be found in [8] and [9]. The results can be summarized in the state-space equation

$$
\frac{\mathrm{d}}{\mathrm{d}t}\begin{pmatrix} V_r \\ V_i \end{pmatrix} = \begin{pmatrix} -\omega_{1/2} & -\Delta\omega \\ \Delta\omega & -\omega_{1/2} \end{pmatrix} \cdot \begin{pmatrix} V_r \\ V_i \end{pmatrix} + \begin{pmatrix} R_L\omega_{1/2} & 0 \\ 0 & R_L\omega_{1/2} \end{pmatrix} \cdot \begin{pmatrix} I_r \\ I_i \end{pmatrix}
\tag{2.7}
$$

with the field vector of the cavity

$$
\vec{V} = \begin{pmatrix} V_r \\ V_i \end{pmatrix}
\tag{2.8}
$$

described by its real (r) and imaginary (i) part, and the driving current

$$\vec{I} = \begin{pmatrix} I_r \\ I_i \end{pmatrix} \tag{2.9}$$

which describes the generator and the beam current. Due to mechanical distur-
bances, the detuning $\Delta\omega$ in the first matrix is a function of time and dependent
on the amplitude of the field vector $\vec{V}$.

2.4   Mechanical Disturbances

Microphonics are mechanical vibrations which are acting onto the cavity, due to
the mechanical structure of the ACC-module. These disturbances originate from
different sources like vibrations of the vacuum and helium pumps, or ground
vibration due to traffic or ground motions. Because of the high quality of the
resonator, small vibrations are already visible as phase changes of the field vector
of the cavity. Vibrations are changing the geometric structure of the cavity and
therefore the resonance frequency. The time scale of these disturbances is up to
a few milliseconds, which results in RF pulse to pulse fluctuations [10].
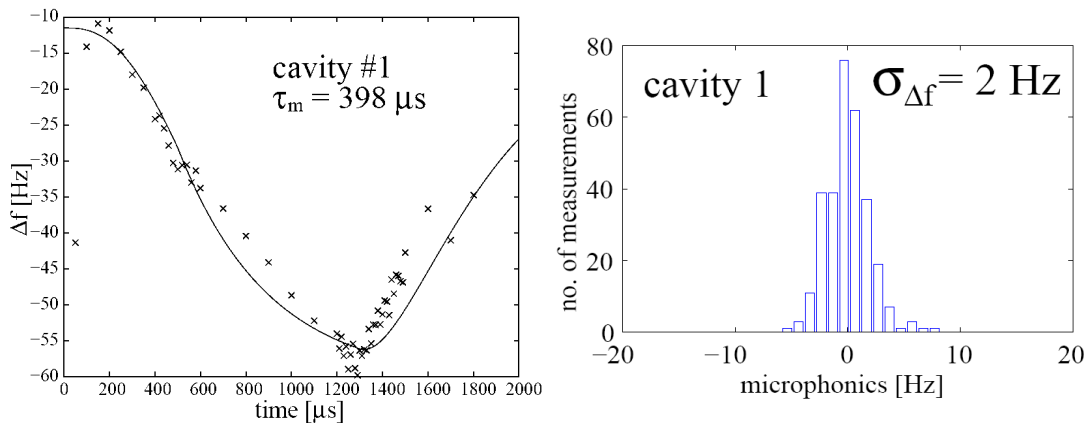
Figure 2.8: Detuning of the resonance frequency due to Lorentz force in one pulse
(measured and modeled)(right); Histogram of the detuning due to microphonics
from pulse to pulse (left); [8]

A further source of disturbance is the Lorentz-force detuning (LFD). While mi-
crophonics are stochastically distributed errors, LFD is strongly repetitive. Due
to the high electrical field strength in the resonator cells, the mechanical structure
of the cavity is deformed and therefore the resonance frequency is changed. A
gradient of $25\,\mathrm{MV/m}$ leads to mechanical deformation of $1\,\mu\mathrm{m}$ which corresponds
to a change of the resonance frequency of one bandwidth of the cavity ($300\,\mathrm{Hz}$).
For compensation of the detuning due to Lorentz force by the feedback loop, an

extra power of 25 % of the klystron is needed. The pulsed structure of the driving signal from the generator and a mathematical model of the deformation process allows to predict and compensate the detuning of the cavity due to Lorentz-force in the controller by adaptive feedforward [11], [9]. The microphonics are stochastical errors, which can only be reduced by the control loop.
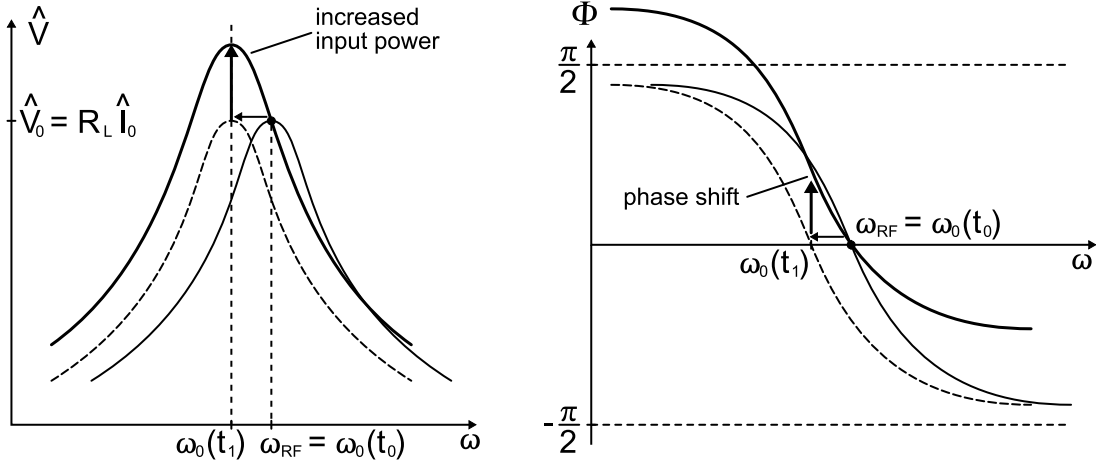

Figure 2.9: Principle of RF control. The change of the resonance frequency from $\omega_0(t_0)$ to $\omega_0(t_1)$ results in a decreasing amplitude at the operating frequency ω_{RF}. This is compensated by increasing the input power by the control system, while the phase at ω_{RF} has to be shifted, too. [8]

All these disturbances lead to a varying resonance frequency. As depicted in Fig. 2.9, the amplitude and phase of the cavity voltage change. The control loop has to reduce these changes by increasing the input power and/or changing the phase of the incident wave.

Another method to suppress the effects of Lorentz-force detuning is the utilization of an active vibration damping by a piezoelectric actuator. This actuator then acts during the RF pulse against the deformation of the cavity [12].

2.5 Acceleration of the Beam

The accelerating voltage which acts onto the beam consists of

$$V_{\mathrm{acc}}(t) = V_{\mathrm{cav}} \cdot \cos \varphi_b = V_{\mathrm{cav}} \cdot \cos(\omega t_b) \tag{2.10}$$

with the beam phase φ_b. It is defined by the time difference between the instants, when the field has its maximum and when the beam goes through the cavity. At a beam phase of $\varphi_b = 0°$, the beam passes the cavity when the gradient in the cavity is maximum. This point of maximal acceleration is called 'on-crest'. In the first module, the beam is accelerated 10° to 20° 'off-crest' to induce a bunch
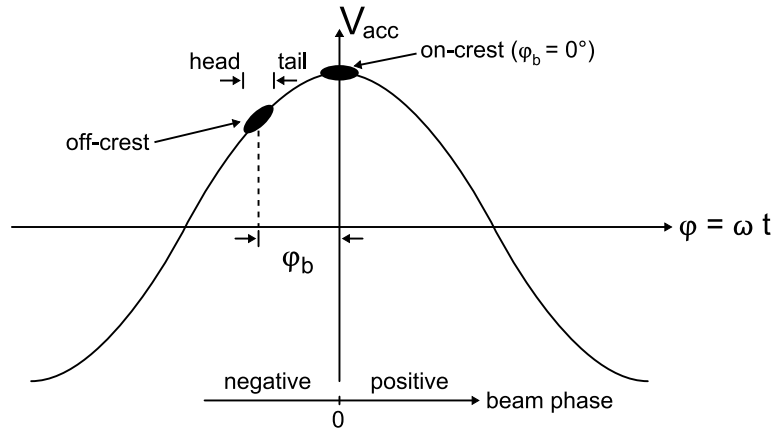
Figure 2.10: Definition of beam phase; on-crest and off-crest

energy profile which is required for a longitudinal compression of the bunch in the bunch compressor section. It is used to achieve the required high peak current of 2 kA [1]. Variations in the amplitude of the accelerating voltage lead to an intra bunch and bunch-to-bunch energy spread of the beam. With a beam phase of 10° to 20°, variations of the phase lead to an energy spread, too. An energy stability of $\sigma_E/E = 10^{-4}$ is required [9]. Additionally, the bunch arrival time at the end of the linac has to be stabilized down to variations of just 100 fs (the order of the bunch length) to guarantee a synchronization with a pump-probe laser for further experiments [13]. The required amplitude and phase stability of the vectorsum are 0.01 % and 0.01° respectively.

Chapter 3

Theoretical Background and Simulation

For an analysis of the noise sources of the LLRF system, a uniform description of noise generation and transport in the signal chain has to be found. Based on the noise theory for linear time invariant (LTI) systems and networks, a system level description for the noise transfer in the subsystems of the LLRF system is derived. A detailed short summary of the underlying theory can be found in textbooks about noise in LTI systems [14], [15]. Based on this description and on the basics of control theory, a system noise model of the simplified LLRF system for amplitude and phase noise is developed and applied to measurement data. As a result of this modeling, the behavior of the LLRF system and the influence of each subsystem on system behavior are investigated. The results are summarized in a noise budget for each subsystem.

3.1 Noise Modeling

There are three methods to describe noise in LTI systems. These methods are the noise factor, the equivalent input noise, or the signal-to-noise ratio (SNR). The application of these three methods is derived from the amount of available information about the noise source, the noisy system, the frequency dependency and/or correlation.

One of the most common used parameters for noisy linear networks, especially in RF applications, is the noise factor F, which describes the degradation of the SNR from the network input to the output. It is a scalar and integral measure, which is defined for a certain bandwidth, and it is dependent on the source impedance of the linear network [16]. The noise factor has no information about correlation or frequency distribution. The latter can be handled by defining a frequency dependent noise factor $F(f)$ which is defined for each frequency band of $1\,\text{Hz}$ width.

A further noise description, which is used for operational amplifiers, is the equivalent input or output noise, which can be defined as an equivalent voltage, current, or power spectral density. For this measure, a frequency dependent correlation coefficient $\gamma(f)$ can be defined, which describes the similarity of two noisy signals [17].

The description of the SNR is commonly used in ADC applications. It describes the ratio of the signal power to the integrated noise power over a given bandwidth, typically the first Nyquist band ($0\,\mathrm{Hz}$ up to half of the sampling rate) [18], at the input of the ADC.

In the following, the derivation of the relation between the noise factor and the equivalent input noise is presented. In Fig. 3.1 (top), a noisy LTI system
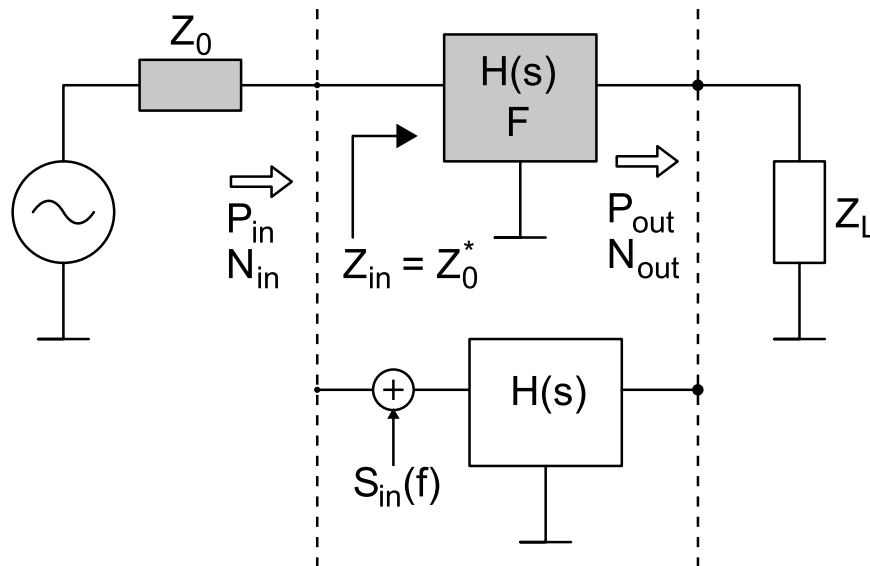
Figure 3.1: Top: Noisy network, described by transfer function $H(s)$ and noise factor F. The input of the network is matched to the reference impedance Z_0; Bottom: Noiseless network with additive equivalent input noise source $S_{\mathrm{in}}(f)$

with transfer function $H(s)$ is shown. The internal noise sources are described by the noise factor F, and an equivalent circuit can be found where all these internal noise sources are combined in one additive noise source outside the linear network, while the residual network is noiseless (Fig. 3.1 (bottom)). If the linear network is assumed to be matched to the source impedance $Z_{\mathrm{in}} = Z_0^*$, the signal and noise power at the input of the linear network are equal to the available power of the source. The network and the source are assumed to be at the same temperature $T_0 = 290\,\mathrm{K}$. At the input of the linear network, the available signal power is P_{in} and the noise power is N_{in}, while the available output signal power is P_{out} and

the noise power is N_{out}. The power gain G of the linear network is defined by

$$G = \frac{P_{\text{out}}}{P_{\text{in}}}. \tag{3.1}$$

The noise factor F is defined by

$$F = \frac{P_{\text{in}}/N_{\text{in}}}{P_{\text{out}}/N_{\text{out}}} = \frac{\text{Input signal-to-noise ratio}}{\text{Output signal-to-noise-ratio}} \tag{3.2}$$

or

$$F = \frac{N_{\text{out}}}{N_{\text{out},0}} == \frac{N_{\text{out}}}{G \cdot N_{\text{in}}} = \frac{\text{Output noise power for noisy network}}{\text{Output noise power for noiseless network}}. \tag{3.3}$$

The noise figure NF is a logarithmic quantity and is defined as

$$\text{NF} = 10 \log_{10} F. \tag{3.4}$$

The available input noise power from the source for $1\,\text{Hz}$ bandwidth and temperature of $T_0 = 290\,\text{K}$ is

$$N_{\text{in}} = N_{\text{th}} = k_B T_0 \, \Delta f = 4 \cdot 10^{-21} \, \text{W}, \tag{3.5}$$

with $k_b = 1.38 \cdot 10^{-23}\,\text{J/K}$, the Boltzmann constant. The output noise of the noiseless linear network is the amplified thermal noise power of the source

$$N_{\text{out},0} = G \, k_B T_0 \, \Delta f = G \, N_{\text{in}} = G \, N_{\text{th}}. \tag{3.6}$$

For the output noise power of the noisy network,

$$N_{\text{out}} = G(k_B T_0 \, \Delta f + N_{\text{in}}^e) = G(N_{\text{th}} + N_{\text{in}}^e) \tag{3.7}$$

the equivalent input noise power N_{in}^e of the linear network is added and amplified, too. From Eqn. 3.2 to 3.7, the equivalent input noise power of the linear network

$$N_{\text{in}}^e = (F - 1)k_B T_0 \, \Delta f = (F - 1) \, N_{\text{th}} \tag{3.8}$$

can be derived [14]. For a noiseless linear network with noise factor $F = 1$, the resulting equivalent input noise is zero and the signal-to-noise ratios at the input and output are equal. The total equivalent noise power referred to the input is

$$N_{\text{total}}^{\text{in}} = F k_B T_0 \, \Delta f = N_{\text{th}} + N_{\text{in}}^e \tag{3.9}$$

and is derived from the thermal noise power of the source and the noise power of the linear network. For a noiseless linear network with $F = 1$, the total noise power $N_{\text{total}}^{\text{in}}$ is equal to the available thermal noise power of the source.

For the assumption of uniformly distributed input noise (white gaussian noise) over the bandwidth Δf, the power spectral density of the equivalent input noise is defined by

$$S_{\text{in}}^e(f) = \frac{N_{\text{in}}^e}{\Delta f} = (F - 1)k_B T_0 \tag{3.10}$$

with

$$S_{\text{in}}(f) = S_{\text{th}} + S_{\text{in}}^e(f), \tag{3.11}$$

where the power spectral density of the thermal noise is

$$S_{\text{th}} = k_B T_0 = 4 \cdot 10^{-21}\,\text{Ws}. \tag{3.12}$$

For a frequency dependent noise factor $F(f)$, the power spectral density of the equivalent input noise can be defined by

$$S_{\text{in}}^e(f) = (F(f) - 1)k_B T_0 \tag{3.13}$$

while the noise power N_{in}^e is determined by

$$N_{\text{in}}^e = \int_{-\infty}^{\infty} S_{\text{in}}^e(f)\mathrm{d}f. \tag{3.14}$$

With $H(s)$ as transfer function of the LTI system, the transport of the power spectral density from the input to the output of the LTI system is defined by

$$S_{\text{out}}(f) = S_{\text{in}}(f) \cdot |H(s)|^2, \tag{3.15}$$

while $S_{\text{in}}(f)$ is the input spectral density

$$S_{\text{in}}(f) = F(f)k_B T_0, \tag{3.16}$$

which contains the spectral densities of the source and the noisy network. Due to the definition of the SNR, it is useful to define the power spectral density relative to the power of the signal and the carrier P_c, respectively, which leads to

$$S(f) = \frac{F(f)k_B T_0}{P_c}. \tag{3.17}$$

In logarithmic domain, the unit is [dBc/Hz], where subscript c indicates the relation to the carrier. The carrier related spectral density is a spectral measure, while the SNR is an integral measure defined for a certain bandwidth B. The relation between the SNR and the carrier related spectral density is

$$\frac{1}{\text{SNR}} = \frac{N}{P_c} = \int_B S(f)\mathrm{d}f = \frac{1}{P_c} \cdot \int_B F(f)k_B T_0 \mathrm{d}f \tag{3.18}$$

In the following the calculations are based on the carrier related power spectral density which will be referred to just as power spectral density.

3.1.1 Amplitude and Phase Noise

For the description of amplitude and phase noise of a sinusoidal signal, the following equations are used [19]. White noise $n(t)$ is added to a sinusoidal signal with frequency f_0 and amplitude V_0

$$
\begin{aligned}
v(t) &= V_0 \cos(2\pi f_0 t) + n(t) \\
&= V_0[1 + \alpha(t)] \cos(2\pi f_0 t + \varphi(t)).
\end{aligned}
\tag{3.19}
$$

This leads to a signal with uniformly distributed amplitude noise $\alpha(t)$ and phase noise $\varphi(t)$. With the assumption of

$$
\begin{aligned}
|\alpha(t)| &\ll 1 \\
|\varphi(t)| &\ll 1
\end{aligned}
\tag{3.20}
$$

Eqn. 3.19 yields

$$
v(t) = \underbrace{V_0 \cos(2\pi f_0 t)}_{\vec{V_0}} + \underbrace{v_c(t) \cos(2\pi f_0 t)}_{\vec{V_\alpha}} - \underbrace{v_s(t) \sin(2\pi f_0 t)}_{\vec{V_\varphi}}
\tag{3.21}
$$

with

$$
\begin{aligned}
v_c(t) &= V_0 \alpha(t) \\
v_s(t) &= V_0 \varphi(t)
\end{aligned}
\tag{3.22}
$$

for the in-phase and quadrature part of the noise related to the carrier. The spectrum of $v(t)$, $V(f)$, contains the carrier $\delta(f - f_0)$ and the spectrum of the amplitude, $V_\alpha(f)$, and phase noise, $V_\varphi(f)$.

$$
V(f) = V_0 \,\delta(f - f_0) + V_\alpha(f) + V_\varphi(f).
\tag{3.23}
$$

In Fig. 3.2, a graphical illustration in time domain and the overlaid spectrum of amplitude and phase noise are shown. With the modulation frequency $f_m = f - f_0$, the power spectral density is defined by the square of the sum of the Fourier transformation of the noise signal.

$$
\begin{aligned}
S_\alpha(f_m) &= \frac{1}{V_0^2}|\mathcal{F}\{\alpha(t)\}|^2 \\
S_\varphi(f_m) &= \frac{1}{V_0^2}|\mathcal{F}\{\varphi(t)\}|^2
\end{aligned}
\tag{3.24}
$$

The power spectral density of the baseband signal is defined as [20]

$$
S(f_m) = S_\varphi(f_m) + S_\alpha(f_m).
\tag{3.25}
$$

For a noisy LTI system with frequency dependent noise factor $F(f)$, the power spectral densities of the equivalent input amplitude and phase noise

$$
S_\varphi(f) = \frac{F(f)k_B T_0}{P_{\text{in}}}
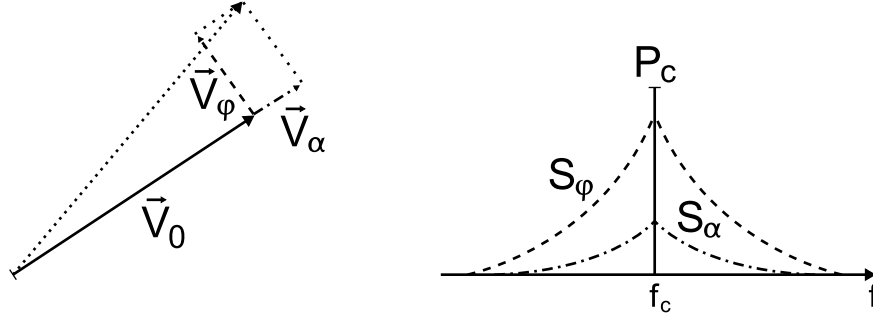\tag{3.26}
$$

Figure 3.2: Vectorial representation in time domain of amplitude and phase noise (left); Overlaid spectrum of amplitude and phase noise (right)

and

$$S_\alpha(f) = \frac{F(f)k_B T_0}{P_{\text{in}}} \tag{3.27}$$

can be derived. The phase noise can also be defined as the commonly known single sideband phase noise

$$\mathcal{L}(f) = \frac{S_\varphi(f)}{2}. \tag{3.28}$$

For further investigations, the root mean square values (rms) of the amplitude and phase jitter are useful, which are derived from the integration of the power spectral densities

$$\left(\frac{\Delta A}{A}\right)_{\text{rms}} = \sqrt{\int_{f_1}^{f_2} S_\alpha(f)\mathrm{d}f} \tag{3.29}$$

and

$$\Delta\varphi_{\text{rms}} = \sqrt{\int_{f_1}^{f_2} S_\varphi(f)\mathrm{d}f} \tag{3.30}$$

for a given bandwidth. From the phase noise, the rms timing jitter can be determined to read

$$\Delta t_{\text{rms}} = \frac{1}{2\pi f_0}\sqrt{\int_{f_1}^{f_2} S_\varphi(f)\mathrm{d}f}, \tag{3.31}$$

which is related to the carrier frequency f_0.

3.1.2 Amplifier noise model

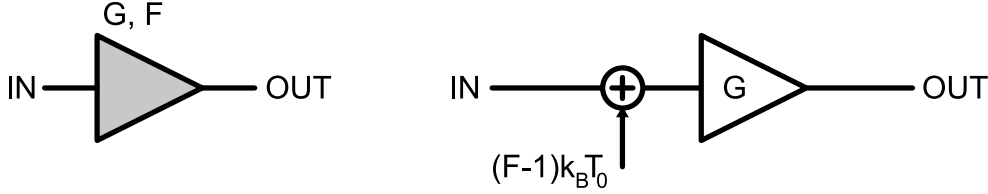Based on the noise description in section 3.1, a model for amplifier noise is shown in Fig. 3.3.

Figure 3.3: Equivalent circuit of a noisy amplifier with noise factor F and power gain G

The power spectral density of the equivalent input noise of the amplifier is added at the input of a noiseless amplifier. The amplitude and phase noise of an amplifier can be defined by the noise figure F of the amplifier and the input power P_{in} by

$$S_x(f) = b_0 + b_{-1}\frac{1}{f} \quad \text{with } x : \alpha, \varphi \tag{3.32}$$

with

$$b_0 = \frac{F k_B T_0}{P_{in}}. \tag{3.33}$$

The first term b_0 describes the white noise contribution of the amplifier due to internal thermal noise sources, while the second term b_{-1} represents the flicker noise of the amplifier which is an experimental parameter. It describes the level of the power spectral density at $1\,\text{Hz}$. Another method for flicker noise description is

$$S_x(f) = \frac{F(f)k_B T_0}{P_{in}} \quad \text{with } x : \alpha, \varphi \tag{3.34}$$

with a frequency dependent noise factor

$$F(f) = \left(1 + \frac{f_c}{f}\right) F_0 \tag{3.35}$$

while f_c is the corner frequency of the flicker noise and F_0 the noise factor for the broadband noise. This definition is inapt, because of the input power dependent flicker frequency f_c. In Eqn. 3.32, this dependency is taken into account. The amplifier gain increases the signal level in the same manner as it increases the noise level. Therefore the SNR or carrier related spectral density of a signal is not affected by the gain of the amplifier. In the following, the calculaions are based on carrier related spectral densities, which allows to neglect the amplification of the devices. As long as the function of the devices is linear, this simplification is justified.

3.1.3   Mixer noise model

The model for the noise of the mixer is shown in Fig. 3.4. It is described by the noise figure F and the conversion loss L and is added at the input of a noiseless mixer. For passive mixers, the noise figure F is related to the conversion loss L
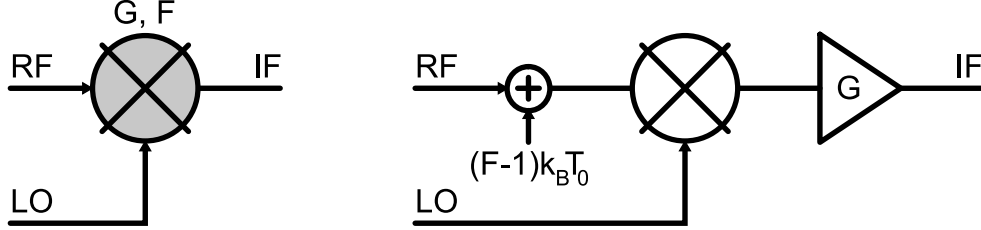

Figure 3.4: Equivalent circuit of a noisy mixer with noise figure F and conversion gain G

by

$$F = \frac{1}{L} \Leftrightarrow F(f) = \frac{1}{L(f)}, \tag{3.36}$$

if the power spectral density of the input noise is $k_B T_0$ and T_0 is equal to the mixer temperature [14]. The conversion loss L, and therefore the noise factor F, can be defined to be frequency dependent, too. For an active mixer, the conversion gain G is additionally modeled by a noiseless amplifier at the mixer output. The power spectral density of the equivalent input noise is

$$S_{\otimes,x}(f) = \frac{F(f)k_B T_0}{P_{\text{in}}} \quad \text{with } x : \alpha, \varphi \tag{3.37}$$

and is added to the RF signal at the input of the mixer [21]. For the noise transport from the RF and LO ports to the output (IF) port, some simplifications are assumed. The mixer should operate in the linear mode for the RF port while the LO input is saturated. An ideal sideband suppression and image rejection is assumed, too. Under these conditions, the mixing process can be modeled as a multiplication in time domain

$$v_{\text{IF}}(t) = v_{\text{RF}}(t) \cdot v_{\text{LO}}(t). \tag{3.38}$$

The RF and LO signal are sinusoidal signals with additive white noise

$$v_{\text{LO}}(t) = A_{\text{LO}} \cdot \sin(2\pi f_{\text{LO}} t + \varphi_{\text{LO}}(t)) \tag{3.39}$$

$$v_{\text{RF}}(t) = A_{\text{RF}} [1 + \alpha_{\text{RF}}(t)] \cdot \sin(2\pi f_{\text{RF}} t + \varphi_{\text{RF}}(t) + \varphi_0) \tag{3.40}$$

which lead to uniformly distributed amplitude noise $\alpha_{\text{RF}}(t)$ and phase noise $\varphi_{\text{RF}}(t)$ and $\varphi_{\text{LO}}(t)$ [17]. The amplitude noise of the LO is neglected, due to

the saturation of the LO port [22]. The up- and downconversion is described by the sum

$$\Sigma f = f_{\mathrm{RF}} + f_{\mathrm{LO}} = f_{\mathrm{IF}}^{up} \qquad (3.41)$$

and the difference

$$\Delta f = f_{\mathrm{RF}} - f_{\mathrm{LO}} = f_{\mathrm{IF}}^{dw} \qquad (3.42)$$

of the RF and LO frequency. With

$$A = \frac{A_{\mathrm{RF}} A_{\mathrm{LO}}}{2} \qquad (3.43)$$

Eqn. 3.38 leads to

$$v_{\mathrm{IF}}^{\mathrm{up}}(t) = A\left[1 + \alpha_{\mathrm{RF}}(t)\right] \cdot \cos(2\pi\Sigma f + \varphi_{\mathrm{LO}}(t) + \varphi_{\mathrm{RF}}(t) + \varphi_0) \qquad (3.44)$$

for upconversion and

$$v_{\mathrm{IF}}^{\mathrm{dw}}(t) = A\left[1 + \alpha_{\mathrm{RF}}(t)\right] \cdot \cos(2\pi\Delta f + \varphi_{\mathrm{RF}}(t) - \varphi_{\mathrm{LO}}(t) + \varphi_0) \qquad (3.45)$$

for downconversion. This leads to a power spectral density of the phase noise

$$S_\varphi^{\mathrm{IF}}(f) = S_\varphi^{\mathrm{LO}}(f) + S_\varphi^{\mathrm{RF}}(f) \pm 2\,\gamma(f)\sqrt{S_\varphi^{\mathrm{LO}}(f)}\sqrt{S_\varphi^{\mathrm{RF}}(f)} \qquad (3.46)$$

with $\gamma(f)$ as the frequency dependent correlation factor [23]. The plus or minus sign indicates the up- or downconversion, respectively. For uncorrelated phase noise at the RF and LO input, the correlation $\gamma(f)$ is equal to zero and Eqn. 3.46 leads to

$$S_\varphi^{\mathrm{IF}}(f) = S_\varphi^{\mathrm{LO}}(f) + S_\varphi^{\mathrm{RF}}(f). \qquad (3.47)$$

The power spectral density of the mixer noise $S_\otimes(f)$ is assumed to be uncorrelated and has to be added as depicted in Fig. 3.4 for the phase noise

$$S_\varphi^{\mathrm{IF}}(f) = S_\varphi^{\mathrm{LO}}(f) + S_\varphi^{\mathrm{RF}}(f) + S_{\otimes,\varphi}(f) \qquad (3.48)$$

and for the amplitude noise

$$S_\alpha^{\mathrm{IF}}(f) = S_\alpha^{\mathrm{RF}}(f) + S_{\otimes,\alpha}(f). \qquad (3.49)$$
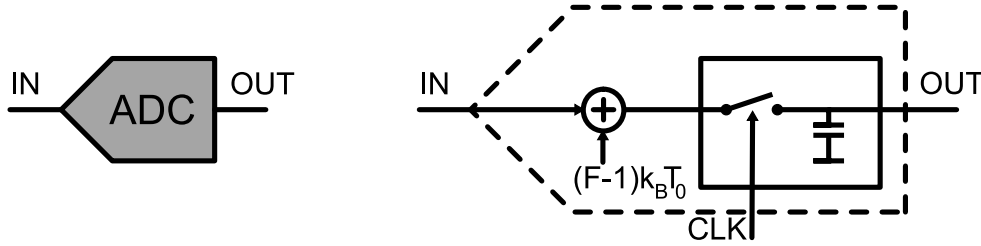
Figure 3.5: Equivalent circuit for ADC noise

3.1.4   ADC noise model

The application of a digital controller requires the digitization of the analog measurement signals. The SNR is a common measure used for the description of the ADC noise performance. Due to the increasing combination of RF components and ADCs, e.g. in software defined radio, a uniform noise description for system analysis and comparison is required [18]. For that the definition of the noise factor F and the spectral density $S(f)$ for the ADC is chosen similarly to the definition for the mixer (Section 3.1.3). It is based on the addition of an equivalent input noise at the input, while the following ideal and noiseless sample-and-hold stage is depicted to describe the sampling process (Fig. 3.5).

All noise sources like quantization noise, thermal noise of the ADC input stage, or errors due to clock jitter are summarized in this equivalent input noise. The noise factor or equivalent input noise can be derived from the SNR of the ADC. Either the SNR is measured, listed in the datasheet of the ADC, or is calculated by Eqn. 3.50 [18]

$$\text{SNR}_{\text{dB}} = -20 \log_{10} \left[(2\pi f_a t_j)^2 + \frac{2}{3} \left(\frac{1+\epsilon}{2^N} \right)^2 + \left(\frac{2\sqrt{2}V_n}{2^N} \right)^2 \right]^{\frac{1}{2}} \tag{3.50}$$

with the following ADC parameters:

f_a : input frequency [Hz]

t_j : rms clock timing jitter [s]

ϵ : differential nonlinearity, DNL [LSB]

N : number of bits

V_n : equivalent input noise [LSB].

If V_n, ϵ, and t_j are equal to zero, Eqn. 3.50 is simplified to the well-known formula

$$\text{SNR}_{\text{dB}} = 6.02 \cdot N + 1.76 \, \text{dB} \tag{3.51}$$

for the signal-to-noise ratio of an ideal ADC, measured over the Nyquist bandwidth $0 - f_s/2$, while f_s is the sampling frequency.

The first part in Eqn. 3.50 describes the influence of the rms timing jitter of the sampling clock. The rms timing jitter consists of two uncorrelated parts and is calculated by

$$t_j = \sqrt{t_{j,\text{ADC}}^2 + t_{j,\text{CLK}}^2} \tag{3.52}$$

with the internal rms aperture jitter of the ADC $t_{j,\text{ADC}}$ and the integrated rms timing jitter of the clock source $t_{j,\text{CLK}}$. The spectral distribution of this part depends on the phase noise spectrum of the CLK signal. For modern high-speed ADCs, the internal rms aperture jitter is much lower than the contribution from the CLK signal. The close-in phase noise of the CLK signal reduces the spectral resolution, while the broadband phase noise will cause degradation in the SNR. The bandwidth of the clock input at the ADC and therefore the upper frequency range for integration of the phase noise can be assumed to be twice the maximum sampling rate of the ADC, unless an external lowpass filter in front of the clock input is used for bandwidth limitation. The lower frequency range for jitter integration depends on the measurement time, because the width of the frequency bins is inversely proportional to the number of samples and measurement time, respectively.

The second part in Eqn. 3.50 shows the contribution of the quantization noise and differential nonlinearities (DNL), while the last part describes the equivalent input noise, which originates in thermal noise of resistive elements in the input stage of the ADC. Both parts are uniformly distributed over the Nyquist band [18].

In modern high speed ADCs, the two latter terms in Eqn. 3.50 lead to a SNR which is lower than 80 dB, while the first term is dependant on the frequency of the sampled signal. This leads to a decreasing SNR for an increasing input frequency. The contributions of a CLK signal with a jitter of 100 fs and an input frequency of up to 100 MHz are in the range

$$\text{SNR}_{\text{dB}} = 20 \log_{10} \left(\frac{1}{2\pi \cdot 100\,\text{MHz} \cdot 100\,\text{fs}} \right) = 84\,\text{dB}. \tag{3.53}$$

Based on the SNR which is related to the power spectral density integrated over the Nyquist bandwidth from DC to half of the sampling rate ($f_s/2$) and the assumption of a sinusoidal input signal with amplitude V_{FS}, the equivalent rms input noise can be calculated to read

$$v_{\text{rms}} = V_{\text{FS,rms}} \cdot 10^{-\text{SNR}/20} \quad [\text{V}] \tag{3.54}$$

with the full-scale rms input voltage $V_{\text{FS,rms}}$. The noise factor is determined

$$F = \frac{v_{\text{rms}}^2}{k_B T_0 B R} = \frac{V_{\text{FS,rms}}^2}{R} \cdot \frac{1}{k_B T_0} \cdot 10^{-\text{SNR}/10} \cdot \frac{2}{f_s} \tag{3.55}$$

with the equivalent input impedance R of the ADC (Fig. 3.6). The noise figure in dB can be obtained from

$$\text{NF} = P_{\text{FS,dBm}} - N_{\text{th,dBm}} - \text{SNR}_{\text{dB}} - 10 \log \left(\frac{f_s}{2} \right) \quad [\text{dB}] \tag{3.56}$$

with the thermal noise floor $N_{\text{th,dBm}}$ and the full scale input power

$$P_{\text{FS,dBm}} = 10 \log \left(\frac{V_{\text{FS,rms}}^2}{R \cdot 1\,\text{mW}} \right) \quad [\text{dBm}] . \tag{3.57}$$
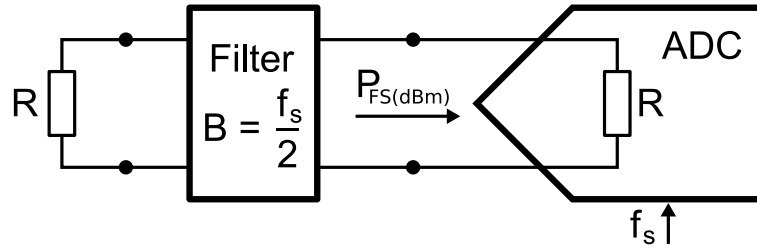

Figure 3.6: Equivalent circuit for calculation of the ADC noise factor

3.2   System Noise Model

To investigate the noise contribution of each component of the LLRF system with respect to amplitude and phase stability of the cavity field, a noise budget of the LLRF system is formed. The calculation of the noise budget is based on a control loop model from control theory. It can be derived from the description in Chapter 2 [24]. Simplifications lead to a model that is clearly arranged and easy to comprehend.

3.2.1   Simplifications

To simplify the modeling of the LLRF system, the subcomponents of the complex system are reduced to black boxes, which are described by their baseband transfer functions and internal noise sources, considered for a frequency band that ranges from 10 Hz up to 10 MHz beside the carrier. The model of each box is based on the calculation of a PLL [20]. The Laplace transforms of the phase and amplitude noise signals are used. The amplitude and phase loops are considered separately and all subsystems are assumed to operate in a linear regime. Furhtermore, only the high frequency fluctuations are noticed and errors due to the vectorsum calibration and pulse-to-pulse fluctuations are neglected. For each system, the baseband transfer function is used, because the disturbances and noise sources are modeled as modulations of the carrier.

3.2.2 Combination of Components

The transfer characteristics of the subsystems described in the previous chapter are used. The simplified LLRF system is shown in Fig. 3.7.
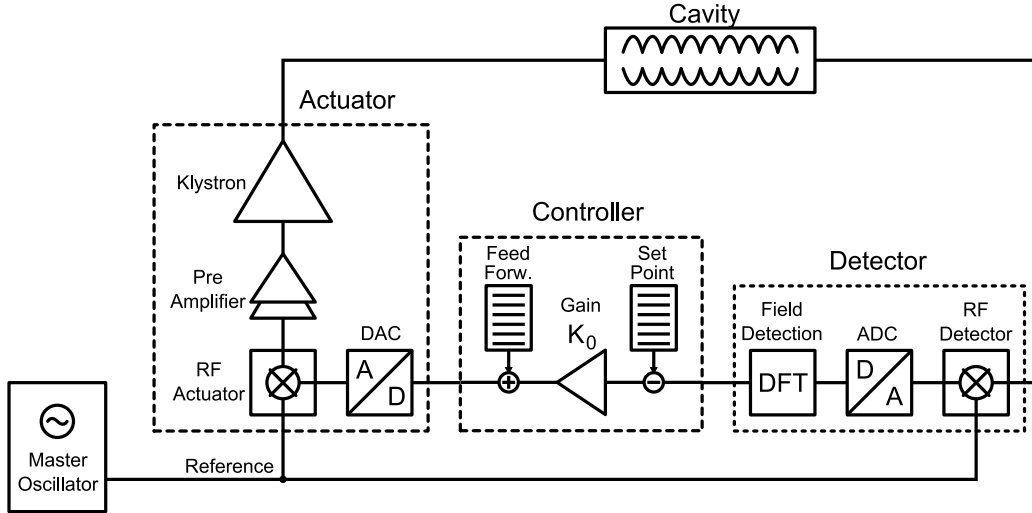

Figure 3.7: Block diagram of the simplified LLRF system with single cavity;

The Plant

The plant is modeled as a single cavity, because of the neglection of the vectorsum calibration errors. Therefore, no nonlinearity errors are affecting the loop. Due to the limitation of the bandwidth to a lower boundary of 10 Hz, all slow changes, like microphonics, Lorentz force detuning, and temperature drifts, are neglected. The baseband model of the cavity is a lowpass filter with a corner frequency equal to the half of the cavity bandwidth. To simplify the calculations, the cavity is assumed to be in steady state.

The Detector

The detector is a combination of two subsystems. The first one is the analog front-end, based on an RF mixer, which is used for frequency conversion from the RF to a lower IF. The second subsystem is an ADC, which is used for digitization of the IF. It provides the digital cavity signal for the controller.

The frequency downconversion operates linearly, while the reference input is assumed to be insensitive to amplitude noise of the reference signal. The IF phase noise consists of the sum of the RF and LO phase noise (Eqn. 3.48), while the IF amplitude noise is still the amplitude noise of the RF signal (Eqn. 3.49).

The frequency responses of both subsystems are combined and modeled by one lowpass filter which describes the limited bandwidth of the analog front-end

and optional digital filtering, respectively. The noise contribution of the front-end and ADC in amplitude and phase are summarized and added at the detector input. The required bandwidth of the detector can be derived from the following line of arguments. If one assumes disturbances of the cavity field in the range of 1° due to microphonics and Lorentz force detuning, which is reduced by an adaptive feed forward, a loop gain in the range of 100 is required to reach the tolerable phase instability of 0.01°. This leads to a unity gain at 20 kHz with a cavity bandwidth of 200 Hz. For diagnostic purposes, e.g. detection of beam induced transients with a bunch repetition rate of 1-10 MHz, it could be useful to detect the cavity signal with a bandwidth of 1-10 MHz. Due to the small bandwidth of the plant of 200 Hz, the influence of the detector bandwidth of 1-10 MHz only affects the rms stability of the detector output signal, but not the rms stability of the cavity field. In the following modeling, the detector bandwidth is set to 1 MHz.

The Controller

In the controller, the set point vector is subtracted from the measured cavity field vector and the resulting error vector is multiplied by the controller gain and added to a feed forward table. The resulting control signal is fed to the actuator. In the black box model, the controller is modeled as P-controller.

The Actuator

The actuator consists of a DAC, which converts the amplified error vector from a digital to an analog signal, and an analog upconverter which changes the phase and amplitude of the incident signal of the cavity. The actuator also contains the following high power pre-amplifiers and the klystron which delivers the required high power signal level to the cavities. The function of the actuator is modeled similar to the function of the detector. The RF phase at the output is the sum of the IF and LO phases. The bandwidth of the actuator, preamplifier, and klystron is in the range of 1-10 MHz. The transfer function of the actuator can be neglected because of the comparatively lower bandwidth of the cavity of 200 Hz. Therefore, only the internal noise sources of the RF actuator, preamplifiers, and klystron are summarized and added to the RF signal.

Master Oscillator and Reference

The Master Oscillator (MO) is modeled by its phase noise which is used for the simulation of the phase loop only. The amplitude noise of the MO is neglected, because of the assumed insensitivity of the LO ports of the detector and actuator against amplitude fluctuations.

3.2.3 The Control Loop Model

The control loop model of the LLRF system in Laplace domain is depicted in Fig. 3.8. It contains the transfer functions of the plant, $G(s)$, the detector, $C(s)$, and the controller, $K(s)$. The output of the cavity is the cavity field $Y(s)$, which
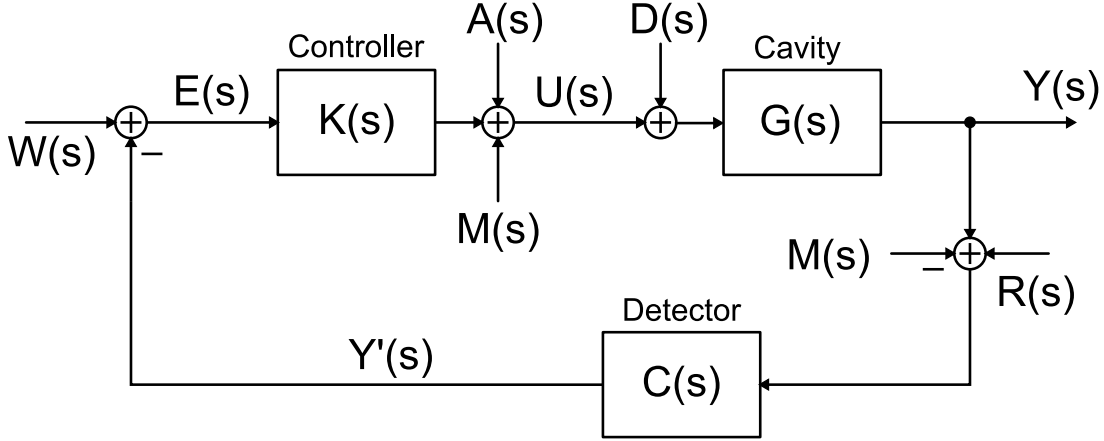

Figure 3.8: Control loop model of the simplified LLRF system

is measured with the detector. The detector output signal $Y'(s)$ is subtracted from the setpoint $W(s)$, which leads to the error signal $E(s)$. $E(s)$ is fed into the controller. The control signal $U(s)$ at the output of the controller drives the actuator and is sent to the cavity. The error sources are the detector noise, $R(s)$, the actuator noise, $A(s)$, the disturbances to the cavity, $D(s)$, and the phase noise from the MO, $M(s)$.

3.2.4 Transfer Functions

For modeling the LLRF system as a control loop, transfer functions are defined for each subsystem. The plant $G(s)$ is characterized by a lowpass filter

$$G(s) = \frac{\omega_{12}}{s + \omega_{12}} \tag{3.58}$$

with the comparatively low cavity bandwidth $\omega_{12} = 2\pi \cdot 216\,\text{Hz}$ (with the loaded quality factor $Q_L = 3 \cdot 10^6$ and the center frequency $f_c = 1.3\,\text{GHz}$). This describes the bandpass characteristics around the carrier at $1.3\,\text{GHz}$ of the cavity transformed to the baseband. The detector $C(s)$ is described as a lowpass, too:

$$C(s) = \frac{\omega_c}{s + \omega_c} \tag{3.59}$$

The detector bandwidth is set to $\omega_c = 2\pi \cdot 1\,\text{MHz}$. The controller

$$K(s) = K_0 \tag{3.60}$$

is modeled as P-controller with gain K_0 which is within the range of 1 to 1000 during the simulation. The controller gain is equal to the loop gain, while all other subsystems are normalized to a gain of 1.

Based on system and control theory, the field $Y(s)$ of the cavity is composed of the noise contribution of each subsystem multiplied by its transfer function. With the transfer function of the open-loop

$$G_0(s) = G(s)\,K(s)\,C(s), \tag{3.61}$$

the transfer functions of the noise contributions of each subsystem to the cavity field $Y(s)$ can be written as

$$H_A(s) = \frac{G(s)}{1 + G_0(s)} \tag{3.62}$$

for the actuator noise and disturbances,

$$H_R(s) = -\frac{G_0(s)}{1 + G_0(s)} \tag{3.63}$$

for the detector noise, and

$$H_{MO}(s) = \frac{G(s)}{1 + G_0(s)} + \frac{G_0(s)}{1 + G_0(s)} \tag{3.64}$$

for the contribution of the MO phase noise. The first term describes the contribution of the MO noise to the cavity field phase via the actuator, while the second one describes the contribution via the detector. Both terms are equal to the transfer functions of the actuator and detector noise to the cavity field, respectively. The transfer function for changes of the setpoint to the cavity field is

$$H_W(s) = \frac{G(s)K(s)}{1 + G_0(s)} \tag{3.65}$$

for the sake of completeness. The cavity field then results in

$$\begin{aligned} Y(s) \;=\; & H_A(s)\,[D(s) + A(s)] + H_W(s)\,W(s) \\ & + H_R(s)\,R(s) + H_{MO}(s)\,M(s). \end{aligned} \tag{3.66}$$

In Fig. 3.9, these transfer functions are shown. The parameter set is $\omega_{12} = 2\pi \cdot 216\,\mathrm{Hz}$ for the cavity bandwidth, $\omega_c = 2\pi \cdot 1\,\mathrm{MHz}$ for the detector bandwidth, and $K_0 = 100$ for the loop gain. The disturbances $D(s)$ and the actuator noise $A(s)$ are suppressed by the loop gain K_0 and the filter function with the loop bandwidth ω'_{12} which is defined by
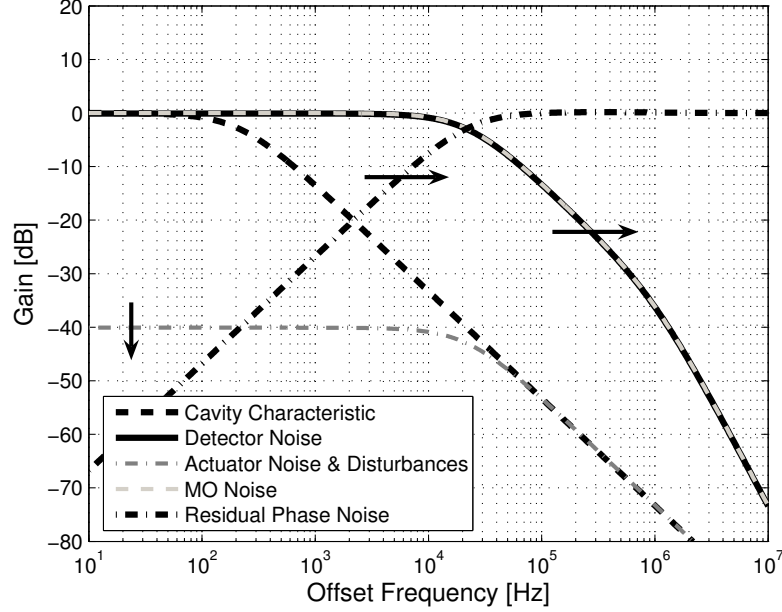
$$\omega'_{12} = K_0 \cdot \omega_{12}. \tag{3.67}$$

Figure 3.9: Transfer function of the noise contribution of each subsystem to the cavity field $Y(s)$. The parameter set is $\omega_{12} = 2\pi \cdot 216\,\text{Hz}$, $\omega_c = 2\pi \cdot 1\,\text{MHz}$, and $K_0 = 100$. The arrows indicate increasing loop gain K_0

The higher the gain K_0, the lower is the contribution of the actuator and disturbances. The detector noise $R(s)$ is suppressed outside the loop bandwidth ω'_{12} only. The higher the gain, the higher is the loop bandwidth and the higher is the contribution of the detector noise to the cavity field. The bandwidth of the detector is negligible in comparison to the cavity bandwidth or the loop bandwidth. The transfer function of the MO phase noise contribution $H_{\text{MO}}(s)$ is congruent with the detector transfer function $H_{\text{R}}(s)$. The cavity phase follows the MO phase within the loop bandwidth ω'_{12}, while the high frequency fluctuations are suppressed by the filter function of the cavity.

The accelerating voltage V_{acc} is dependent on the injection time of the beam t_b or the beam phase φ_b

$$V_{acc}(t_b) = V_{cav} \cdot \cos\varphi_b = V_{cav} \cdot \cos(\omega t_b)$$

with the cavity voltage V_{cav} (Eqn. 2.10). For amplitude jitter $(\Delta A/A)_{\text{cav}}$ of the cavity voltage and phase jitter $\Delta\varphi_{\text{cav}}$ between the cavity field and the beam, the accelerating voltage is

$$V_{acc} = V_{cav} \left(1 + \left(\frac{\Delta A}{A}\right)_{\text{cav}}\right) \cos(\varphi_b + \Delta\varphi_{\text{cav}}). \tag{3.68}$$

Because of the MO being the overall frequency reference for the whole accelerator as well as for the RF gun laser, the phase noise of the cavity field relative to the

MO is of interest. Therefore, the residual phase jitter of the cavity field is defined as the difference between the cavity field and the MO

$$
\begin{aligned}
Y_{\text{res},\varphi}(s) &= Y(s) - M(s) \\
&= H_{\text{A}}(s)\,[D(s) + A(s)] + H_{\text{R}}(s)\,R(s) \\
&\quad + (H_{\text{MO}}(s) - 1)\,M(s).
\end{aligned}
\tag{3.69}
$$

The integration of the residual phase noise $Y_{\text{res},\varphi}(s)$ describes the phase jitter $\Delta\varphi_{\text{cav}}$ in Eqn. 3.68, while the amplitude jitter $(\Delta A/A)_{\text{cav}}$ is equal to the integrated amplitude noise of the cavity field

$$
Y_{\text{res},\alpha}(s) = H_{\text{A}}(s)\,[D(s) + A(s)] + H_{\text{R}}(s)\,R(s).
\tag{3.70}
$$

The transfer function of the MO to the residual field jitter (Fig. 3.9) is

$$
H_{\text{MO,res}} = H_{\text{MO}}(s) - 1 = \frac{G(s)}{1 + G_0(s)} - \frac{1}{1 + G_0(s)}.
\tag{3.71}
$$

The contributions of the actuator, detector, and disturbances are uncorrelated to the MO and therefore uncorrelated to the beam. The beam is modulated with these noise contributions, while the contribution of the amplitude and phase noise is dependent on the beam phase (Eqn. 2.10).

3.2.5   Detector Output

The field stability measured at the detector output is one figure of merit for the quality of the field control. The phase noise at the detector output consists of the detector noise and the difference between the cavity field phase and the MO phase (Section 3.1.3). This leads to

$$
\begin{aligned}
Y'(s) &= [Y(s) - M(s) + R(s)] \cdot C(s) \\
&= \ldots \\
&= \left[\frac{G(s)}{1 + G_0(s)}\,A(s) + \frac{1}{1 + G_0(s)}\,R(s) + \frac{G(s) - 1}{1 + G_0(s)}\,M(s) \right] \cdot C(s)
\end{aligned}
\tag{3.72}
$$

for the phase noise at the detector output. The actuator noise is suppressed by the cavity and the controller. The noise contributions of detector and MO consist of high frequency noise outside the loop bandwidth, which can be derived from the negative feedback loop (Fig. 3.10).

3.2.6   Noise Sources

For the description of the equivalent input noise sources, the power spectral density relative to the carrier is expressed by the parameter for the white noise floor,
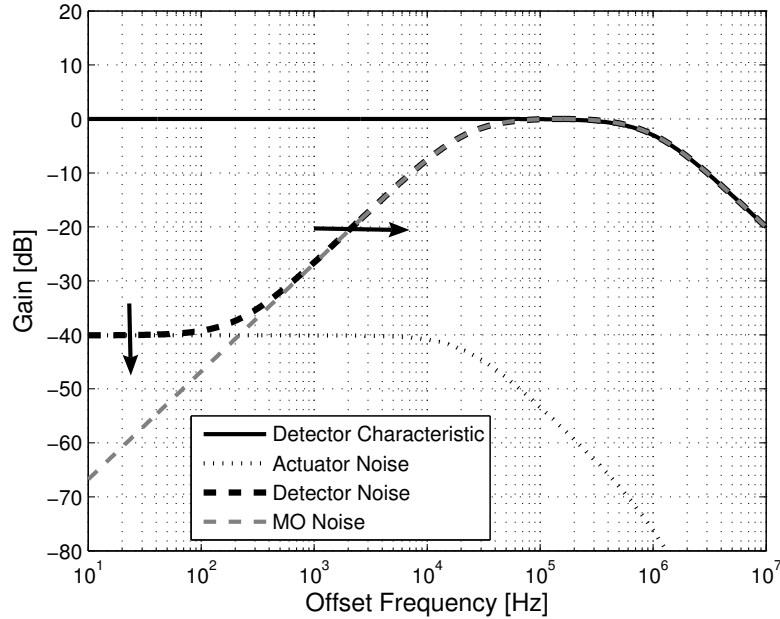
Figure 3.10: Transfer function of the noise contribution of each subsystem to the detector output $Y'(s)$. The parameter set is $\omega_{12} = 2\pi \cdot 216\,\text{Hz}$, $\omega_c = 2\pi \cdot 1\,\text{MHz}$, and $K_0 = 100$. The arrows indicate increasing loop gain K_0

b_0, and by the parameter for the flicker noise, b_{-1}. The equivalent input spectral densities of the actuator and detector noise are

$$
\begin{aligned}
S_A(f) &= b_{\text{a},0} + b_{\text{a},\text{-1}} \cdot f^{-1} \\
S_R(f) &= b_{\text{r},0} + b_{\text{r},\text{-1}} \cdot f^{-1}.
\end{aligned}
\tag{3.73}
$$

The parameters for the equivalent input spectral density of the actuator noise are derived from measurements of the klystron noise and listed in Tab. 3.1. The contribution of the RF upconverter is comparatively low and is neglected [25].

For the simulation, three sets of parameters for the equivalent input spectral density of the detector noise are chosen. The first two sets (detector 1 and 2) are derived from real measurement data, while the third parameter set (detector 3) is based on theoretical considerations.

Detector 1 is currently installed at FLASH and is based on a low power Gilbert-cell mixer followed by a 14 bit, 1 MHz sampling ADC. The noise floor of -135 dBc/Hz is derived from the noise floor of the ADC, while the 1/f-noise component originates in the output buffer of the analog front-end. The values for detector 2 are based on a new developed detector which will be described later in this thesis. The noise floor of -150 dBc/Hz is derived from an improved ADC stage following the analog front-end, based on a 16 bit, 81 MHz sampling ADC. The RF mixer increases the 1/f-noise component to -105 dBc. Detector 3 is a

	b_0 [dBc/Hz]	b_{-1} [dBc]
Actuator	-110	-90
Detector 1	-135	-120
Detector 2	-150	-105
Detector 3	-150	-130

Table 3.1: Parameters for the equivalent input noise sources of the detector and actuator

theoretical version, based on detector 2 with an improved 1/f-noise contribution of -130 dBc at 1 Hz. With detector 3, the effect of an improved 1/f-noise contribution is investigated. All values are summarized and listed in Tab. 3.1. The power spectral densities of the equivalent input noise of the actuator and detector are plotted in Fig. 3.11.
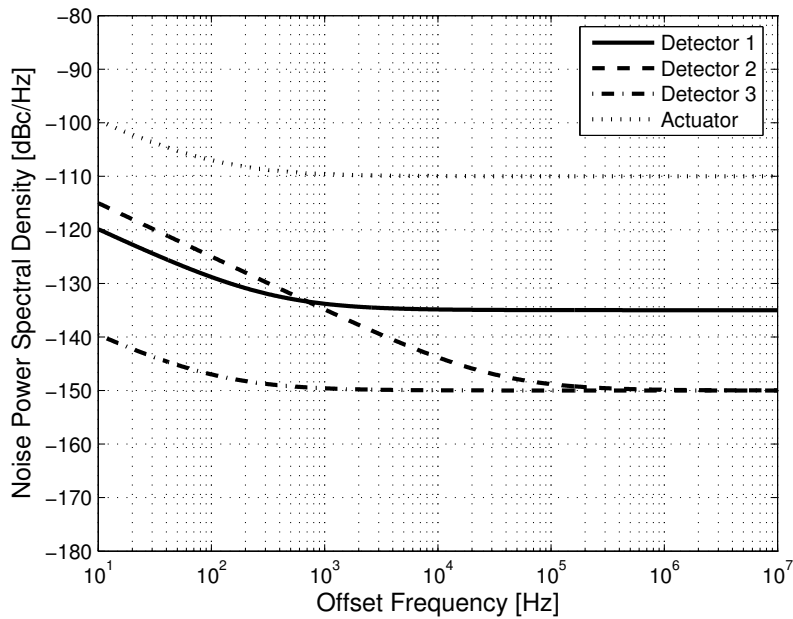

Figure 3.11: The equivalent input spectral densities for the detector and actuator noise

The disturbances are slow changes of the resonance frequency of the cavity caused by microphonics and Lorentz force detuning (section 2.4). In this simulation, only contributions and disturbances from the LLRF system are investigated. Microphonics and Lorentz force detuning both being below 1 kHz, these disturbances are suppressed by the controller.

The MO phase noise is based on measurement data taken from the currently installed MO at FLASH [26]. The phase noise $S_{\varphi,\mathrm{MO}}(f)$ is shown in Fig. 3.12.
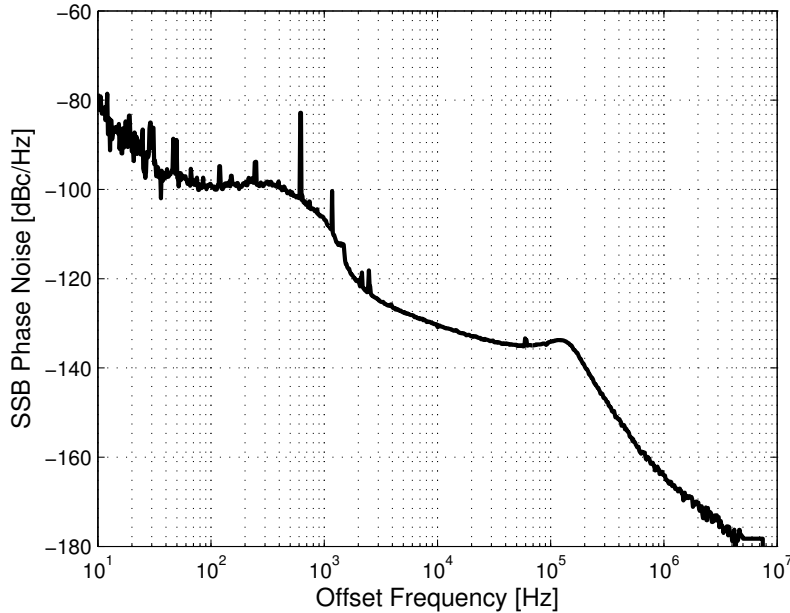
Figure 3.12: Phase noise of the currently installed MO at FLASH ($f_c = 1.3$ GHz), measured with the signal source analyzer E5250 (Agilent)

3.3 Simulation Results

To investigate the noise contribution of the components of the LLRF system with respect to amplitude and phase stability of the cavity field, a noise budget of the LLRF system is formed.

In Fig. 3.13, the power spectral density of the phase noise of the cavity field $Y(s)$, the MO, and the contributions of the detector (1) and actuator are shown. The controller gain is set to $K_0 = 100$ and the detector bandwidth is $\omega_c = 2\pi \cdot 1$ MHz. The phase of the cavity field follows the phase of the MO within the loop bandwidth. Outside the loop, the detector phase noise contribution affects the cavity field phase. The actuator contribution is suppressed by the loop gain of 100 (40 dB) and, outside the loop bandwidth, by the cavity. The detector contribution is suppressed outside the loop bandwidth by the cavity and influences the cavity field phase at 1 MHz.

Fig. 3.14 (left) shows the phase noise at the detector output $Y'(s)$ and the residual phase noise of the field and its composition for the same loop gain and detector bandwidth as mentioned before. On the right side of Fig. 3.14, the integrated phase jitter is shown, integrated from 10 MHz down to 10 Hz. The residual phase noise follows the MO outside the loop bandwidth, while within the loop bandwidth it is composed of the detector contribution and the MO, which is suppressed by the controller (cp. Fig. 3.9). The detector output is dominated by
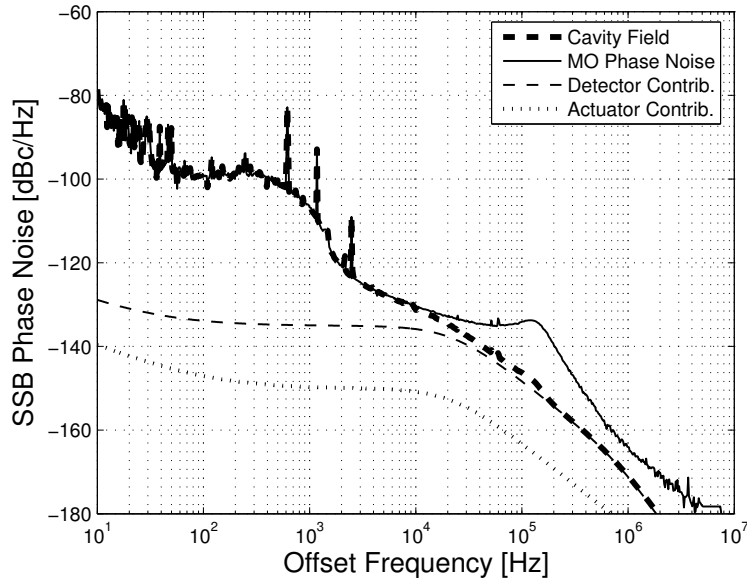
Figure 3.13: Power spectral density of the phase noise of the cavity field and contributions of the subsystems (detector, actuator) and the MO phase noise ($f_c = 1.3 \, \text{GHz}$);

the high frequency noise of the detector noise outside the loop bandwidth, while within the loop bandwidth it is composed of the MO and actuator contributions.

The residual phase jitter (Fig. 3.14 right) is dominated by the high frequency MO contribution, while the phase jitter at the detector output is only a measure for the upper limit of the residual jitter. It is caused by the high frequency noise of the detector.

Fig. 3.15 shows the amplitude noise and integrated amplitude jitter. The MO amplitude noise being neglected, the amplitude noise of the cavity field is determined by the detector and actuator noise contributions. As described for the phase noise, the actuator noise contribution is suppressed by the controller and the cavity, while the bandwidth of the detector contribution is increased by the loop gain. For a loop gain of $K_0 = 100$, the amplitude noise of the field is dominated by the detector noise contribution. The amplitude jitter at the detector output is higher than the amplitude jitter of the cavity field. It is mainly caused by the high frequency noise of the detector in the frequency band of the loop bandwidth $\omega'_{12} = 21.6 \, \text{kHz}$ up to the detector bandwidth $\omega_c = 1 \, \text{MHz}$. The actuator noise is suppressed by the controller and can be neglected.

The integrated phase jitter of the contributions of the subsystems (MO, detector, and actuator) to the field and residual jitter are summarized in Tab. 3.2. The phase and amplitude jitter at the detector output for a loop gain of $K_0 = 100$ are $\Delta\varphi = 3.14 \cdot 10^{-4} \, \text{rad}$ and $\frac{\Delta A}{A} = 3.05 \cdot 10^{-4}$, respectively. For the integrated
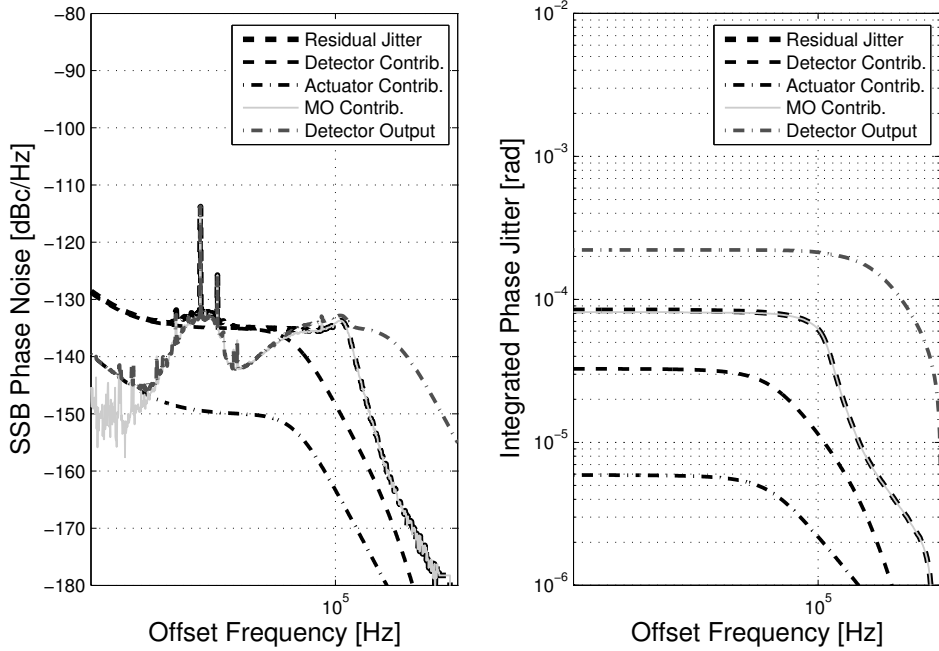
Figure 3.14: Power spectral density of the residual phase noise and contributions of the subsystems (detector, actuator, and MO) at the cavity field and detector output (left); integrated phase jitter of the residual phase noise, contributions of the subsystems (detector, actuator, and MO) and detector output (integrated from 10 MHz down to 10 Hz)(right);

Subsystem	System Jitter [rad]	Field Jitter [rad]	Residual Jitter [rad]
MO	$6.83 \cdot 10^{-4}$	$6.74 \cdot 10^{-4}$	$1.16 \cdot 10^{-4}$
Detector	$7.95 \cdot 10^{-4}$	$0.46 \cdot 10^{-4}$	$0.46 \cdot 10^{-4}$
Actuator	$141 \cdot 10^{-4}$	$0.08 \cdot 10^{-4}$	$0.08 \cdot 10^{-4}$
Σ		$6.74 \cdot 10^{-4}$	$1.19 \cdot 10^{-4}$

Table 3.2: Integrated phase jitter of the contributions of the subsystems (MO, detector, and actuator) to the cavity field and residual jitter for a loop gain of $K_0 = 100$ and integration bandwidth of 10 Hz to 10 MHz.
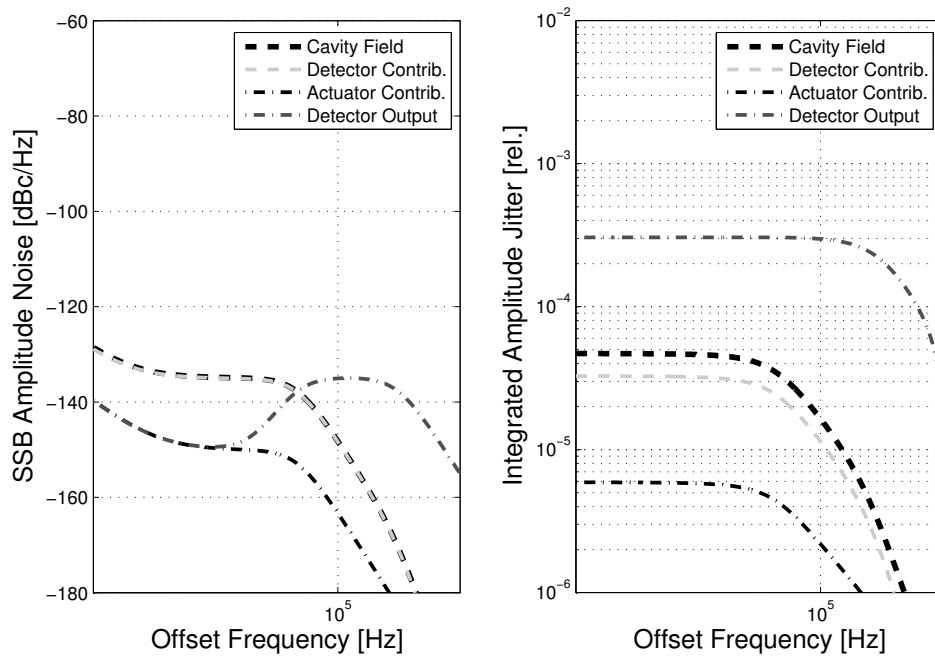
Figure 3.15: Power spectral density of the amplitude noise of the cavity field and contributions of the detector and actuator (left); integrated amplitude jitter of the cavity field and contributions of the detector and actuator (integrated from $10\,\text{MHz}$ down to $10\,\text{Hz}$)(right);

amplitude jitter, the values of the detector and actuator lead to a field jitter of $0.47 \cdot 10^{-4}$.

To evaluate the effect of the loop gain and different settings of the detector noise, Fig. 3.16 shows the integrated residual phase jitter and the jitter contribution of the subsystems as function of gain for phase noise (left) and amplitude noise (right). The loop gain is swept in a range of $K_0 = 1 \ldots 400$ and the integration bandwidth is set from 10 Hz to 10 MHz.
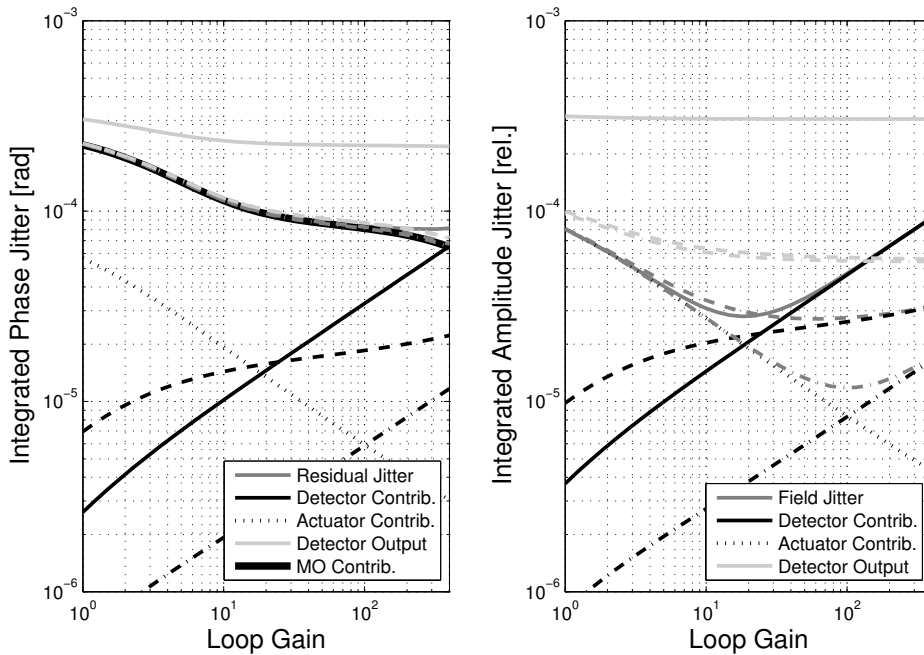

Figure 3.16: Phase and amplitude jitter contribution of the subsystems to the residual jitter for different detector settings; phase and amplitude jitter at the detector output; solid: detector 1; dashed: detector 2; dash-dotted: detector 3;

The major impact on the residual phase jitter originates in the MO contribution. The contribution of the detector is only visible for detector 1 and a loop gain up to 100. With a reduced noise floor, the detector contribution can be neglected. The actuator noise has no influence on the residual phase jitter at all.

By changing detector 1 to detector 2 or 3, the phase jitter at the detector output is reduced by a factor of approximately 3 from $3.1 \cdot 10^{-4}$ down to $1.1 \cdot 10^{-4}$ for a loop gain of 100. The 1/f-noise improvement (detector 3) has no influence on the phase jitter at the detector output.

The minimum amplitude jitter is the crosspoint of the actuator and detector contributions ($2.7 \cdot 10^{-5}$). This point is shifted to higher gain and smaller jitter values for a reduced detector noise floor, while the high 1/f-noise of detector 2 limits the minimum reachable jitter to approximately $2.4 \cdot 10^{-5}$. With the

improved detector 3 and a reduced 1/f-noise, the amplitude jitter can even be more reduced down to $1.2 \cdot 10^{-5}$.

As described for the phase jitter, the reduction of the detector noise floor reduces the amplitude jitter at the detector output from approximately $3 \cdot 10^{-4}$ (detector 1) down to $5.5 \cdot 10^{-5}$ (detector 2 and 3). The reduction of the 1/f noise from detector 2 to detector 3 has a minor influence.

3.3.1   Conclusion and Discussion

For a loop gain of $K_0 = 0$, the cavity field follows the jitter of the MO within the cavity bandwidth. If the beam phase is correlated with the phase noise of the MO, the residual cavity field jitter is imposed on the beam. Additionally, the actuator noise contribution is added. The contributed detector jitter is zero. If the loop gain K_0 increases, the closed loop bandwidth increases as well and therefore the bandwidth of the detector contribution increases, which leads to more induced jitter from the detector noise on the residual phase noise. The locking bandwidth of the field to the MO increases, therefore the residual phase noise decreases.

A problem is the evaluation of the field stability with the signal at the output of the detector. Due to the low loop bandwidth, the contribution of the detector noise is much smaller than its output noise. It can be seen as an upper boundary for the field stability. For a more accurate determination of the residual jitter, beam-based measurement techniques have to be used [27] [28] [29].

The attention concerning these simulations is focused on the high frequency fluctuations. Due to the limited loop gain, slow drifts due to microphonics lead to steady-state errors. The implementation of an additional integrating part in the controller (PI-controller) would lead to a slope on the field. This is in conflict with the requirement of field flatness, which could be solved by an adaptive feed forward.

Other forms of slow errors originate in the 1/f-component of the detector noise and in thermal drifts. They lead to measurement errors and influence the quality of the field control directly. Thermal drifts cause phase drifts of cable transmission from the cavity to the detector or phase drifts of the detector itself. Also drifts in the reference distribution system will lead to phase errors in the measurement between different LLRF stations [6].

3.4   Beam Stability

In Fig. 3.17, a schematic of the coupled and simplified LLRF systems in a linac is shown. The laser, which is used to generate the electron bunches in the RF gun, is locked to the MO by a PLL. Due to the limited loop bandwidth and because
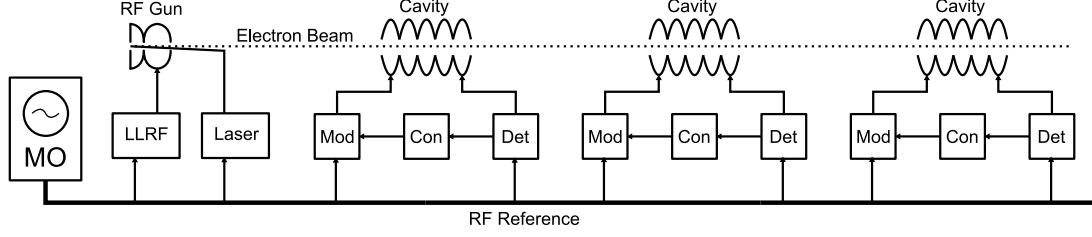
Figure 3.17: Schematic diagram of the induced jitter coupling of the LLRF system to the beam

of noise sources in the laser PLL, additional uncorrelated phase jitter is added to the laser and the generated beam.

To estimate the jitter contributions of the LLRF systems to the beam energy, it is assumed that the beam phase at the output of the RF gun is synchronized to the phase of the MO, except for the uncorrelated jitter contribution of the RF gun control loop and laser PLL.

The electron beam is accelerated by the electrical field in the cavity (Eqn. 2.10). The uncorrelated amplitude and phase jitter of the cavity field is imposed on the beam energy. The jitter contributions of each LLRF system along the linac are uncorrelated. As described by Eqn. 3.68, the accelerating voltage is affected by the amplitude stability of the cavity voltage and by the relative phase stability between the beam and the cavity field. According to [30], the energy spread induced by field instabilities can be calculated to be

$$
\left(\frac{\Delta E}{E}\right)^2 \cos^2\varphi_b = \frac{1}{2}(1 + \cos 2\varphi_b)\left(\frac{\Delta A}{A}\right)^2 \tag{3.74}
$$
$$
+ \frac{1}{2}\left(1 - \cos(2\varphi_b)\right)\Delta\varphi^2 + \frac{1}{4}\left(3\cos(2\varphi_b) - 1\right)\Delta\varphi^4.
$$

The energy spread is affected by the amplitude jitter $\Delta A/A$ and phase jitter $\Delta\varphi$ of the residual field, where φ_b denotes the beam phase (Fig. 2.10).

In Fig. 3.18, the contribution of the LLRF system to the energy spread of the beam for a beam phase of 20° is shown. These values are induced by the uncorrelated noise sources from the detector, actuator, and MO in the LLRF system. For a beam phase of 20°, the residual phase jitter contribution determines the induced energy spread at lower gain values. The amplitude jitter contribution increases the induced energy spread for gain values above 100. If the beam phase is reduced, the contribution of the residual phase noise decreases and the induced energy spread is limited by the amplitude jitter. The off-crest acceleration with a beam phase of 20° is only required for the first ACC-module (ACC1) in front of BC2 in order to guarantee bunch compression. The following ACC-modules are operating on-crest to get the highest energy gain. The induced phase jitter for these modules can be neglected. The improvement of the induced energy spread

for different detectors at high gain values stems from reduced amplitude jitter. The phase jitter is mainly affected by the MO, which is independent of the chosen detector.
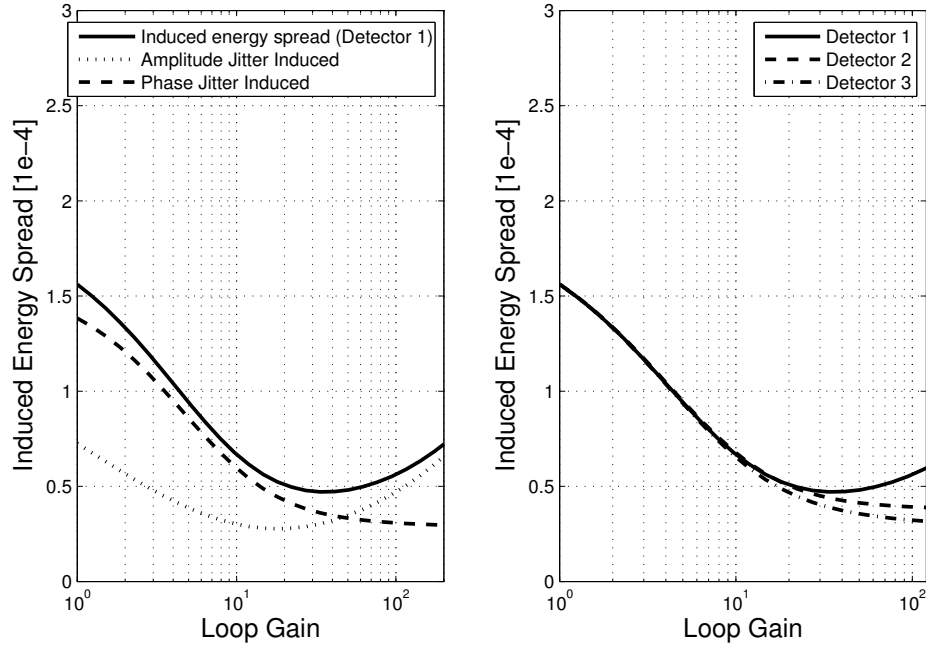

Figure 3.18: Induced energy spread of one LLRF system for a beam phase of 20°; left: composition of the energy spread by amplitude and phase induced jitter; right: influence of different detectors.

These simulation results indicate a minor influence of the noise sources of one LLRF system to the energy stability of the beam. For loop gain values above 10, the contribution of one LLRF system is below the required margin of 10^{-4}. It is caused by the small bandwidth of the cavity, which makes it sensitive to microphonics. The contribution of the high frequency noise of the detector is filtered out by the cavity, while the contributions of the actuator are suppressed by the control loop. The major contribution of the LLRF system to the phase jitter results from the MO. As long as the beam is locked to the MO, the main part of the contribution to the residual jitter is induced by the high frequency noise of the MO. If the beam is locked to the MO with loop bandwidth close or equal to the loop bandwidth of the LLRF system, the contribution is minimized. This is valid for all systems which are locked to the MO and influence the beam. The fastest system in the accelerator dominates the jitter contribution of the MO to the beam. The dominant error sources are disturbances at low frequencies from microphonics and Lorentz force detuning, and the measurement errors caused by calibration errors of the vectorsum.

3.5 Nonlinearity

In reality, for a certain power level, all electronic networks behave nonlinearly. Also passive components like connectors or filters are nonlinear strongly depending on the input power level. To estimate the compression errors, which result from the nonlinearities, a simple form of description is useful. A nonlinear network with an amplitude compression can be modeled as a polynomial with

$$v_{\text{out}}(t) = a_0 + a_1 v_{\text{in}}(t) + a_2 v_{\text{in}}(t)^2 + a_3 v_{\text{in}}(t)^3, \tag{3.75}$$

while a_0 describes the DC offset at the output, a_1 is the linear gain, and a_2 and a_3 are the second and third order coefficients of the nonlinear curve [15]. With an input signal

$$v_{\text{in}}(t) = A_{\text{in}} \sin(\omega t) \tag{3.76}$$

this equation leads to

$$
\begin{aligned}
v_{\text{out}}(t) &= a_0 + a_1 A_{\text{in}} \sin(\omega t) \\
&\quad + a_2 \frac{A_{\text{in}}^2}{2} [1 - \cos(2\omega t)] \\
&\quad + a_3 \frac{A_{\text{in}}^3}{4} [3\sin(\omega t) - \sin(3\omega t)].
\end{aligned} \tag{3.77}
$$

The output amplitudes separated into the different frequencies are

$$A_{\text{out,DC}} = a_0 + \frac{1}{2} a_2 A_{\text{in}}^2 \tag{3.78}$$

$$A_{\text{out},\omega} = a_1 A_{\text{in}} + \frac{3}{4} a_3 A_{\text{in}}^3 \qquad \text{(Fundamental)} \tag{3.79}$$

$$A_{\text{out},2\omega} = \frac{1}{2} a_2 A_{\text{in}}^2 \qquad \text{(2nd Harmonic)} \tag{3.80}$$

$$A_{\text{out},3\omega} = \frac{1}{4} a_3 A_{\text{in}}^3 \qquad \text{(3rd Harmonic)}. \tag{3.81}$$

3.5.1 Compression

The output amplitude at ω of a linear network is described by

$$A_{\text{out,ideal}} = a_1 A_{\text{in}}. \tag{3.82}$$

The amplitude gain of the network at ω is definded by the ratio of output and input amplitude at frequency ω

$$G_A = \frac{A_{\text{out},\omega}}{A_{\text{in},\omega}} = \frac{a_1 A_{\text{in}} + \frac{3}{4} a_3 A_{\text{in}}^3}{A_{\text{in}}} = a_1 + \frac{3}{4} a_3 A_{\text{in}}^2 \tag{3.83}$$

which describes the gain compression at higher input amplitude levels if a_3 is negative. The 1 dB compression point is defined as

$$-1\,\mathrm{dB} = 20\log_{10}\left(\frac{a_1 A_{-1\,\mathrm{dB}} + \frac{3}{4}a_3 A_{-1\,\mathrm{dB}}^3}{a_1 A_{-1\,\mathrm{dB}}}\right) \tag{3.84}$$

with the input amplitude $A_{-1\,\mathrm{dB}}$, where the compression error is 1 dB. The compression error can also be defined as the relative amplitude compression error

$$\left(\frac{\Delta A}{A}\right)_{\mathrm{NL}} = \frac{3}{4}\frac{a_3}{a_1}A_{\mathrm{in}}^2. \tag{3.85}$$

3.5.2   Intermodulation

With a two-tone input signal

$$v_{\mathrm{in}}(t) = A_1\sin(\omega_1 t) + A_2\sin(\omega_2 t) \tag{3.86}$$

with two closely spaced frequencies ω_1 and ω_2, the output signal of the nonlinear network consists of combinations of the frequencies in the form of

$$m\omega_1 \pm n\omega_2 \tag{3.87}$$

with $m, n = 0, 1, 2, 3, \ldots$ (Fig. 3.19). These combinations are called intermodulation products (IM products). For the investigation of nonlinearity errors, the 3rd order IM products at the frequencies $2\omega_1 - \omega_2$ and $2\omega_2 - \omega_1$ are important. They are closely located to the frequencies of interest at ω_1 and ω_2. Due to the close
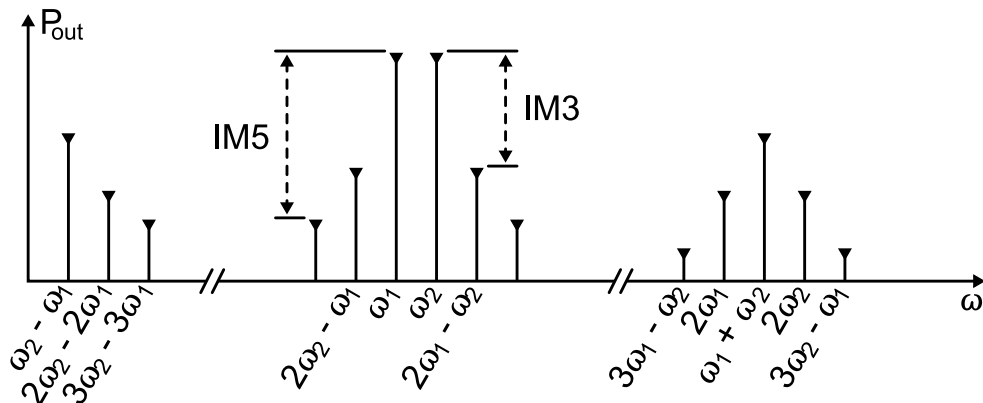

Figure 3.19: Output spectrum of a nonlinear network with two-tone input signal and second and third order intermodulation products.

location of the IM products, one can assume that the IM products are affected by

the same frequency response of the nonlinear network as the carrier. The output amplitudes at ω_1 and ω_2 are

$$
\begin{aligned}
A_{\omega_1} &= a_1 A_1 + \frac{3}{4} a_3 A_1^3 + \frac{6}{4} a_3 A_1 A_2^2 \\
A_{\omega_2} &= a_1 A_2 + \frac{3}{4} a_3 A_2^3 + \frac{6}{4} a_3 A_1^2 A_2,
\end{aligned}
\tag{3.88}
$$

and at the two frequencies closely located to the carriers

$$
\begin{aligned}
A_{2\omega_1 - \omega_2} &= \frac{3}{4} a_3 A_1^2 A_2 \\
A_{2\omega_2 - \omega_1} &= \frac{3}{4} a_3 A_1 A_2^2.
\end{aligned}
\tag{3.89}
$$

For simplification, A_1 and A_2 is set to A_{in}. This leads to

$$
A_{\omega_1} = A_{\omega_2} = a_1 A_{\text{in}} + \frac{9}{4} a_3 A_{\text{in}}^3
\tag{3.90}
$$

and

$$
A_{2\omega_1 - \omega_2} = A_{2\omega_2 - \omega_1} = \frac{3}{4} a_3 A_{\text{in}}.
\tag{3.91}
$$

The intercept point of 3rd order is a theoretical value, which is defined as the crossing point of the two lines, which result from the linear part of Eqn. 3.90 and of Eqn. 3.91 (Fig. 3.20). This leads to the equation

$$
a_1 A_{\text{IP3}} = \frac{3}{4} a_3 A_{\text{IP3}}^3.
\tag{3.92}
$$

The amplitude of the 3rd order intermodulation point related to the input is

$$
A_{\text{IP3}} = \sqrt{\frac{4}{3} \frac{a_1}{a_3}}.
\tag{3.93}
$$

The combination of Eqn. 3.85 and 3.93 results in the nonlinear compression error. This error is dependent on the input/output amplitude and input/output IP3

$$
\left(\frac{\Delta A}{A} \right)_{\text{NL}} = \frac{A_{\text{in}}^2}{A_{\text{IIP3}}^2} = \frac{A_{\text{out}}^2}{A_{\text{OIP3}}^2}
\tag{3.94}
$$

with

$$
A_{\text{out}} = G \cdot A_{\text{in}} \quad A_{\text{OIP3}} = G \cdot A_{\text{IIP3}}.
\tag{3.95}
$$

Eqn. 3.94 can also be written in terms of input/output power, which is commonly used:

$$
\left(\frac{\Delta A}{A} \right)_{\text{NL}} = \frac{P_{\text{in}}}{P_{\text{IIP3}}} = \frac{P_{\text{out}}}{P_{\text{OIP3}}}
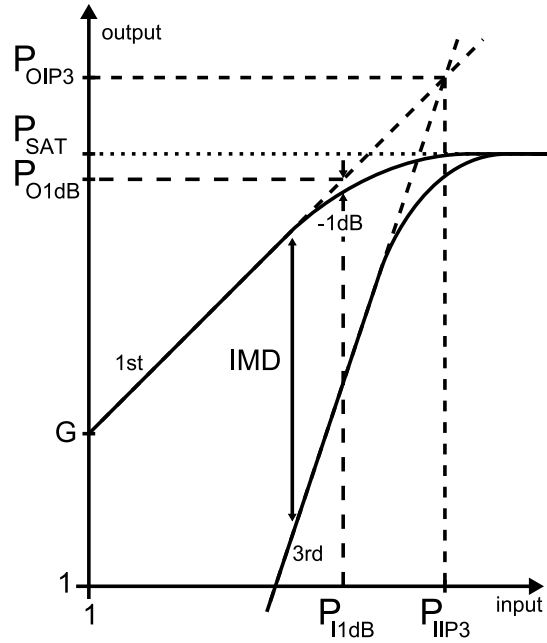\tag{3.96}
$$

Figure 3.20: Characteristic curve with input and output power of 3rd order inter-modulation products P_{xIP3}, 1 dB compression point $P_{1\,\mathrm{dB}}$, and output saturation P_{sat}.

3.5.3   AM-PM Conversion

It can be observed that not only the gain is dependent on the input amplitude but also the phase shift of a nonlinear network. For modeling these effects, Eqn. 3.75 is extended to

$$v_{\mathrm{out}} = \bar{a}_0 + \bar{a}_1 v_{\mathrm{in}} + \bar{a}_2 v_{\mathrm{in}}^2 + \bar{a}_3 v_{\mathrm{in}}^3 + \ldots \tag{3.97}$$

with complex coefficients

$$\bar{a}_n = A_n\, e^{j\varphi_n} = I_n + jQ_n. \tag{3.98}$$

With these complex coefficients, the AM-to-AM and AM-to-PM conversion can be modeled and lead to an amplitude dependent network phase shift and gain, which can be modeled separately as a function of A_{in}

$$\Phi = f(A_{\mathrm{in}}) \quad \text{and} \quad G = f(A_{\mathrm{in}}). \tag{3.99}$$

3.6   Vectorsum Calibration

The requirements for the linearity of the detector are derived from the requirements of the vectorsum calibration. As decribed in chapter 2, the control signal

of a vectorsum control is derived from the sum of multiple field vectors of one or more ACC-modules.

One ACC-module at FLASH contains 8 cavities, which are controlled by one LLRF-system[1]. The accelerating voltage is derived from the sum of the field vectors of one ACC-module, which acts like a single cavity with one field vector. This leads to the ansatz to control the vectorsum of N cavities, instead of one control system for each single cavity.

The induced pulse-to-pulse energy gain jitter of the LLRF-system is derived from the time varying fluctuations of the controlled vectorsum instead of time constant errors [8]. For the vectorsum control, it has to be considered that each single field vector of the vectorsum has to be calibrated in amplitude and phase to get the correct ratio between the real and measured field vectors of the vectorsum. Fluctuations of the field vectors due to microphonics lead to time dependent variations of the measured vectorsum and therefore to time dependent errors of the controlled vectorsum. Due to the variance of the measurement errors, the ratio of the measured vectors differs from the ratio of the real field vectors.

In general, calibration errors are constant errors and lead to constant errors in the vectorsum. Due to time dependent disturbances, like microphonics, this constant calibration error yields a time dependent measurement error of the vectorsum and therefore a limited accuracy of the control. These effects are revealed by a simple graphical model of a vectorsum with only two vectors, $\vec{V}_1$ and $\vec{V}_2$. Each field vector is moving stochastically independent and as function of time in phase with the detuning angle $\psi(t)$ due to microphonics onto the cavity, while any changes of the amplitude are negligible [9]. These changes are visible on the real vectorsum, seen by the beam, and the measured vectorsum.

If the calibration errors are zero, the control loop compensates the changes by the loop gain. Furthermore, the disturbances are reduced by $\sqrt{N}$, while N is the number of cavities in the vectorsum, because of the summation of stochastically independent fluctuations. $\vec{V}_1$ is chosen as the reference vector, which is assumed to be constant, while $\vec{V}_2$ is affected $\sqrt{2}$-times by the microphonics and calibration errors. A constant calibration error $(\Delta A/A)_{\text{cal}}$ in the amplitude primarily leads to an amplitude error $(\Delta A/A)_{\text{VS}}$ in the measured vectorsum. This error is almost constant for a small detuning angle $\psi \ll 1$.

In Fig. 3.21, an additional phase error $\Delta\varphi_{\text{VS}}$ is visible (gray curve), which is dependent on the time dependent detuning angle $\psi(t)$. The same situation can be observed for a constant calibration error $\Delta\varphi_{\text{cal}}$ in the phase and in the amplitude error $(\Delta A/A)_{\text{VS}}$ of the mearsured vectorsum in Fig. 3.22. The phase calibration error $\Delta\varphi_{\text{cal}}$ leads primarily to a constant phase error $\Delta\varphi_{\text{VS}}$ of the measured vectorsum. With the time dependent detuning angle $\psi(t)$, the amplitude error $(\Delta A/A)_{\text{VS}}$ is changing time dependently, too. To measure the vectorsum of 8

---

[1]One LLRF system is capable to control up to 4 ACC-modules, which means a vectorsum of up to 32 cavities.
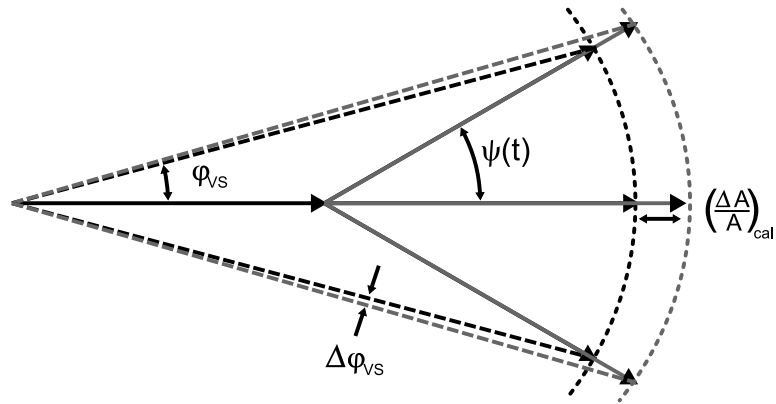
Figure 3.21: A constant calibration error in amplitude $(\Delta A/A)_{\mathrm{cal}}$ leads to a time dependent phase error of the measured vectorsum $\Delta\varphi_{\mathrm{VS}}$; black: real vectorsum, gray: measured vectorsum with calibration error;
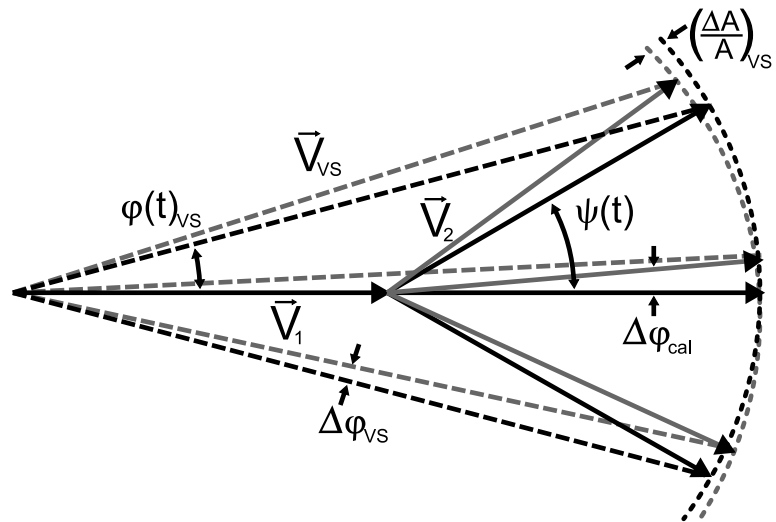

Figure 3.22: A constant calibration error in phase $\Delta\varphi_{\mathrm{cal}}$ leads to a time dependent amplitude error of the measured vectorsum $(\Delta A/A)_{\mathrm{VS}}$; black: real vectorsum, gray: measured vectorsum with calibration error;

cavities with an accuracy of 10^{-4} in amplitude and phase, the maximal allowable amplitude and phase calibration error is 1% for amplitude and 0.5° for phase [9].

Differences in the loaded Q, incident phase, and detuning of each single cavity lead to variations of the gradient of each single cavity up to 10%, while the vectorsum is constant [8]. Nonlinearities in the detector lead to amplitude dependent gain compression. With changing gradient, this results in time dependent measurement errors which are comparable with the calibration errors of the vectorsum. Hence, it can be concluded, that the requirements for the vectorsum calibration are likewise valid for the nonlinearity errors. This leads to an allowable amplitude compression of less than 1% or 0.08 dB and to a phase change of less than 0.5°.

Chapter 4

Concepts and Requirements

At the beginning of this chapter, requirements for the detector are derived, based on the proposed models, simulations, and equations. These requirements are related to a black box model of the detector, in order to be independent of the chosen concept of field detection and RF downconversion. Possible realizations are described in the next chapter. Subsequently, concepts of RF downconversion are presented and compared concerning their advantages and disadvantages. Afterwards, a description of a digital field detection algorithm is presented, which can be used for two of the presented downconversion concepts. It is planned to implement and test this algorithm at FLASH. Derived from the simulation in section 3.3, the noise contribution of the detector to the field increases, when the loop gain of the feedback system is increased. It is hence necessary to develop a detector, whose noise contribution at a given loop gain remains below the required field stability. This ensures, that the field stability in the cavity does not degrade because of the noise contribution of the detector. The linearity requirements are derived from the specifications of the vectorsum calibration, which is described in section 3.6. With the equations from section 3.5, these results are converted to boundary conditions for the linearity parameters of the detector.

4.1 Hardware Specification

Independent of the chosen detection scheme, the detector is modeled as a black box with the system parameters for a receiver, e.g. noise figure, F_{sys}, gain, G_{sys}, and third order intercept point, $P_{\text{IP3,sys}}$.

4.1.1 Detector Noise

To measure the cavity field vector within the measurement bandwidth B with a rms resolution of 10^{-4}, the upper limit of the detector noise integrated over the measurement bandwidth B should be below 10^{-4}. To get the required value
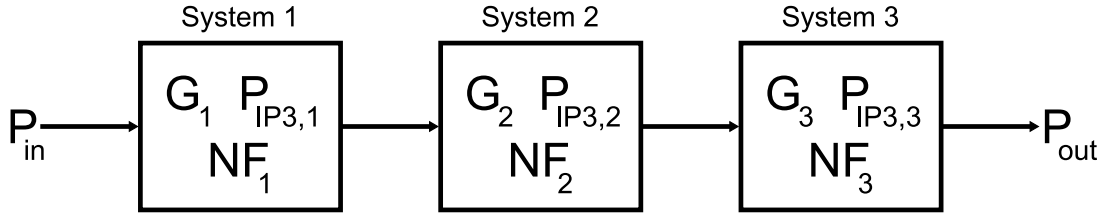
Figure 4.1: Cascaded networks with IP3, G and NF

for the white noise floor (b_0) and the 1/f-noise contribution (b_{-1}) of the power spectral density, Eqn. 4.1 defines the equivalent noise power spectral density at the input of the detector.

$$S_{\text{in}}(f) = b_0 + b_{-1}f^{-1} \tag{4.1}$$

Integrated over the measurement bandwidth $B = (f_2 - f_1)$, Eqn. 4.1 leads to an rms field error of

$$\Delta x_{\text{rms}}^2 = \int_{f_1}^{f_2} S_{\text{in}}(f)\mathrm{df} = b_0(f_2 - f_1) + b_{-1}\ln\frac{f_2}{f_1}. \tag{4.2}$$

In general, the upper boundary f_2 is in the range of 10^6 Hz to 10^8 Hz while f_1 is 10^2 Hz, so that f_1 can be neglected in the first term. The logarithm naturalis in the second term leads to a value of approximately 10. Eqn. 4.2 can be simplified to

$$\Delta x_{\text{rms}}^2 = b_0 f_2 + 10 \cdot b_{-1}. \tag{4.3}$$

To influence the integrated noise power, the 1/f-noise coefficient b_{-1} has to be 5 to 7 orders of magnitude larger than b_0 depending on f_2. In practical applications, this is not fulfilled. Therefore the 1/f-noise can be neglected and the input noise is assumed to be constant over the frequency band of interest. This leads to a simplified equation for the rms field error

$$\Delta x_{\text{rms}}^2 = b_0 \cdot B \tag{4.4}$$

with B for the measurement bandwidth of the detector, or

$$20\log_{10}(\Delta x_{\text{rms}}) = b_{0,\text{dBc}} + 10\log_{10}(B) \tag{4.5}$$

for the logarithmic scale. To determine b_0 for a given measurement bandwidth B of the detector, the following formula is used:

$$\begin{aligned} b_0 &= \Delta x_{\text{rms}}^2 \cdot \frac{1}{B} \quad [\text{s}] \\ b_{0,\text{dBc}} &= 20\log_{10}(\Delta x_{\text{rms}}) - 10\log_{10}(B). \end{aligned} \tag{4.6}$$

The measurement bandwidth B of the detector is equal to the signal bandwidth. The noise bandwidth is equal to the bandwidth of an ideal filter, which passes the same noise power as the nonideal filter, e.g. the detector. Therefore, the noise bandwidth is always higher than the signal bandwidth of a filter, depending on the filter slope and filter order, respectively [18].

A filter of first order has a noise bandwidth of 1.57 times the 3 dB signal bandwidth while the noise bandwidth of a third order filter is just 1.05 times higher. This leads to Tab. 4.1, which shows the noise power spectral density for a required measurement resolution of $\Delta x_{\mathrm{rms}} = 10^{-4}$ for different signal bandwidth.

3 dB Signal BW [MHz]	b_0 [dBc/Hz] for 1st Order LP	b_0 [dBc/Hz] for 3rd Order LP
0.01	-122	-120.2
0.1	-132	-130.2
1	-142	-140.2
10	-152	-150.2

Table 4.1: Required power spectral density parameter b_0 for a given measurement resolution of $\Delta x_{\mathrm{rms}} = 10^{-4}$ and different detector bandwidth and filter order.

The allowable maximum power spectral density of the detector for a measurement bandwidth of 10 MHz is -150 dBc/Hz. By Eqn. 3.17 and the noise power spectral density, the required noise figure dependent on the input power of the detector can be determined. The parameters F_{sys}, B, and P_{in} of the detector lead to a conditional equation for

$$
\begin{aligned}
b_0 &= \frac{F_{\mathrm{sys}} \cdot kT}{P_{\mathrm{in}}} \quad [\mathrm{s}] \\
b_{0,\mathrm{dB}} &= \mathrm{NF}_{\mathrm{sys}} + N_{\mathrm{th}} - P_{\mathrm{in,dB}} \quad [\mathrm{dB}]
\end{aligned}
\tag{4.7}
$$

Eqn. 4.6 and 4.7 yield

$$
\begin{aligned}
\mathrm{NF}_{\mathrm{sys}} - P_{\mathrm{in,dBc}} + 10 \log_{10}(B) &= 20 \log_{10}\left(\Delta x_{\mathrm{rms}}\right) - N_{\mathrm{th,dBm}} \\
\frac{F_{\mathrm{sys}}}{P_{\mathrm{in}}} \cdot B &= \Delta x_{\mathrm{rms}}^2 \cdot \frac{1}{k_B T_0} \quad \left[\frac{1}{\mathrm{Ws}}\right].
\end{aligned}
\tag{4.8}
$$

By Eqn. 4.8, the parameters F_{sys}, B, and P_{in} of the detector can be determined. For a given input power P_{in}, the noise figure F_{sys} can be determined for a given bandwidth B and a denoted resolution Δx_{rms}. A higher input power increases the resolution, while the bandwidth and the noise factor should be low.

The noise factor of the detector is defined by the choice of the internal devices and their noise factor and gain. With Friis' formula [17] one gets the overall noise figure of the system as

$$
F_{\mathrm{sys}} = F_1 + \frac{F_2 - 1}{G_1} + \frac{F_3 - 1}{G_1 G_2} + \dots.
\tag{4.9}
$$

In comparison to a receiver for communication systems, where the available input power is comparatively low and close to the noise floor, the available signal power for the LLRF detector is comparatively high. Hence, the still tolerable nonlinear distortions limit the maximum signal power level.

4.1.2 Detector Nonlinearity

To reduce the signal-to-noise ratio of the input signal of the detector and to minimize the influence of the detector noise, the available input power level has to be increased, as had been shown in the previous section. The maximum power level is limited by the available output power of the cavity and by the nonlinearities of the detector. The latter cause errors in the detected signal, while the dimension of the errors is dependent on the input power level. In section 3.5, the amplitude compression error is defined by the ratio of the input or output powers and the intercept point of third order.

$$\left(\frac{\Delta A}{A}\right)_{\mathrm{NL}} = \frac{P_{\mathrm{in}}}{P_{\mathrm{IIP3,sys}}} = \frac{P_{\mathrm{out},\omega}}{P_{\mathrm{OIP3,sys}}}$$

In comparison to Friis' formula for the noise figure, the system IP3 related to the input of a cascade of nonlinear networks can be calculated by

$$P_{\mathrm{IIP3,sys}} = \left(\frac{1}{P_{\mathrm{IIP3,1}}} + \frac{G_1}{P_{\mathrm{IIP3,2}}} + \frac{G_1 G_2}{P_{\mathrm{IIP3,3}}}\right)^{-1} \tag{4.10}$$

or related to the output of the cascade by

$$P_{\mathrm{OIP3,sys}} = \left(\frac{1}{P_{\mathrm{OIP3,1}} G_2 G_3} + \frac{1}{P_{\mathrm{OIP3,2}} G_3} + \frac{1}{P_{\mathrm{OIP3,3}}}\right)^{-1} \tag{4.11}$$

with

$$G_n = 10^{G_{\mathrm{n,dB}}/10} \tag{4.12}$$

as the power gain of the n-th network stage. The maximum input power level is defined by the full scale power level of the ADC P_{FS} and by the system gain G_{sys} of the analog front-end

$$P_{\mathrm{in,max}} = \frac{P_{\mathrm{FS}}}{G_{\mathrm{sys}}} \tag{4.13}$$

or

$$P_{\mathrm{in,max,dBm}} = P_{\mathrm{FS,dBm}} - G_{\mathrm{sys,dB}} \quad [\mathrm{dB}]. \tag{4.14}$$

The full scale power level of the ADC is a constant value and has to be equal to the output power level of the analog front-end.

$$P_{\mathrm{out}} = P_{\mathrm{ADC,FS}} = \mathrm{const.} \tag{4.15}$$

With these equations and the tolerable amplitude compression error, the required minimum OIP3 can be calculated to be

$$P_{\text{OIP3,sys}} = P_{\text{ADC,FS}} \left(\frac{\Delta A}{A} \right)_{\text{NL}}^{-1} . \qquad (4.16)$$

4.1.3 Conclusion

The noise requirements determine the system noise figure and power gain, depending on the required rms resolution, bandwidth, and ADC input power level.

$$F_{\text{sys}} \cdot G_{\text{sys}} = \Delta x_{\text{rms}}^2 \cdot P_{\text{out}} \frac{1}{k_B T_0 B} \qquad (4.17)$$

with

$$P_{\text{out}} = P_{\text{FS,ADC}} = P_{\text{in}} \cdot G_{\text{sys}} \qquad (4.18)$$

and in logarithmic scale

$$\text{NF}_{\text{sys}} + G_{\text{sys,dB}} = 20 \log_{10} \left(\Delta x_{\text{rms}} \right) + P_{\text{out,dBm}} - 10 \log_{10}(k_B T_0 B). \qquad (4.19)$$

The OIP3 of the system results from the nonlinearity requirements and determines the minimum OIP3 of the detector (Eqn. 4.16).

4.2 RF Detection

The principles of RF field detection - to measure the amplitde and phase or in-phase (I) and quadrature (Q) part of an RF signal - are all based on mixing a reference signal (LO) with the RF signal. The high frequency signal is downconverted to the base band, while different phase conditions between the RF and the LO are responsible for the resulting output signal (A, φ, I or Q). The discussed concepts are:

- Baseband Sampling (IQ- and AP-Detection)

- IQ-Sampling (switched Local Oscillator)

- IF Sampling (RF Downconversion)

- Direct Sampling

The sequence of the presented concepts illustrates the stages of development, where the actual field detection shifts from the analog to the digital domain. In the first scheme, the ADC just converts the measured fieldvector to the digital domain, while at the direct sampling scheme any field detection processing is done in the digital part of the system. No analog detection scheme is needed.

4.2.1   Baseband Sampling

The first concept described in this chapter is an analog IQ-Detector, where the RF signal is converted to the baseband and sampled with an ADC. A block diagram of an analog IQ-detector is depicted in Fig. 4.2.
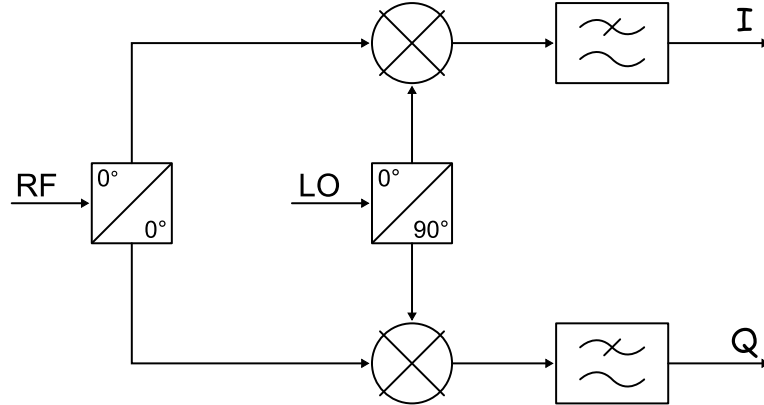

Figure 4.2: Analog IQ-Detection

The input signal (RF) is split into two branches and converted down to the baseband by multiplying it with a reference signal (LO) in two separate RF mixers. The reference signal is split by a hybrid, which leads to a phase difference of 90° between the two outputs. Behind the two mixers, lowpass filters suppress the unwanted high frequency mixing products. The two output signals correspond to the in-phase (I) and quadrature (Q) component of the input signal relative to the reference signal. The baseband signals (I and Q) are sampled with an ADC with small effort in signal processing. The amplitude and phase can be derived to read

$$
\begin{aligned}
A &= \sqrt{I^2 + Q^2} \\
\tan \varphi &= \frac{Q}{I}.
\end{aligned}
\tag{4.20}
$$

The advantage of this concept is the low effort of digital processing, due to direct I and Q sampling. The disadvantages of this scheme are the error sources of a real analog IQ-detector (Fig. 4.3). Due to phase imbalance at the output of the input splitter ($\delta\varphi_1$) or between the reference signal phase shifted by 0° and by 90° ($\delta\varphi_2$), the output signals of the mixers are not exactly I and Q. They are a combination of both, which leads to a deformation of the constellation diagram as depicted in Fig. 4.4 a). Also gain mismatch (G_I, G_Q) of the two mixer branches is present (Fig. 4.4 b)), which results from amplitude imbalance of the input splitter or gain imbalance of the mixers. Due to the baseband mixing procedure, the I and Q signals are sensitive to offsets (O_I, O_Q) at the mixer outputs (Fig. 4.4 c)). Also temperature drifts of the offset errors affect the values of the measured
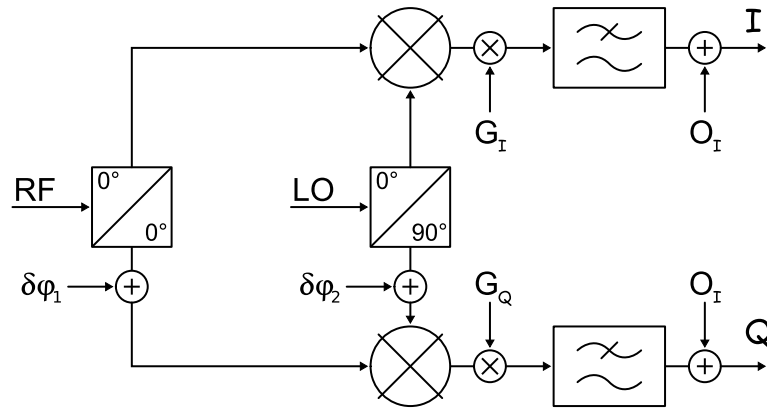
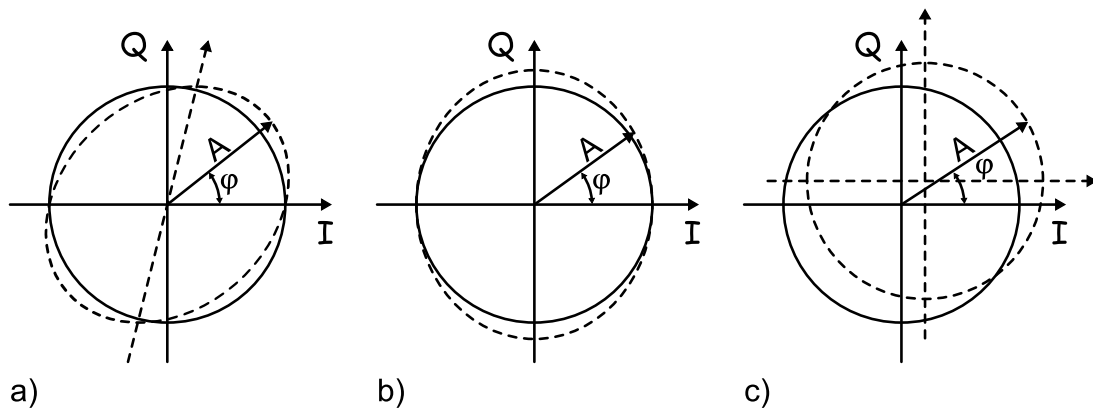Figure 4.3: Error Sources of an analog IQ-Detector

Figure 4.4: Constellation diagram with different errors on I and Q: All errors lead to phase dependent amplitude.

I and Q signal. A further disadvantage is the usage of two ADCs which leads to higher costs, more required space, and reduced reliability.

4.2.2 IQ Sampling

Using this method, the probe signal of the cavity is mixed down to the baseband with a switched LO, whose phase is switched by 90° for a fixed time interval (Fig. 4.5). The output signal of the mixer represents alternately the I, Q, -I, and
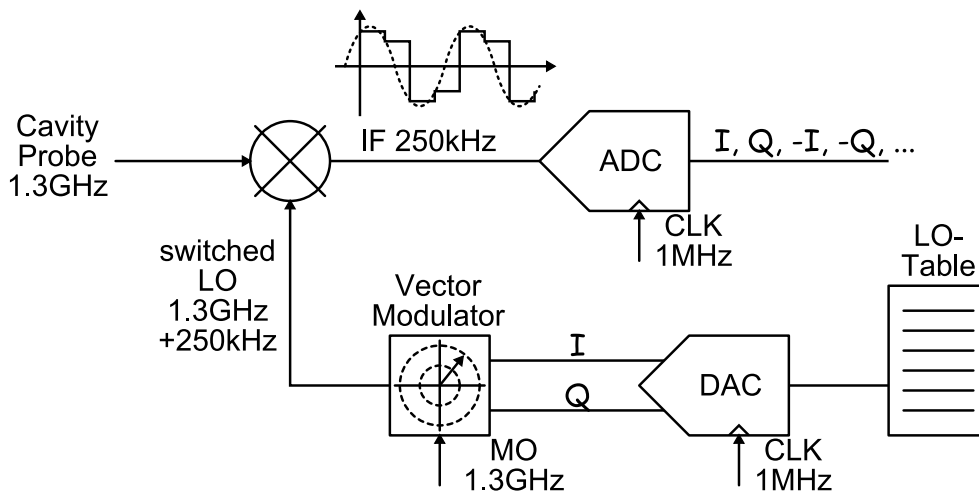

Figure 4.5: Detection scheme with RF mixer, ADC and LO-Generation as implemented at FLASH; The $1.3\,$GHz reference from the MO is switched every $1\,\mu$s by 90° with a vector modulator. The switching values are stored in a table (LO-table) and the IQ-signals are generated via a DAC. The IF signal at $250\,$kHz is sampled with $1\,$MHz. The samples correspond to subsequent in-phase and quadrature values with alternating signs of the cavity probe signal.

-Q values of the probe signal. The field vector is calculated by two subsequent samples, used as I and Q value, and shifted by $n \cdot 90°$, as depicted in Fig. 4.6.

Compared to the analog IQ-detector, where the detection is separated by two mixers, this scheme uses a time separated IQ-detection. The I and Q values are measured alternately, by phase changing the LO and with alternating sign. The technical realisation of the switched LO can be done with an electrical phase shifter or vector modulator, where the phase is changed by a controller.

One advantage of this scheme arises from baseband mixing. For the sampling of the I and Q value of the rectangle signal, the timing requirements for the ADC clock are relaxed. Furthermore, only one mixer and one ADC channel are needed. With only one mixer, the error sources of gain and phase imbalance between the I and Q mixers are removed. The sampling could be realized with a higher number of bits (16-18) and moderate sampling rates (up to $1\,$MHz) to increase the resolution.
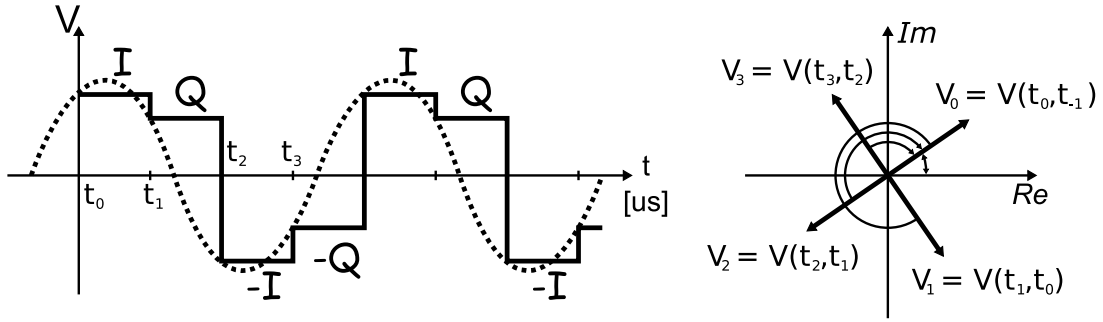
Figure 4.6: The subsequent values of the rectangular signal correspond to the in-phase and quadrature value of the complex field vector of the cavity.

Disadvantages of this detection scheme could be the error sources of the LO generation. The errors are comparable to those of an analog IQ-detector. The output of the mixer and the following amplifier stages have to have a ten times higher bandwidth or slew rate than the signal bandwidth, in order to transfer the rectangular output signal to the ADC, because a lower slew rate would smear the rectangular signals. The higher bandwidth yields more noise power at the ADC input and, depending on the sampling rate, to noise aliasing which will decrease measurement resolution. A further disavantage is the dependency of the mixer output signals on offset drifts of the mixer due to temperature changes.

The signal bandwidth has to be four times lower than the sampling frequency, because the I and Q values are each sampled by half of the sampling frequency. Hence the Nyquist frequency for the I and Q signal is $f_s/4$.

The phase step of the LO does not have to be 90°. Depending on the processing power of the digital signal processing unit, a scheme with a different phase step value is also possible. The samples are combinations of I and Q, which have to be extracted by an algorithm in the digital signal processing unit. Also, the LO does not have to be switched. For a non-zero frequency output signal (intermediate frequency, IF) of the mixer with a synchronized LO and clock signal for the ADC, the sampled IF can be interpreted as subsequent I and Q values. This leads to the scheme of IF sampling.

4.2.3 IF Sampling

For this method, the RF signal from the probe is mixed down to an intermediate frequency and afterwards sampled by an ADC (Fig. 4.7). The LO signal for downconversion and the clock signal for the sampling procedure have to be synchronized to assure a constant phase step $\Delta\varphi$ between two subsequent samples. Jitter on the LO or CLK signal leads to jitter in the phase step and thus to reduced measurement accuracy. The actual IQ detection is done in the digital signal processing unit, where the input signal is multiplied by a sine and
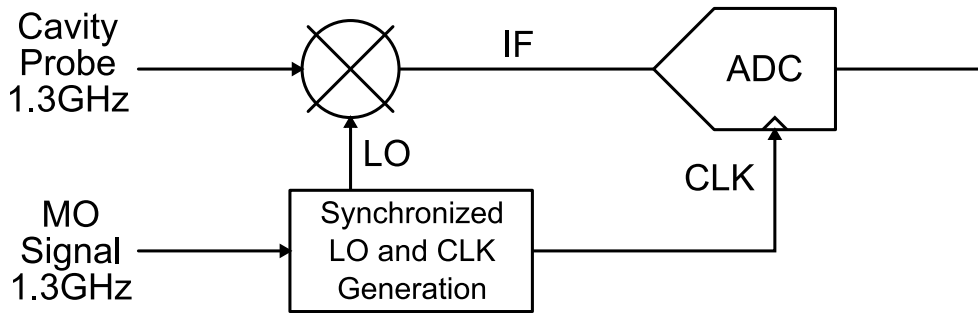
Figure 4.7: IF sampling scheme

cosine function, which is comparable with the analog IQ-detector. The advantage of this scheme is that the errors of an analog IQ-detector do not exist, e.g. phase and gain imbalance of the two multipliers. One still existent problem is the temperature dependent phase drift of the mixer.

The choice of the IF depends on different conditions. The upper limit is given by the jitter of the sampling clock and the required SNR of the ADC (Fig. 4.8) and by the linearity of the ADC buffer amplifier, which generally increases for higher frequencies. The lower limit of the IF is given by the required measuring time,
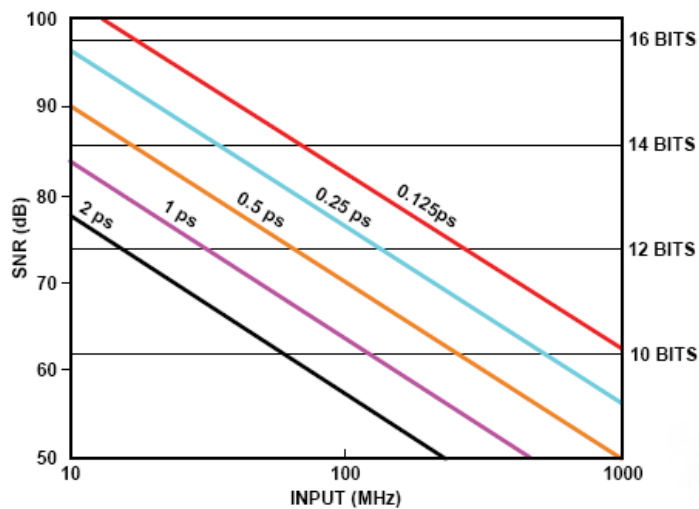

Figure 4.8: Signal-to-noise ratio of an ADC as function of the input frequency and different clock jitter values [31]

signal bandwidth, and latency of the detection algorithm. Also the generation of a synchronized LO signal has to be guaranteed.

This IQ detection scheme with an appropriate IQ detection algorithm is further investigated in the following sections. A hardware realization and the corresponding measurement results will be presented in chapters 5 and 6.

4.2.4 Direct Sampling

Nowadays, high speed 12 bit ADCs are available with sampling rates of more than 500 MSPS and analog input bandwidth of up to 1.5 GHz. These ADCs allow to sample the RF signal directly without any RF converter or IF scheme with a SNR of more than 50 dB. The advantage is the reduction of the number of input stages for preconfiguration (downconversion, filter, amplifier, etc.) which reduces possible errors and noise sources and increases reliability.

The disadvantage is the increasing impact of the clock jitter on the SNR for higher input frequencies (Fig. 4.8). This linear effect can be reduced by the process gain due to digital bandlimitation and averaging as function of the square root. For a required detection resolution of 10^{-4}, an input signal at 1.3 GHz with 10 MHz signal bandwidth, sampled with 500 MHz, leads to a required SNR of the ADC of 66 dB. This leads to an allowable clock timing jitter of up to 60 fs. With a signal bandwidth of 1 MHz and an internal digital filter with this bandwidth, the allowable jitter is increased to 200 fs. For a vectorsum of 32 cavities, it is further reduced to approximately 1 ps.

Because FLASH being a pulsed system, each single RF pulse is detected and sampled separately. A trigger signal marks the beginning of each pulse, while this trigger is synchronized with the MO. The clock signal for sampling the IF and the LO for downconversion has to be synchronized, too. Especially the sampling process has to start at the same time for each pulse, otherwise the phase of the detected signal is changed. For higher sampling rates, the trigger signal for the IQ detection has to be fast enough in order to trigger the sampling process during one clock cycle. For a sampling rate of 500 MHz, the slope has to be below 1 ns.

4.3 Digital Field Detection

Following the description of concepts of RF downconversion and digitalization in the previous sections, this section presents an algorithm which is used to derive the I and Q values from the digital data. The algorithm is based on the calculation of the Fourier coefficients of a Fourier series, the coefficients of the first order being of interest. For further applications, it could be useful to get coefficients of higher order, too.

4.3.1 Mathematical Basics

The fundamentals are delivered by the orthogonality of the sine and cosine function. This attribute allows to get the in-phase (I) and quadrature (Q) component of a sinusoidal signal in a simple manner. According to [32], the integral over the

product of a sine and cosine function leads to the following equations:

$$\frac{1}{\pi} \int_0^{2\pi} \sin(nx) \sin(mx) dx = \begin{cases} 0 & m \neq n \\ 1 & m = n \end{cases} \tag{4.21}$$

$$\frac{1}{\pi} \int_0^{2\pi} \cos(nx) \cos(mx) dx = \begin{cases} 0 & m \neq n \\ 1 & m = n \end{cases} \tag{4.22}$$

$$\int_0^{2\pi} \sin(nx) \cos(mx) dx = 0 \tag{4.23}$$

with $n, m \in \mathbb{N}$. We assume a sinusoidal input signal

$$s(t) = A \sin(2\pi ft + \varphi) = I \cos(2\pi ft) + Q \sin(2\pi ft) \tag{4.24}$$

with the amplitude A and the phase φ or the in-phase value I and quadrature value Q. The I and Q values are derived by muliplying $s(t)$ with a sine and cosine function with the same frequency and integrating over one period $T = 1/f$.

$$\begin{aligned}
\frac{2}{T} \int_0^T s(t) \cos(2\pi ft) dt &= \frac{2}{T} \int_0^T [I \cos(2\pi ft) + Q \sin(2\pi ft)] \cos(2\pi ft) dt \\
&= I \underbrace{\frac{2}{T} \int_0^T \cos(2\pi ft) \cos(2\pi ft) dt}_{=1} \\
&\quad + Q \underbrace{\frac{2}{T} \int_0^T \sin(2\pi ft) \cos(2\pi ft) dt}_{=0} \\
&= I \tag{4.25}
\end{aligned}$$

$$\frac{2}{T} \int_0^T s(t) \sin(2\pi ft) dt = \ldots = Q. \tag{4.26}$$

This corresponds to the calculation of the Fourier coefficients of a Fourier series for a periodic signal

$$s(t) = \frac{a_0}{2} + \sum_{n=1}^{\infty} [a_n \cos(n2\pi ft) + b_n \sin(n2\pi ft)] \tag{4.27}$$

with the coefficients:

$$a_n = \frac{2}{T} \int_c^{c+T} f(t) \cos(2\pi nft) \, \mathrm{dt}, \tag{4.28}$$

$$b_n = \frac{2}{T} \int_c^{c+T} f(t) \sin(2\pi nft) \, \mathrm{dt} \tag{4.29}$$

and

$$\frac{a_0}{2} = \frac{1}{T} \int_c^{c+T} f(t) \, \mathrm{dt} \tag{4.30}$$

with $T = 1/f$ the period of $s(t)$. The coefficients a_1 and b_1 are identical to I and Q.

4.3.2 Discrete Series

In our case, $s(t)$ is sampled with sampling period $T_s = 1/f_s$, and the resulting discrete series of data points $s[k]$ is

$$\begin{aligned} s[k] &= s(kT_s) = A \sin(2\pi fkT_s + \varphi) \\ &= I \cos(2\pi fkT_s) + Q \sin(2\pi fkT_s). \end{aligned} \tag{4.31}$$

Due to this discretization, Eqn. 4.28 and 4.29 for the Fourier coefficients yield Eqn. 4.32 and 4.33 with summation replacing integration

$$a_n = \frac{2}{M} \sum_{k=0}^{M-1} f(kT_s) \cos(n2\pi fkT_s) \tag{4.32}$$

$$b_n = \frac{2}{M} \sum_{k=0}^{M-1} f(kT_s) \sin(n2\pi fkT_s), \tag{4.33}$$

M is the number of samples per period T. For the coefficients of first order with $n = 1$ and the first coefficients $a_1 = I$ and $b_1 = Q$, the algorithm delivers I and Q as

$$I = \frac{2}{M} \sum_{k=0}^{M-1} s[k] \cos(k\Delta\varphi) \tag{4.34}$$

$$Q = \frac{2}{M} \sum_{k=0}^{M-1} s[k] \sin(k\Delta\varphi) \tag{4.35}$$

with $\Delta\varphi$, the phase step between two subsequent samples. The relation between the signal frequency f and the sampling frequency f_s is defined by

$$\frac{\Delta\varphi}{2\pi} = \frac{f}{f_s} = \frac{P}{S} \tag{4.36}$$

where S is the number of samples that are taken during P periods. The minimum number of samples for detecting I and Q is given by the least common multiple (LCM) of S and P divided by P,

$$M_{\min} = \text{LCM}(S, P)/P \tag{4.37}$$

whereas M could be a multiple of $M_{\min}$

$$M = n \cdot M_{\min} \quad \text{with } n = 1, 2, 3, \ldots \tag{4.38}$$

to ensure that a multiple of the period T of $s(t)$ is used. For a series of samples $s[k]$ longer than M, the series of $I[i]$ and $Q[i]$ is calculated by

$$
\begin{aligned}
I[i] &= \frac{2}{M} \sum_{k=0}^{M-1} s[k+i] \cos((k+i)\Delta\varphi) \\
Q[i] &= \frac{2}{M} \sum_{k=0}^{M-1} s[k+i] \sin((k+i)\Delta\varphi),
\end{aligned}
\tag{4.39}
$$

which describes a sliding window detection (Fig. 4.9 left). The following equa-
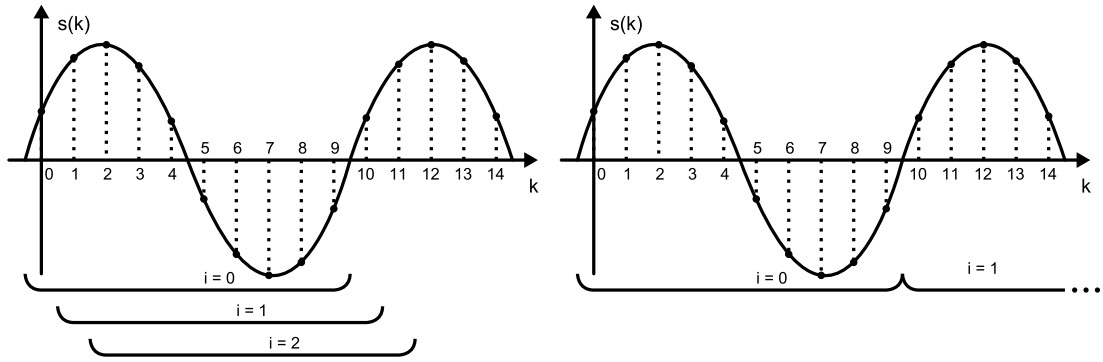

Figure 4.9: Sliding window (left) and step window (right) for digital IQ-detection algorithm

tions describe a step window detection (Fig. 4.9 right).

$$
\begin{aligned}
I[i] &= \frac{2}{M} \sum_{k=0}^{M-1} s[k+iM] \cos((k+iM)\Delta\varphi) \\
Q[i] &= \frac{2}{M} \sum_{k=0}^{M-1} s[k+iM] \sin((k+iM)\Delta\varphi).
\end{aligned}
\tag{4.40}
$$

With the sliding window detection, the spectral resolution of the detected IQ signals remains because of the high sampling rate. With the step window detection, the update sampling rate is reduced by the number of samples, which are used for one IQ pair.

4.3.3 FIR Filter and Noise

With the sum of M samples for one I and Q value, a digital finite impulse response (FIR) filter is applied with coefficients

$$
\begin{aligned}
b_I[k] &= \frac{2}{M} \cos\left(2\pi k \frac{f}{f_s}\right) \\
b_Q[k] &= \frac{2}{M} \sin\left(2\pi k \frac{f}{f_s}\right).
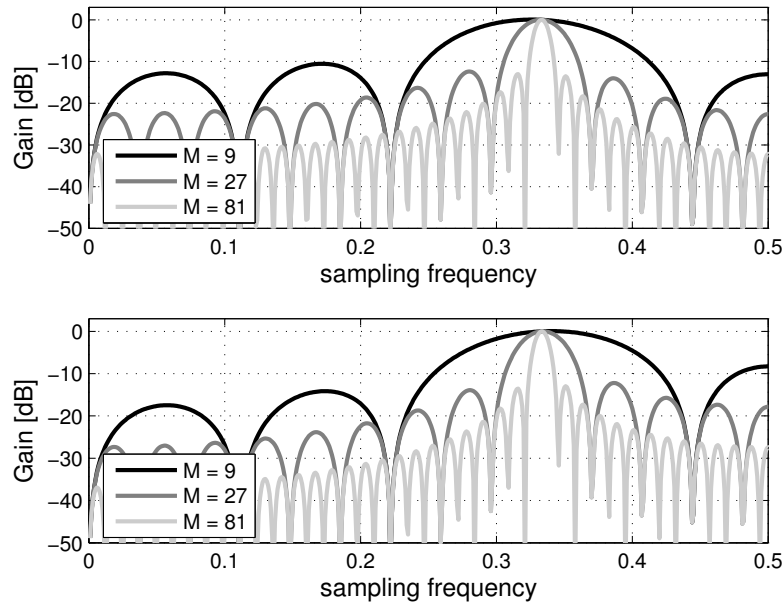\end{aligned}
\tag{4.41}
$$

Figure 4.10: Transfer functions of the FIR filter for the in-phase (top) and quadrature (bottom) value, for $P = 1$ and $S = 3$

The transfer function is given by

$$
\begin{aligned}
H_I(z) &= \sum_{k=0}^{M-1} b_I[k] \cdot z^{-k} \\
H_Q(z) &= \sum_{k=0}^{M-1} b_Q[k] \cdot z^{-k}
\end{aligned}
\tag{4.42}
$$

and the amplitude response is depicted in Fig. 4.10. The filter function has a bandpass characteristic, while the bandwidth of the detection is dependent on the number of samples M. This allows to implement a noise reduction filter.
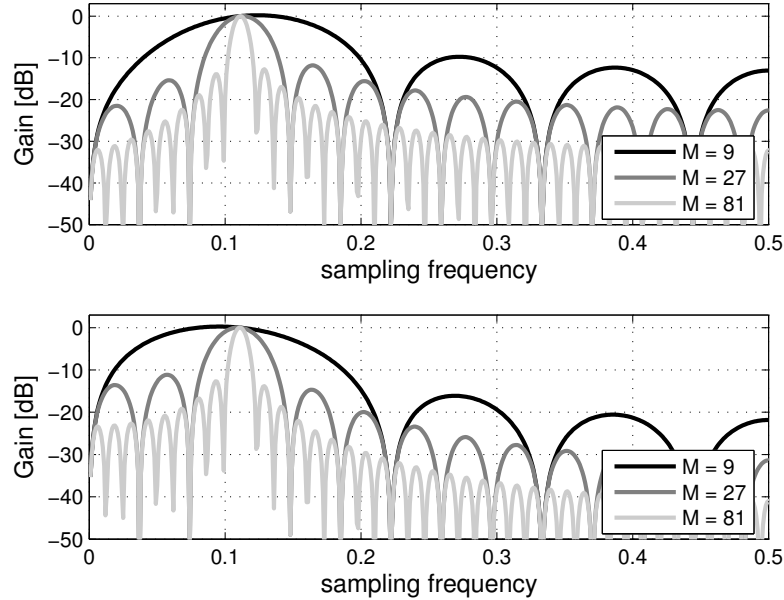

Figure 4.11: Transfer functions of the FIR filter for the in-phase (top) and quadrature (bottom) value, for $P = 1$ and $S = 9$

4.3.4   Effects of Nonlinearities

Nonlinearities in the analog front-end or the ADC generate harmonics, which can be aliased down to the first Nyquist band and disturbe the measurement of the sampled signal. One can distinguish two cases:

In the first case, a higher harmonic is aliased down to the wanted signal. This results in a constant error. However, it is dependent on the phase of the detector input signal. The phase of the n-th harmonic changes n-times faster than the fundamental phase. As a result of phase shifts in the cavity signal due to microphonics and Lorentz force detuning, this error leads to a time dependent error.

The second case occurs, when the harmonics are aliased close to the wanted signal. If the aliased harmonic is within the bandwidth of the digital filter function, it acts like modulation sidebands and will produce amplitude and/or phase modulation on the wanted signal, which yields a time dependent error, too.

The singularities of the FIR filter (Fig. 4.10 and 4.11) depend on the number of samples M taken for calculating the I and Q values. The positions of these

singularities are

$$f_0 = m \cdot \frac{f_s}{M}, \quad m = 1, 2, \ldots \tag{4.43}$$

except when f_0 is equal to f. The harmonics of the frequency f generated by the detector nonlinearities are

$$f_n = n \cdot f = n \cdot \frac{f_s}{S} P, \tag{4.44}$$

while all harmonics are aliased to a singularity, unless they are aliased to f. The above mentioned second case does not occur, if the Eqn. 4.36 and 4.37 are valid. With different coefficients of the digital FIR filter, the detection can be tuned to another frequency. To detect the n-th harmonic, the coefficients are

$$\begin{aligned} b_I[k] &= \frac{2}{M} \cos\left(2\pi k \frac{n f}{f_s}\right) \\ b_Q[k] &= \frac{2}{M} \sin\left(2\pi k \frac{n f}{f_s}\right). \end{aligned} \tag{4.45}$$

This could be used to measure the nonlinear distortions and correct this compression during detection. One problem could, however, be the small SNR of these harmonics.

Chapter 5

Hardware Development

From the simulation results in chapter 3, the optimal loop gain value for minimum noise contribution of the LLRF system to the cavity field can be determined. The possibilities to improve the noise contribution of the detector in order to increase the optimal loop gain value will be discussed in the following chapter. In the previous chapter, different types of RF detection schemes had been presented. The realization of one of them is described in this chapter. Based on the results and experiences of the realization, and the blackbox model of chapter 4, criteria for an optimization are set up.

Because of the usage of a digital LLRF control scheme, the analog signals from the cavities have to be digitized by ADCs. The disadvantage of an ADC is its finite resolution, depending on the possible number of bits, which leads to a limitation of the whole detector resolution. Therefore, the ADC will be included in the detector development in order to improve selection and matching.

The IF sampling scheme is chosen, because the baseband sampling exhibits more error sources and requires two ADCs instead of one. The IQ-Sampling, on the other hand, requires a higher analog bandwidth due to the switched signals, which leads to aliasing. Compared to the direct sampling scheme, the requirements for the signal processing unit for the IF sampling scheme are less demanding. For the injector linac, the SNR values of the high speed ADCs which are available nowadays, are too low for direct sampling at an input frequency of 1.3 GHz.

The IF sampling scheme allows to operate a manageable sampling rate and an intermediate frequency value with moderate complexity of the analog front-end, while the requirements for signal processing are feasible. Nevertheless, the requirements for the synchronized LO and CLK signals have to be kept in mind.

5.1   IF Sampling Detector

Compared to a classical receiver in communication systems, where the power level of the detectable signal is up to -50 dBm (SNR of about 54 dB for 10 MHz signal bandwidth), the power level of the cavity probe signal is very high (up to +30 dBm for a maximum gradient of 25 MV/m), which leads to an available SNR of 134 dBm for 10 MHz bandwidth. The actual difficulties to realize the high level detector are the nonlinearities of the analog front-end and the limited resolution and full scale input voltage range of the ADC.

Nowadays available high resolution ADCs with 14 - 16 bits and sampling rates up to 100 MHz deliver a SNR of 70 - 80 dB for a bandwidth of half of the sampling rate. With a signal bandwidth of 10 MHz (1 MHz), the SNR can be increased by a factor of 10 dB (20 dB). The full scale input voltage is limited to a range of 2 - 2.5 V_{pp}, which leads to an input power range of 10 - 12 dBm at 50 Ω. The implication of the ADC to the detector development requires a readout system and a desired pre-processing for the digital data. Therefore, a modular concept is chosen, which is based on a digital motherboard with pluggable mezzanine cards, where the analog front-end and the ADC are provided on. This concept is preferred to a complete design on one PCB for the possibilities of changes in the analog front-end and of an ADC exchange. It is planned as a test enviroment for different applications in diagnostics (beam arrival monitor (BAM) [27] or beam position monitor (BPM) [28]), too. Furthermore, an electrical decoupling is desired, in order to reduce pertubations from the digital part, while the analog front-end and the ADC are separated. The connection of both is realized with a transformer, which provides a galvanic isolation and separates the analog and digital ground[1].

The detector has to provide 8 channels, which are connected to the 8 cavity probes of one ACC-Module (q.v. chapter 2). The limited space requires a sophisticated design to place 8 channels on a VME-sized board (210x160 mm) and to avoid crosstalk between adjacent channels. Due to the limited isolation of the mixer ports, especially for the RF and LO port, the RF signal from one channel is distributed spuriously via the LO distribution network to the other channels and perturbs the measurements. This holds for the power supply network, too. Crosstalk along the PCB itself can be reduced by an advanced design, like separated ground layers, no parallel routed RF lines close together, or short distances between RF components.

Additionally, a metal housing for the analog front-end and the ADC is designed for mounting the mezzanine cards to the motherboard and shielding the susceptable detector electronics. It provides a stable ground for the cavity pickup signals, which are distributed over 20 - 30 m long cables from the cavity pickup to the input of the detector. For further developments, the packaging density has

---

[1]Only conditionally correct, because of the ADC input belonging to the analog part.

to be increased in order to provide more than 8 channels (up to 16 or 24) on one PCB. The integrated circuit components of the detector should be available from industry, whereas in-house developments should be avoided.

5.1.1 Selection of Components

The RF mixer and the ADC are the essential components of the detector. The mixer is mainly responsible for the linear operation of the detector, while the ADC limits the required resolution. The selection of these devices is described in the next section, where different types of RF mixers and ADCs are presented and compared.

Mixer Selection

The contribution of the mixer to the overall detector noise is comparatively low. Due to the high input power, the linearity requirements for the mixer are more important. Traditionally, for a linear conversion of the mixing process, the mixing device has to have an appropriate characteristic and the power level at the LO port has to be higher than at the RF port [14].

One has to distinguish between active and passive mixers. The active mixers commonly offer an amplification from the RF port (input) to the IF port (output) and require an external power supply. Mainly, they are based on transistor circuits (Gilbert-cell mixer) or diodes (double balanced mixer) with internal buffer amplifier for the RF or IF port. Passive mixers are lossy networks and require no external power supply. They are based on diode circuits and the required power for driving the diodes is delivered by the LO. The advantage of active mixers is their conversion gain, which is mostly in the range of up to 7 dB, while passive mixers are characterized by a conversion loss. Due to the active elements (transistors, buffer amplifiers) in the active mixer, the internal noise sources are comparatively higher than in the passive mixer, and the noise figure of an active mixer is in the range of 12-14 dB. The main cause for a degradation of the SNR by passive mixers is a result of the conversion loss, so that the mixer is comparable in its noise behavior to an attenuator. In good approximation, the noise figure of a passive mixer is the inverse of the conversion loss [14].

The required LO power level to switch the diodes of a passive mixer is higher than for an active mixer. For passive mixers, it is necessary to have a considerably higher LO power level than the input power level. The lower the difference between the LO and input power level, the lower is the grade of linearity. This results from the small signal condition being broken. The nonlinear characteristic of the diode affects the input signal, too.

Passive mixers are classified in different types of required LO power levels. Depending on the power level, the mixers are named low, middle, and high power mixers. Low power usually means 7 dBm, middle is equivalent to 13 dBm and

high is defined from 17 dBm up to 21 dBm (27 dBm) power level for the LO input. Meanwhile, manufacturers deliver high level passive mixers with internal LO buffers, which allow to provide LO power level in the range of 0 dBm, but with the performance of a high level passive mixer.

Active mixers deliver a better isolation between the input and output ports of the mixer. This is an important point for multichannel applications, where crosstalk between adjacent channels causes problems. The main contribution of the crosstalk originates in the LO-distribution and the poor isolation of the RF and LO port. The isolation is mainly affected by the matching of the mixer ports.

Tab. 5.1 shows some available mixer ICs from different companies and their parameters in the frequency band around 1.3 GHz. The HMC483 [33] is cho-

Typ	G [dB]	NF [dB]	IP1dB [dBm]	OIP3 [dBm]	LO [dBm]	R-L Iso [dB]	L-I Iso [dB]
HMJ7	-8.5	10.5	23	25.5	21	-24	-30
SYM-25DHW	-6.4	6.4	9	23.6	20	-37	-28
HMC483	-9	9	26	28	0	-14	-10
LT5527	3	12	9	27	0	-43	-50
LT5557	3	10.5	8.8	28.5	-3	-50	-42
AD8342	3	12	8	27	0	-55	-27
AD8343	4	13	3	22	-10		-50

Table 5.1: Typical mixer parameters for an RF of 1.3 GHz and IF of 50 MHz (10-70 MHz) based on datasheets.

sen for the further development. In comparison with the other mixers in Tab. 5.1, the input compression point (IP1dB) is maximum and the noise behavior is acceptable. It is a highly linear double balanced mixer with an output IP3 of 28 dBm and a conversion loss of $L = 9$ dB at 1.3 GHz. A further advantage of this high level passive mixer is the internal LO buffer, which reduces the required LO power to a range of 0 dBm. The IF bandwidth of the mixer is up to 350 MHz. A disadvantage of this mixer, on the other hand, is the low isolation between the three mixer ports.

ADC Selection

For the digital conversion and sampling of the IF signal, a high speed, high resolution ADC is required. In Tab. 5.2, parameters from the datasheets of different types of ADCs are summarized for an input frequency band of 30 to 70 MHz. The main parameters of interest are the SNR and the spurious free dynamic range (SFDR). For the concept of IF sampling, a low internal ADC jitter is required. The LTC2207 [34] was chosen due to the high SNR, the low internal jitter, and the small package size (7x7 mm). The AD9446 [35] possesses

Typ	Bits	$f_{s,max}$ [MSPS]	SNR [dBFS] 70 MHz	SFDR [dBc] 70 MHz	V_{FS} [V_{pp}]	t_j [fs]
LTC2207	16	105	77.5	90	2.25	80
LTC2208	16	130	77.5	90	2.25	70
AD6645	14	80	73.5	87	2.2	100
AD9461	16	130	77	84	3.4	60
AD9446	16	100	79	89	3.2	60
ADS5546	14	190	73.5	87	2.0	150

Table 5.2: Typical ADC parameters for an input frequency of 70 MHz based on datasheets.

a better SNR, but its package size is two times larger (16x16 mm), and the power consumption of up to 2.8 W is much higher than that of the LTC2207 with 1 W. With the small package size of the LTC2207, it is easily feasible to assemble 8 detector channels on one VME-size board.

5.1.2   The Prototype Detector

A block diagram of the detector based on HMC483 and LTC2207 is depicted in Fig. 5.1. To keep the noise contribution of the analog front-end as low as possible, a complete passive structure is built. Due to the high available input
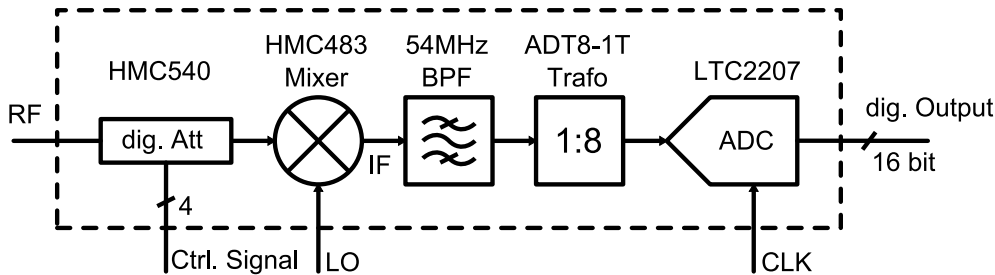

Figure 5.1: Block diagram of the detector based on HMC483 and LTC2207

power of the cavity probe signal, the conversion loss of the passive front-end can be compensated. The high input power leads to a high SNR at the detector input, while the first stages have to handle these high power levels and require high linearity.

At the input of the detector, a digitally controlled attenuator (HMC540 [33]) is used to set the high input power level to an optimal operating point of the subsequent sections, which means -1 dB below full-scale operation of the ADC input. The HMC540 is a 4 bit digital attenuator with 1 dB attenuation steps and a maximum attenuation value of 15 dB. The insertion loss is about 1 dB at 1.3,GHz and the input IP3 is 50 dBm (0 - 4 dB) and 45 dBm (5-15 dB), respectively. This

leads to an amplitude compression error below 1% for a maximum input power
of 20 dBm. The control lines of the input attenuator are filterd with RC-filter
arrays to avoid crosstalk to the other receiver channels. The coupling between
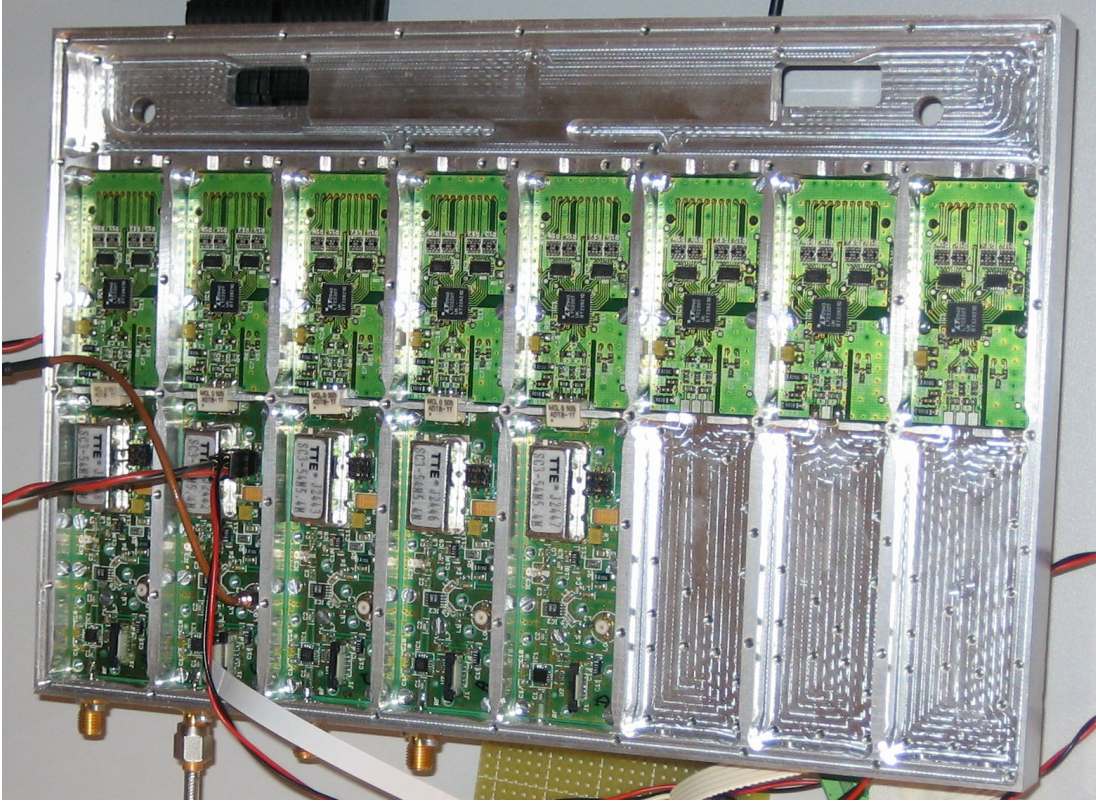

Figure 5.2: Photo of the detector chassis

the mixer and the ADC is done by a filter and a step-up transformer. The IF
bandpass filter behind the mixer suppresses the unwanted mixing products and
avoids aliasing of frequency components which are not in the band of interest. It
is realized as a lumped element LC Chebychev bandpass filter of third order and
delivered by industry [36].

The step-up transformer (ADT8-1T [37]) is used for transformation of the
single-ended output signal of the filter to a differential input signal at the ADC
input. Furthermore, it adds an offset voltage which is required for the internal
ADC input stage. With an impedance ratio of 1:8, it provides a noiseless voltage
gain of 2.83 or 9 dB, while the impedance at the ADC side of the transformer
is stepped up to $400\,\Omega$. A higher step-up ratio was tested (up to 1:16), but the
source impedance of the driving signal should not be higher than $400\,\Omega$, otherwise
the internal sampling capacitors of the sample-and-hold stage are not completely
loaded during the sampling time. This leads to a reduced detected signal level
and to higher distortions. The design of the ADC board is extracted from the

evaluation board and realized as described in the datasheet [38].

The LO distribution, the power supply, and the distribution of the digital control signals for the input attenuators are provided by a further PCB, which is placed in the metal housing, too. All distributions to each channel are done by cabling, while the clock signal and the power supply for the ADCs are provided by the digital motherboard and additional connectors for each channel.

5.1.3 Frequency Selection

A sampling frequency of 81 MHz is chosen, while the IF is 54 MHz and the LO frequency is 1354 MHz, respectively. This frequency constellation leads to an undersampling scheme. The minimum number of samples for the detection of one pair of IQ values is 3 samples in order to fulfill Eqn. 4.25 and Eqn. 4.26. They are taken during 2 periods of the IF. This leads to a maximum bandwidth of the detection of 27 MHz and a minimum detection time of 37 ns, respectively. For a required signal bandwidth of 10 MHz, 9 samples have to be taken for IQ detection, which leads to a bandwidth of 9 MHz. For a bandwidth of 1 MHz, 81 samples are necessary.
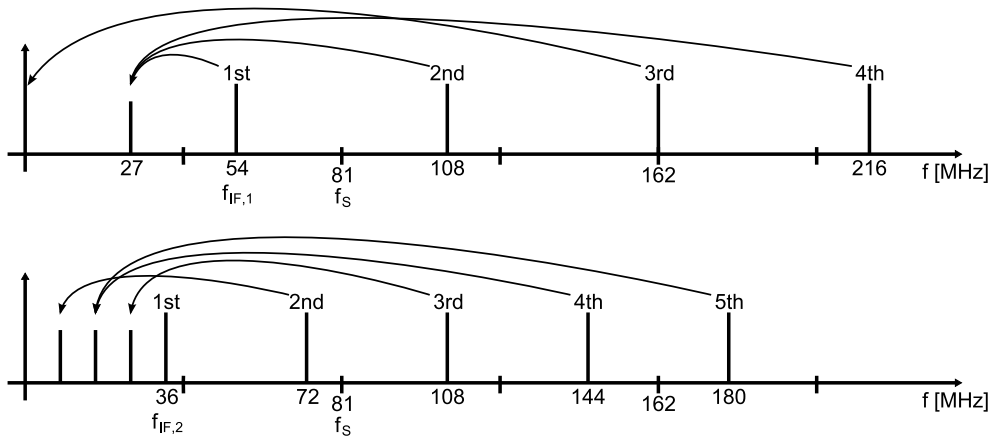

Figure 5.3: Aliasing of harmonics of $f_{IF,1} = 54$ MHz (top) and $f_{IF,2} = 36$ MHz (bottom) at a sampling frequency f_s of 81 MHz.

A disadvantage of this frequency constellation is the aliasing of the higher harmonics (2nd, 4th, and 5th) of the 54 MHz signal down to 27 MHz as depicted in Fig. 5.3 (top) which leads to distortions. Therefore, an IF-filter between mixer and ADC must be provided.

An alternative IF of e.g. 36 MHz would avoid this aliasing. All harmonics are aliased to different frequencies in the first Nyquist band (Fig. 5.3 (bottom)). The minimum number of samples required for IQ detection is increased to now 9 samples (during 4 periods of IF), which leads to a maximum measurement bandwidth of 9 MHz or detection time of 111 ns.

5.1.4   Performance Estimation

To estimate the performance of the detector with respect to noise and linearity, the noise figure NF_{sys} and the third order output intercept point $OIP3_{sys}$ of the detector are calculated. The parameters for each stage are shown in Tab. 5.3. The

	high level Att.	digital Att.	HMC483 Mixer	BP-Filter	1-to-8 Transf.	ADC
NF [dB]	10	8	9	1	1	35
G [dB]	-10	-8	-9	-1	9	/
OIP3 [dBm]	100	37	28	100	100	/
P_{in} [dBm]	30	20	12	3	2	11
P_{out} [dBm]	20	12	3	2	11	

Table 5.3: System parameters for each converter stage

high level attenuator at the detector input is used to decrease the available power level of the cavity probe of 30 dBm down to an adequate power level of 20 dBm for the digital attenuator, while the digital attenuator is set to an attenuation level of 8 dB to get an IF power level of 11 dBm at 50 Ω at the ADC input. The OIP3 of the attenuator is dependent on the set attenuation level.

The ADC noise figure of 35 dB is determined by the SNR of 74 dB, a sampling frequency of 81 MHz, and for full-scale operation of the ADC [18]. The overall noise figure NF_{sys} of the detector amounts to 54 dB, while the system third order output intercept point, $OIP3_{sys}$, is 33 dBm and the system gain, G_{sys}, is −19 dB.

The calculated equivalent input white noise floor of −150 dBc/Hz integrated over the measuring bandwidth of 9 MHz results in a rms jitter of $0.95 \cdot 10^{-4}$ for amplitude and phase (radian). For a detection bandwidth of 1 MHz, the rms jitter is $0.32 \cdot 10^{-4}$ for both amplitude and phase (radian).

With an output intercept point of $OIP3_{sys} = 33$ dBm, the amplitude compression error of the detector reads 0.6% at full scale operation of the ADC. The complete characterization and measurement results of the prototype are presented in chapter 6.

5.2   Detector Optimization

For optimization of detector performance, especially the linearity performance, a structure based on the prototype circuit described in the previous section is used. The block diagram is shown in Fig. 5.4.

The mixer (stage 2) and the ADC (stage 4) are the main components of the prototype circuit and determine the essential parameters for detector development. The optimization parameter is the gain value of a feasible amplifier
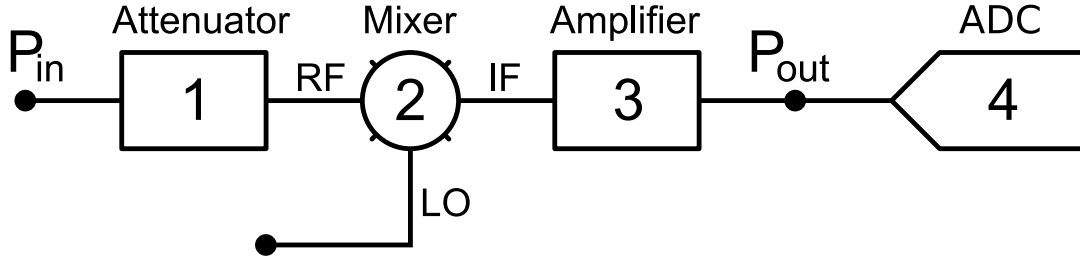
Figure 5.4: Detector based on HMC483 as stage 2 (Mixer) and LTC2207 as stage 4 (ADC). The first stage is an attenuator and the third stage is an amplifier.

(stage 3) between mixer and ADC, while the first stage is assumed to be an attenuator in order to adjust the input level for getting an IF power level of 11 dBm at 50 Ω at the ADC input.

The LLRF system is based on a digital control loop, which requires digitized signals from the detector. The first constraint describes the maximum output power $P_{\mathrm{out,FS}}$ of the detector, which is related to the full scale (FS) operation of the ADC to exploit its full resolution. With this condition for the output power and the requirements for a maximally acceptable nonlinearity amplitude error $(\Delta A/A)_{\mathrm{NL}}$, the power level of the intercept point of 3rd order of the complete detector $P_{\mathrm{OIP3,sys}}$ can be determined (Eqn. 4.16). It describes the nonlinear behavior of the complete detector. For a maximum ADC input voltage of 2.25 V_{pp} at 50 Ω, the equivalent full scale input power of the ADC or the maximum output power of the analog front-end $P_{\mathrm{out,FS}}$ is 11 dBm. With a feasible amplitude compression error of $(\Delta A/A)_{\mathrm{NL}} \leq 1\%$ (Section 3.6), the $P_{\mathrm{OIP3,sys}}$ has to be larger than 36 dBm.

With a step-up transformer with an impedance ratio of 1:8, the input impedance at the ADC is increased to 400 Ω and the equivalent input power of the ADC is decreased to 2 dBm, while the $P_{\mathrm{OIP3,sys}}$ can be larger or equal to 26 dBm.

$$P_{\mathrm{OIP3,sys}} = \left(\frac{1}{P_{\mathrm{OIP3,1}} G_2 G_3} + \frac{1}{P_{\mathrm{OIP3,2}} G_3} + \frac{1}{P_{\mathrm{OIP3,3}}} \right)^{-1} \qquad (4.11)$$

The smallest denominator in Eqn. 4.11 determines the OIP3 of the whole system. If one assumes an amplifier for the last stage in the cascade in front of the ADC, the contribution of the first stages decreases by the amplifier gain. This means, that the OIP3 of the amplifier dominates the system OIP3. If the gain of the last stage is increased, the input level of the first stage can be decreased for a constant output level. With a lower input level, the power level of the subsequent stages are also lower, and their contribution to the compression error decreases. It is also obvious, that the gain of the first stage does not influence the contribution of the OIP3 of the subsequent stages to the system OIP3, contrary to the noise figure.

The limitation of the gain value is given by the amplified noise contribution of the analog front-end. The noise of the ADC is the maximal contribution to the overall noise of the whole detector. If the gain increases, the noise of the analog front-end will be amplified and increases, too. The maximum gain value is reached, if the amplified noise contribution of the analog front-end is of the order of the ADC noise. An optimal operating point of the detector, where both
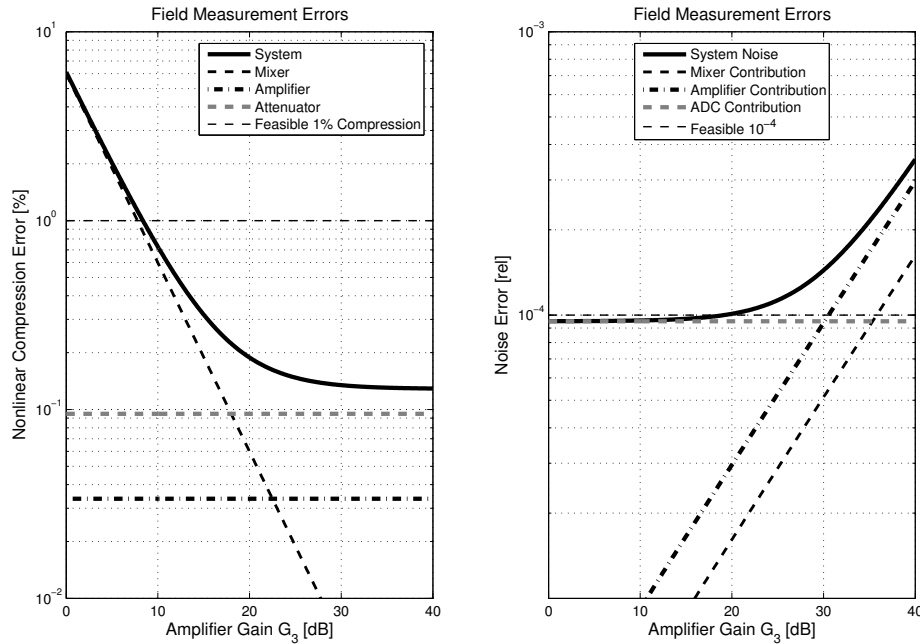

Figure 5.5: Contribution of compression error (right) and noise (left) as function of amplifier gain; amplifier settings at 70 MHz (based on LTC6401-20): IIP3 = 30.5 dBm, NF = 6.1 dBm;

the compression and the noise contribution are below their required value, can be determined with respect to the gain of the amplifier. It depends on linearity and noise of the previous stages. The limits of the noise contribution and tolerable deviations from linearity are the ADC noise and the compression error of the amplifier, respectively, which is affected by the frequency, too. This leads to an additional argument for a lower IF.

Chapter 6

Measurement Results

In this chapter, the performed tests and obtained results of the field detector are described. In the first part, the detector is characterized in the laboratory. Two different signal generation set-ups are described and compared and the used measurement set-up is presented.

The characterization of the detector is mainly focused on its noise and linearity performance. The noise performance is determined by the SNR and the measured rms amplitude and phase resolution. Both values are dependent on the detection bandwidth. The required rms amplitude and phase resolution for a detection bandwidth of $1\,\mathrm{MHz}$ are both 10^{-4}. The linearity performance is determined by measuring the intercept point of third order (IP3) by a two-tone test. This value leads to the compression error depending on the amplitude of the operating point. The requirements of the vectorsum calibration lead to a tolerable compression error of 1% in amplitude and of $0.5°$ in phase. Further tests are performed to determine the channel-to-channel crosstalk and the temperature coefficients for amplitude and phase.

In the second part of this chapter, the detector is tested in the accelerator environment. The main purpose is to evaluate the measurement resolution of the detector embedded in a perturbed system supporting signals of the accelerator environment. Afterwards the detector is integrated in the control loop and the thus achieved field stability is determined.

6.1 Single Channel Characterization

The first characterization of a single detector channel was done in the laboratory under almost ideal conditions. Here pertubations from the accelerator environment are not present. There are neither high voltage switching devices like the modulator of the klystron nor a lot of digital electronics embedded in the measurement set-up. The digital readout board (ACB2.0) was not ready during these tests and not all detector boards were assembled. Therefore, only single channel

77

tests were performed. The readout of the digital data of the ADC was done with
a logic analyzer and two 16 Bit probes. A maximum of two detector boards could
be tested in parallel. The signal processing and data analysis (IQ detection) was
done offline with MatLab.

6.1.1 LO and CLK Generation

For the laboratory characterization of the detector, three test signals had to be
generated: the RF input signal at 1.3 GHz with an adjustable power level, the
LO signal for the mixer at 1.354 GHz with 0 dBm power level, and the sample
clock (CLK) for the ADC at 81 MHz with approximately 10 dBm power level.

To assure measuring the resolution of the detector and not the quality of
the signals, correlated signals for the RF, LO, and CLK inputs had to be used.
Especially uncorrelated phase jitter on the three test signals will be seen as phase
jitter on the measured signal. It cannot be distinguished between detector induced
jitter or generator induced jitter. The amplitude jitter of the RF signal generators
is comparatively low and can be neglected.

The first trial was done with three separate RF signal generators (3GEN set-
up), which are synchronized via the 10 MHz reference signal at the rear panel
of the generators to guarantee a synchronized phase. The disadvantage of this
scheme is the limited locking bandwidth of the internal PLL of each generator,
which leads to less correlated phase jitter, especially for low frequency jitter below
100 Hz. The second set-up for test signal generation is depicted in Fig. 6.1. This
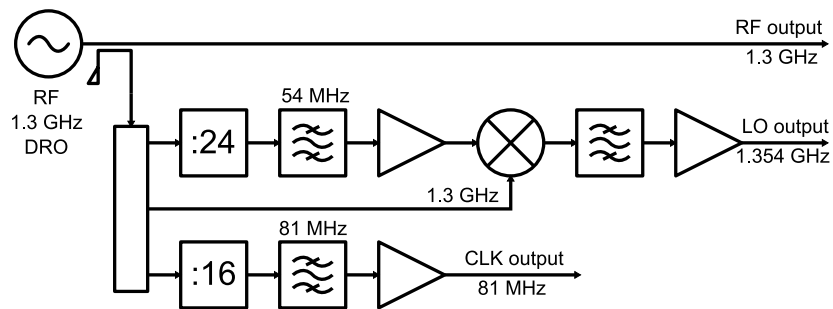
Figure 6.1: Signal generation set-up

signal generation set-up (DIV set-up) has been chosen to assure correlated phase
jitter on all three input signals, except for phase noise from the used amplifier
and frequency dividers. A 1.3 GHz Dielectric Resonator Oscillator (DRO) [39]
was used as RF input and as reference for LO and CLK generation. The LO
signal is generated by dividing the 1.3 GHz by 24 and mixing it with the 1.3 GHz
again. The CLK signal was generated by dividing the 1.3 GHz by 16. Amplifiers,
attenuators, and filters were used to adjust signal levels and suppress unwanted
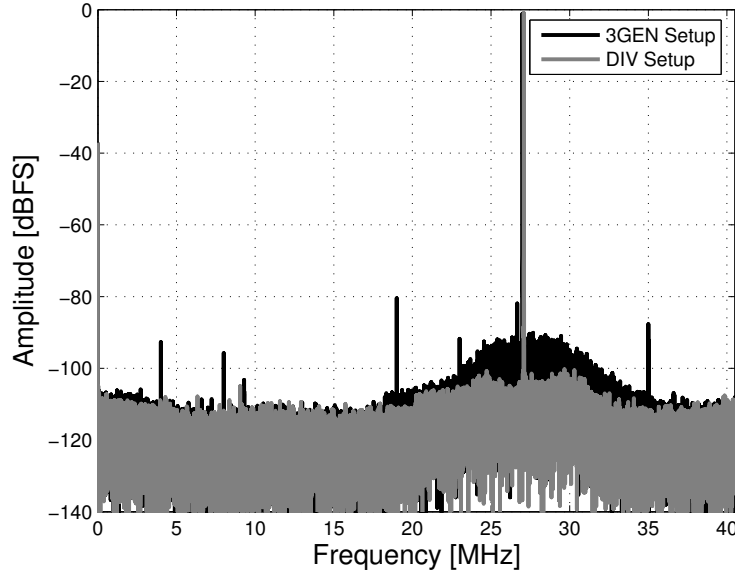frequencies, especially at the mixer output.

Figure 6.2: Spectrum of ADC raw data for different signal generation schemes with intermediate frequency of $f_{\mathrm{IF}} = 54\,\mathrm{MHz}$ and sampling frequency of $f_s = 81\,\mathrm{MHz}$.

The difference in the signal quality can be observed in Fig. 6.2. It shows the spectrum of the raw data of the ADC (sampled IF signal) measured with both the 3GEN and the DIV set-up. In the spectrum, a higher noise floor of the 3GEN set-up can be observed. The plateau around the carrier originates from the bandpass filter (54 MHz, 10% bandwidth) in front of the ADC. The main contribution of the noise floor is that of the LO signal via the mixer. The noise contribution due to the CLK signal would increase the overall noise floor of the spectrum, because it acts behind the bandpass filter in the sampling process of the ADC. The measured rms amplitude and phase jitter for a detection bandwidth of 1 MHz of the 3GEN set-up are

$$\left(\frac{\Delta A}{A}\right)_{rms} = 0.89 \cdot 10^{-4} \qquad \Delta\varphi_{rms} = 2.87 \cdot 10^{-4}\,\mathrm{rad}$$

and for the DIV set-up

$$\left(\frac{\Delta A}{A}\right)_{rms} = 0.33 \cdot 10^{-4} \qquad \Delta\varphi_{rms} = 0.67 \cdot 10^{-4}\,\mathrm{rad}.$$

The rms amplitude jitter of the DIV set-up is 3 times lower than that of the 3GEN set-up, while the rms phase jitter is 4 times lower.

6.1.2   Measurement Set-up

The measurement set-up for characterizing the detector is shown in Fig. 6.3. The signal generation set-up (DIV set-up) is connected to the detector (DUT). For intermodulation tests, a second signal source (RF 2) with a frequency shift of 1 MHz was added. The amplifiers in front of the combiner were used for decoupling the signal sources.

For drift characterization, the detector and the DIV set-up were installed separately in an oven with a temperature stabilization of about 0.1°C. To determine the temperature coefficient of the detector, the response of a temperature step of approximately 10°C on oven No. 2 was measured. A rough temperature measurement was done to estimate the influence of each converter stage on the temperature coefficient of the system.

A logic analyzer was connected to the detector (ADC) to acquire and analyze the digital data. For temperature recording, a conventional data logger with temperature sensors was applied.
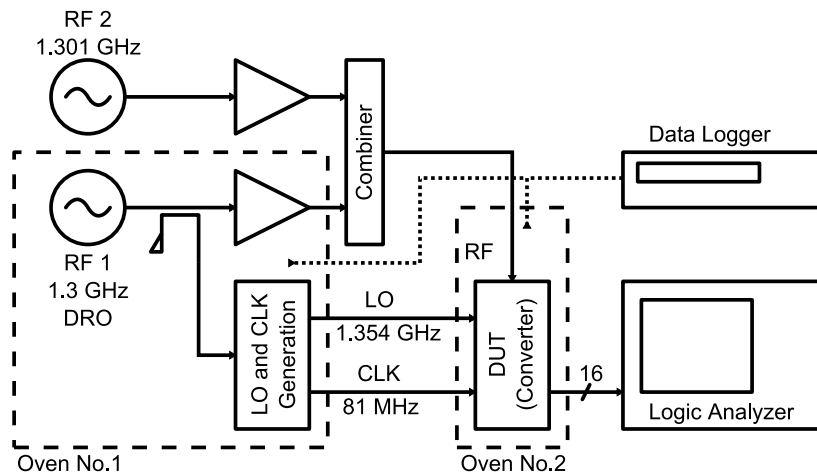
Figure 6.3: Measurement set-up for detector characterization

Due to the chosen intermediate frequency of 54 MHz and the sampling frequency of 81 MHz, the minimal number of samples for IQ detection is 3. This leads to a detection bandwidth of 27 MHz. With 9 samples, the detection bandwidth is decreased to 9 MHz. For a detection bandwidth of 1 MHz, 81 samples have to be used for IQ detection. In the subsequently described tests, a detection bandwidth of either 1 MHz or 9 MHz were used, respectively.

6.1.3   Results of the Laboratory Test

Without the high power attenuators and a reduced attenuation level of the digital input attenuator down to 1 dB, an input power level of 17 dBm is necessary to get

full scale operation of the ADC. For the same attenuator settings, the calculated value yields 13 dBm. This difference results from higher insertion loss of the mixer and bandpass filter and from a reduced step-up ratio of the transformer because of impedance mismatch at the ADC input. The system gain is

$$G_{\mathrm{sys}} = -6 \, \mathrm{dB}.$$

The measured values of the rms amplitude and phase jitter at -1 dBFS operation of the ADC are

$$\left(\frac{\Delta A}{A} \right)_{rms} = 0.92 \cdot 10^{-4} \pm 5.2 \cdot 10^{-6} \qquad \Delta\varphi_{rms} = 1.7 \cdot 10^{-4} \pm 1.4 \cdot 10^{-5} \, \mathrm{rad}$$

for a detection bandwidth of 9 MHz, and

$$\left(\frac{\Delta A}{A} \right)_{rms} = 0.37 \cdot 10^{-4} \pm 4.7 \cdot 10^{-6} \qquad \Delta\varphi_{rms} = 0.9 \cdot 10^{-4} \pm 2.3 \cdot 10^{-5} \, \mathrm{rad}$$

for a detection bandwidth of 1 MHz. The phase jitter corresponds to an integrated timing jitter at 1.3 GHz of 20.8 fs and 11.0 fs, respectively. The measurement time was 400 μs, which leads to a lower corner frequency of 2.5 kHz. The calculations in section 5.1.4 yield a jitter of $0.95 \cdot 10^{-4}$ for 9 MHz and $0.32 \cdot 10^{-4}$ for 1 MHz. The measured amplitude jitter is in the same range, while the measured phase jitter is approximately 3 times higher. This is caused by a higher white noise floor of the phase, by the 1/f noise of the mixer, and by the internal LO buffer of the mixer, respectively [40].

The nonlinearity performance of the detector is measured by a two-tone test with a difference frequency of $\Delta f = 1$ MHz. This method offers a higher accuracy than a linear power sweep with a network analyzer. The measured intermodulation distance (Fig. 6.4) of the lower sideband is 45.6 dBc and for the upper sideband 43.6 dBc, while the power levels for the two carriers are $P_{\omega_1} = -6.6$ dBFS and $P_{\omega_2} = -5.6$ dBFS. Both values lead to a system IP3 of

$$P_{\mathrm{OIP3}} = 16.2 \, \mathrm{dBFS} = 27.3 \, \mathrm{dBm}.$$

or

$$P_{\mathrm{IIP3}} = 22.2 \, \mathrm{dBFS} = 33.3 \, \mathrm{dBm}.$$

The measured P_{OIP3} is 6 dB lower than the calculated one. A possible reason for the linearity degradation could be the saturation of the ferrite in the step-up transformer. The main contribution to the system OIP3 is caused by the mixer. The amplitude compression error for full scale operation of the ADC (11 dBm $\hat{=}$ -1 dBFS) reads
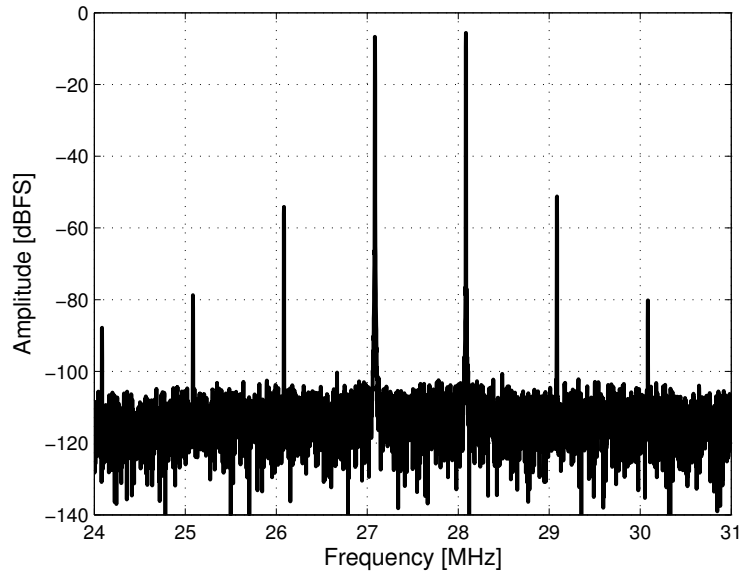
$$(\Delta A/A)_{\mathrm{NL}} = 2.34 \, \%.$$

Figure 6.4: Measured intermodulation spectrum with $\Delta f = 1\,\text{MHz}$. Intermodulation distance is $45.6\,\text{dBc}$ for the lower sideband and $43.6\,\text{dBc}$ for the upper sideband.
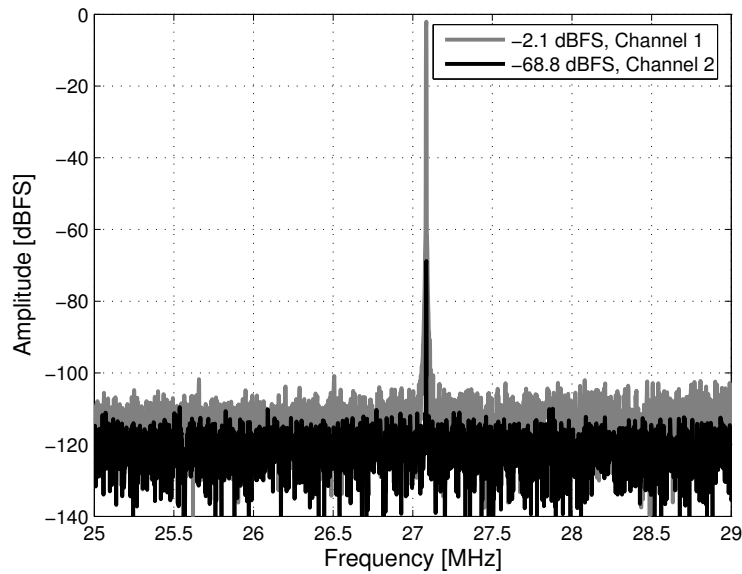

Figure 6.5: Measured crosstalk of $66.7\,\text{dB}$ between two adjacent channels; Channel 1: with input power; Channel 2: matched with $50\,\Omega$

The requirement for the amplitude compression error to be smaller than 1% requires an OIP3 of 31 dBm for full scale operation.

The channel-to-channel crosstalk is determined to be -66.7 dB (Fig. 6.5) by measuring two channels in parallel, one with input power (Channel 1), while the other one is terminated with $50\,\Omega$ at its input (Channel 2). Its main contribution is caused by the low RF-to-LO isolation of the mixer and by the low isolation of the power splitter outputs in the LO distribution network.
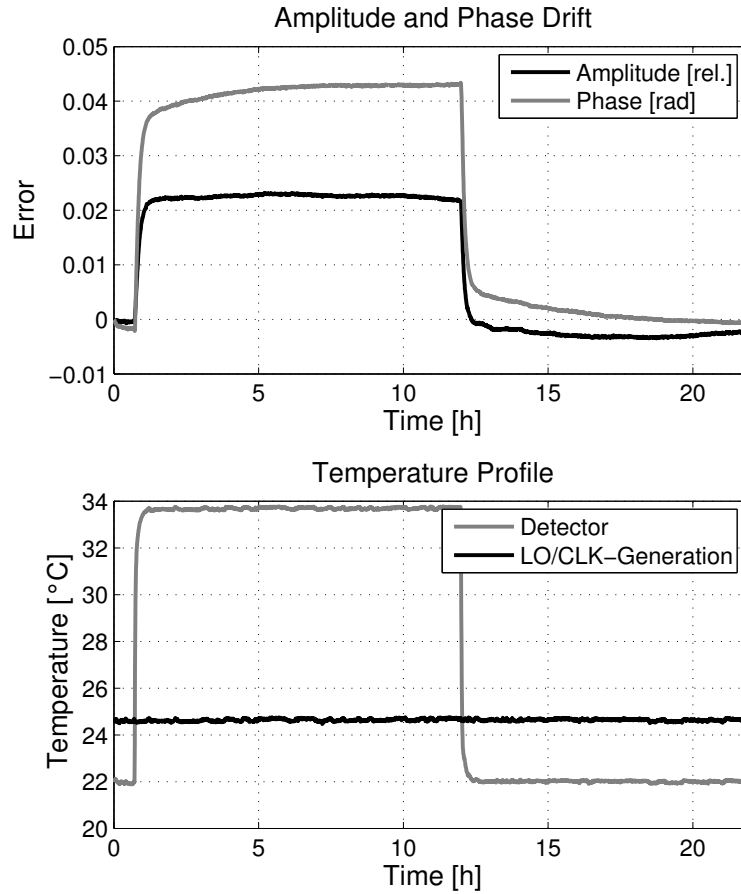
Figure 6.6: Results of the drift measurement with a temperature step of $12°C$.

The results of the drift characterization are shown in Fig.6.6. The determined temperature coefficients of the detector for amplitude and phase are

$$\theta_A = 2 \cdot 10^{-3}/°C \qquad \theta_\phi = 0.2°/°C.$$

The main contribution to θ_A is caused by the digital input attenuator, while the contribution to θ_ϕ is caused by the mixer and the bandpass filter. The temperature sensitivity of the ADC is insignificant for both amplitude and phase.

6.1.4   Conclusion

For a measurement bandwidth of $1\,\mathrm{MHz}$, a rms amplitude jitter of $0.37 \cdot 10^{-4}$ and a rms phase jitter of $0.9 \cdot 10^{-4}\,\mathrm{rad}$ are achieved, which fulfill the requirement to be below 10^{-4}. Jitter and drift of the LO directly limit the detector performance, whereas the ADC clock jitter is less significant. A stable LO signal generation is needed, also for frequencies below $100\,\mathrm{Hz}$ and for phase drifts caused by temperature changes. Presently, the ADC limits the high frequency noise performance of the field detection.

The amplitude compression error of the detector nonlinearity of $(\Delta A/A)_{\mathrm{NL}} = 2.34\,\%$ is beyond the required value of $1\,\%$. An improvement could result from an additional low noise and high linear buffer amplifier in front of the ADC, in order to reduce the power level of the operating point of the mixer. It is also possible to implement linearization techniques.

The temperature coefficients for amplitude and phase, $\theta_{\mathrm{A}} = 2 \cdot 10^{-3}/^{\circ}C$ and $\theta_{\phi} = 0.2^{\circ}/^{\circ}C$, require a temperature stabilized environment and a drift compensation.

Besides using a passive low-noise front-end, the improved detection resolution is caused by the detection scheme and the reduced detection bandwidth of $1\,\mathrm{MHz}$.

6.2   Tests at FLASH

For the performance tests of the detector at FLASH two steps were performed. First of all, the noise behavior of the detector installed in the accelerator environment was investigated and compared with the results of the laboratory tests. The analysis was done both in the frequency and time domain. It was observed that disturbances from other systems in the environment disturb the quality of the field detection. Afterwards, the behavior of the detector in the control loop was investigated. To begin with, a single cavity was used as the plant in the control loop, and the maximal reachable loop gain and field stability were determined. In the next step, the same tests were performed with the vectorsum of 8 cavities, which required a vectorsum calibration. At last, an energy stability measurement was performed, in order to evaluate the quality of the field control. The purpose of these tests was to get a field stability of 10^{-4} for a detection bandwidth of $1\,\mathrm{MHz}$ in amplitude and phase with the new IF sampling scheme and the chosen hardware set-up.

For the performance tests at FLASH, the new detector and the digital readout board ACB2.0 were installed at the accelerator. The cavity signals were connected to the detector inputs. The LO signal for the mixers and the CLK signal for the ADCs were provided by a separate set-up, which has also been used in the laboratory tests. The $1.3\,\mathrm{GHz}$ reference was taken from the MO, in order to guarantee synchronized LO and CLK signals to the RF of the cavity field. To

prevent an overdrive of the digital input attenuators of the detector, 10 dB high power attenuators were installed in order to reduce the input power level down to the required 20 dBm. The output power of the cavity probe is up to 30 dBm for a maximum gradient of 22 MV/m.

6.2.1 Detector Performance

In the first step, the noise performance of the detector was evaluated by measuring its resolution without an input signal. The equivalent input noise of the eight detector channels was measured. It is summarized in Fig. 6.7 for three different cases. In the first one, the analog front-end was switched off and the RF and LO inputs were matched with $50\,\Omega$ in order to get the resolution of the ADC. In the second case, the power supply for the analog front-end was switched on, while the LO and RF inputs were still matched. At last, the LO signal was connected to the mixers.
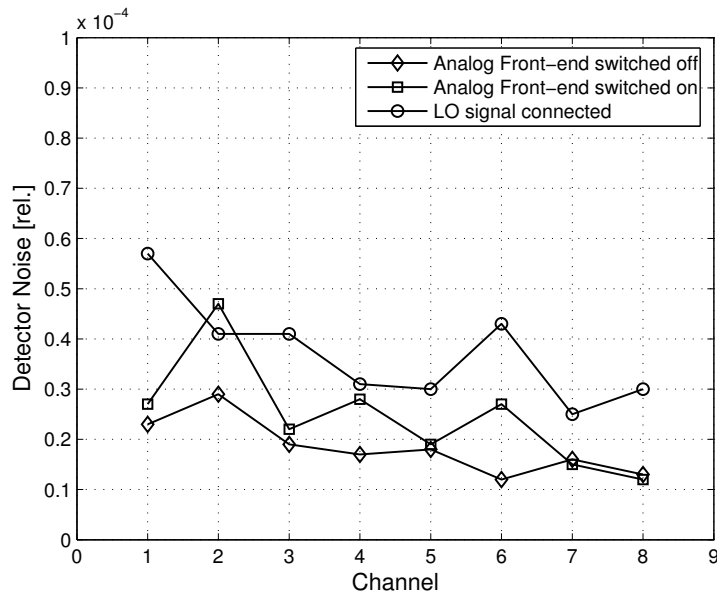
Figure 6.7: Measured detector noise for a detection bandwidth of 1 MHz and three different input constellations.

With the analog front-end switched off, the resolution of the ADC for a detection bandwidth of 1 MHz was below $0.3 \cdot 10^{-4}$ for all eight channels. The spectra of channel 2 and 8 are depicted in Fig. 6.8 as a representative selection of all channels. Some spurious lines below -100 dBFS are visible, while the noise floor is at -120 dBFS for both channels. With a FFT length of $N = 131072$ points, a sampling frequency of $f_s = 81$ MHz, and a full scale input power of $P_{\text{FS,ADC}} =$

11 dBm, the noise floor can be determined to be

$$S_{\mathrm{ADC}} = -147.9\,\mathrm{dBFS/Hz} \widehat{=} -136.9\,\mathrm{dBm/Hz}. \tag{6.1}$$

With the thermal noise floor of $-174\,\mathrm{dBm/Hz}$, the equivalent noise figure can be determined as $\mathrm{NF}_{\mathrm{ADC}} = 37\,\mathrm{dB}$.
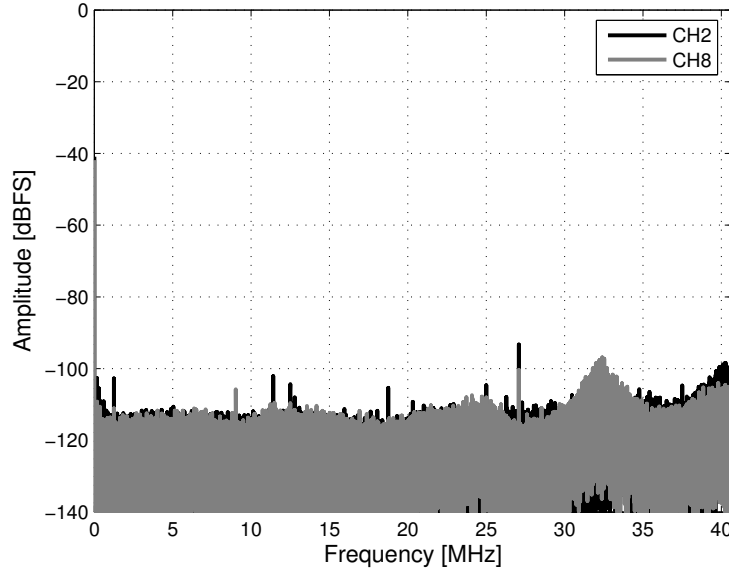

Figure 6.8: Spectra of raw data of channels 2 and 8; RF and LO inputs are matched with $50\,\Omega$ and the analog front-end is switched off.

When the analog front-end is switched on, the noise in channels 2, 4 and 6 increases (Fig. 6.7). In the spectrum (Fig. 6.9), the noise floor of channel 2 increases by 10 dB and by 20 dB between 25 MHz and 35 MHz. The spectral line at 4 MHz is of minor relevance, because it is out of the frequency band of interest, which is around 27 MHz. The origin of the increased noise floor and the spectral line is still unknown and has to be investigated. In channel 8 the noise floor is still at -120 dBFS. With the connected LO, the noise of all detector channels increases (Fig. 6.7), except for channel 2. In the spectra of channels 2 and 8 (Fig. 6.10), an additional spectral line at 27 MHz with an amplitude of -65 dBFS is visible, while the noise floor in channel 2 decreases down to -120 dBFS again. This line at 27 MHz could be the 1.3 GHz of the MO, fed through the LO generation set-up and coupled to the input of the mixer. In time domain (Fig. 6.11), the crosstalk of the RF gun pulse to the detector channel is visible in channel 8. This signal crosstalk is visible with the old detection system as well, while the path of it is still unknown. The 27 MHz component in the spectrum of channel 8 could be the crosstalk of the RF gun pulse, too. Crosstalk is possible via the power supply, the MO, or unshielded cables along the whole environment.
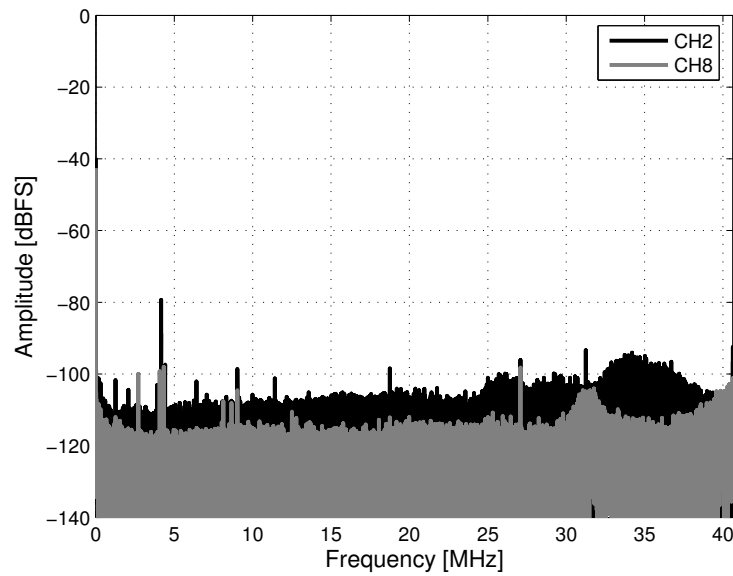
Figure 6.9: Spectra of raw data of channels 2 and 8; RF and LO inputs are matched with $50\,\Omega$ and the analog front-end is switched on.
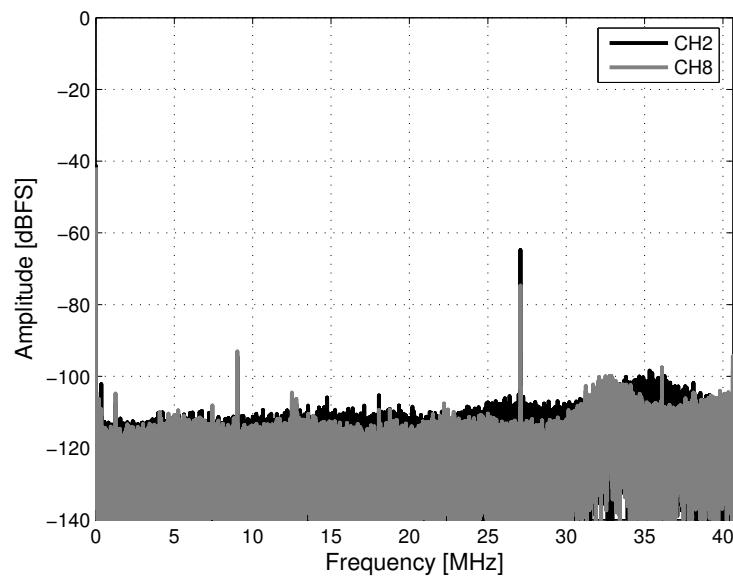

Figure 6.10: Spectra of raw data of channels 2 and 8; the RF inputs are matched with $50\,\Omega$ and the LO signal is connected.
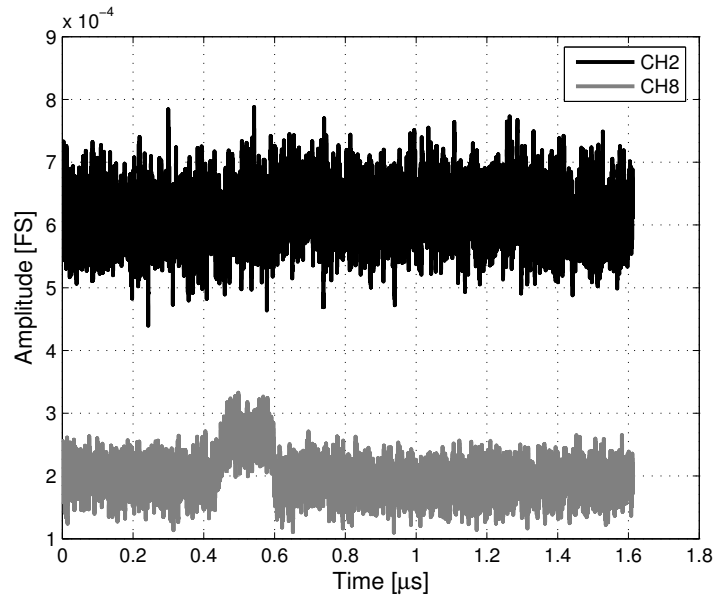
Figure 6.11: Detected amplitude of channels 2 and 8 with detection bandwidth of 1 MHz; crosstalk of RF gun pulse is visible in channel 8;

However, with all these disturbances and the RF gun crosstalk, the detector resolution with a detection bandwidth of 1 MHz is still below the required 10^{-4}.

To measure the detector resolution with an input signal, the MO is used as RF signal and connected to each detector channel. Because LO and CLK signals are generated by the MO, all signals are synchronized and derived from the same source. The measurement conditions are comparable to the laboratory tests, except for disturbances from the accelerator environment. In Fig. 6.12, the spectra of channels 2 and 8 are shown once more. The downconverted and sampled 1.3 GHz signal is visible as the spectral line at 27 MHz. Four additional spectral lines are observable close to the carrier. They are located in the band of interest of 1 MHz around the carrier (Fig. 6.13). For all channels these lines are below -80 dBFS. For each channel, the amplitude and phase stability for detection bandwidths of 9 MHz and 1 MHz are measured and presented in Fig. 6.14. The reduction of the detection bandwidth from 9 MHz to 1 MHz yields twice better jitter values. Only the values of the amplitude jitter of the last five channels for a detection bandwidth of 1 MHz reach the required value of 10^{-4}.

The final measurement of the detector performance test was done with the cavity probe signals. All probe signals were connected to the detector and the attenuation level of the digital input attenuators were adjusted to get a signal level close to the ADC full scale range for maximum gradient. The amplitude and phase of cavities 2 and 8 are shown in Fig. 6.15 with a detection bandwidth of 1 MHz. During the first 500 μs, the cavity field is built up, followed by 300 μs
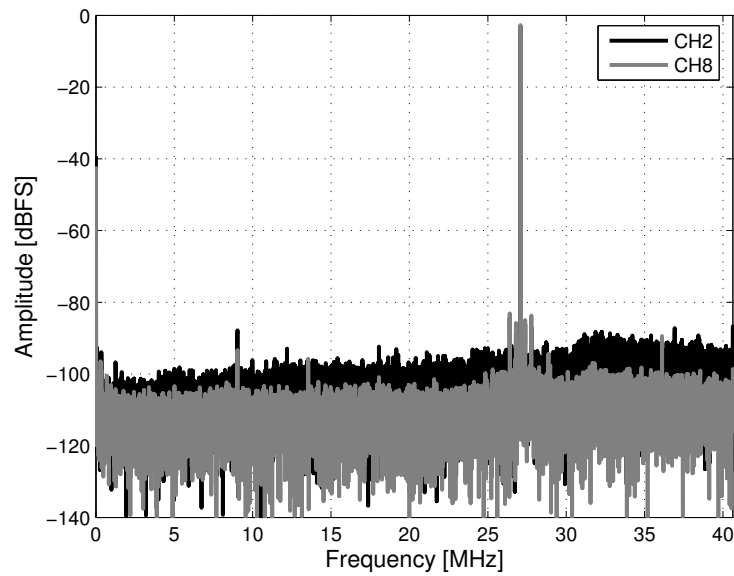
Figure 6.12: Spectra of channels 2 and 8; the 1.3 GHz of the MO is used as RF input signal

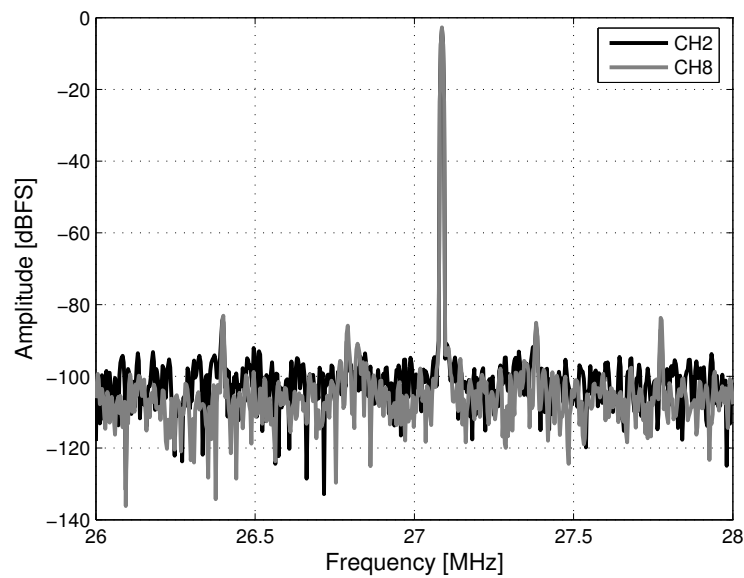

Figure 6.13: Spectra of channels 2 and 8 zoomed to the carrier; two sidebands at 300 kHz and 700 kHz are visible. They are below −80 dBFS.
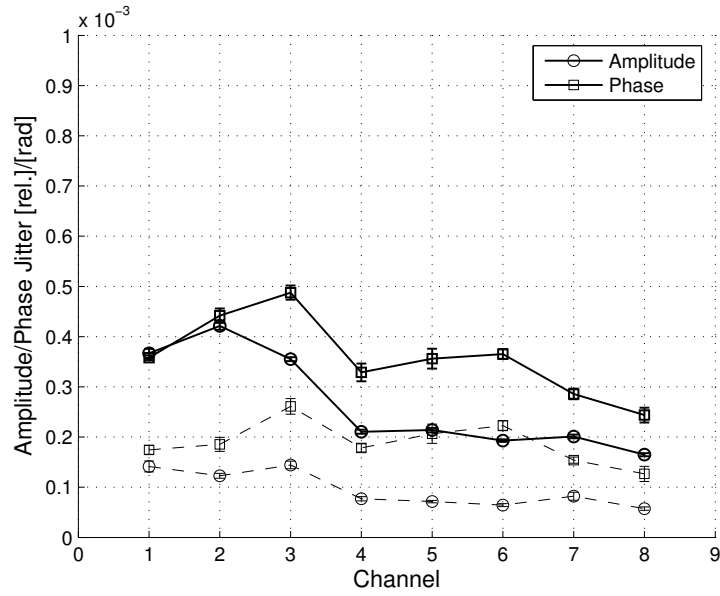
Figure 6.14: Rms amplitude and phase jitter of the detected 1.3 GHz signal of the MO for a detection bandwidth of 9 MHz (solid) and of 1 MHz (dashed).
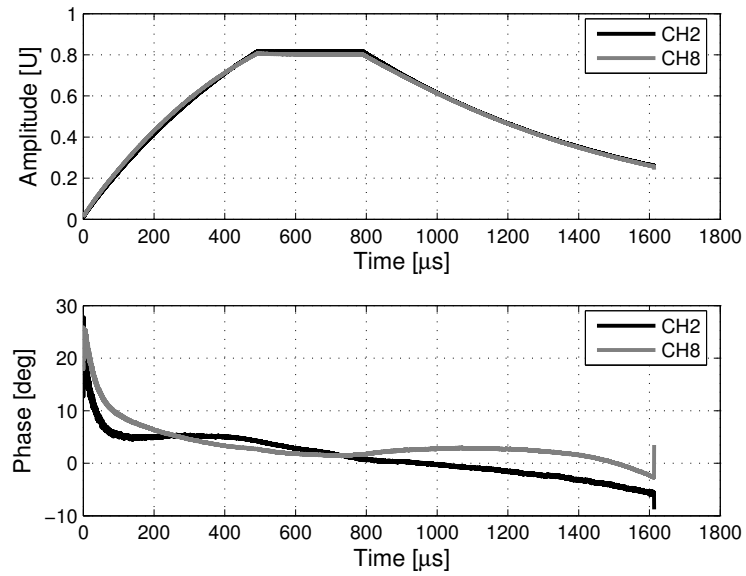

Figure 6.15: Amplitude and phase of the field vector in cavities 2 and 8 for a detection bandwidth of 1 MHz.

of constant gradient and phase (flat-top phase), and then the forward power is switched off and the cavity field decays.
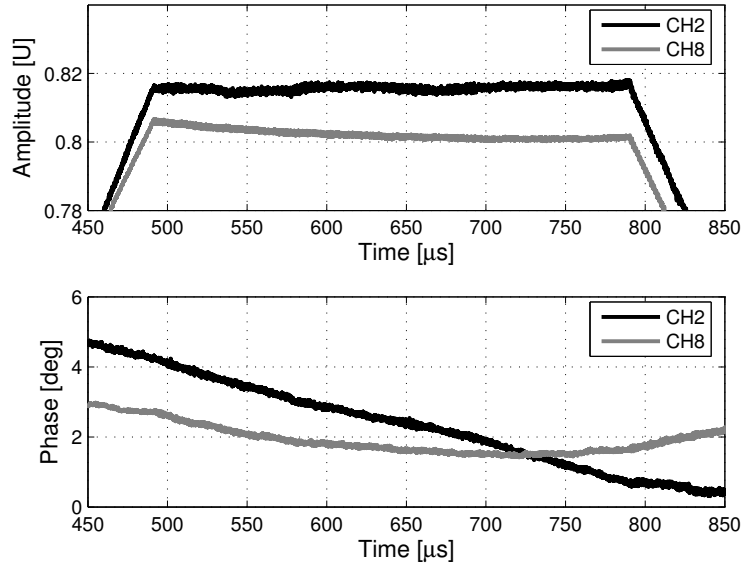

Figure 6.16: Zoomed flat-top phase of amplitude and phase (Fig. 6.15, detection bandwidth of 1 MHz)

In Fig. 6.17, the spectra of the flat-top phase of both channels are depicted. Close to the carrier, the $8/9\pi$-mode is visible and the noise floor increases. For each channel, the amplitude and phase stability of the cavity probe signal during the flat-top phase has been measured for different detection bandwidths. They are shown in Fig. 6.18. With reduced detection bandwidth, less high frequency noise disturbs the resolution of the field detection. The $8/9\pi$-mode close to the carrier is still present at the amplitude and phase of the cavity probe signal (Fig. 6.19). This also holds for the reduced detection bandwidth of 1 MHz.

6.2.2 Single Cavity Results

For the first tests of the detector within the control loop, only one cavity field (cavity 6) was controlled by the control loop. The other cavities were disregarded by setting the calibration matrices to zero. They were not considered by the controller.

The detected measures were the high frequency rms fluctuation of the amplitude and phase during the flat-top phase, the pulse-to-pulse stability of the field, and the field flatness. All these measures were recorded as function of loop gain. The slope of the amplitude and phase during the flat-top phase were calculated by a polynomial fit of 3rd order (Fig. 6.20) and subtracted from the field. The
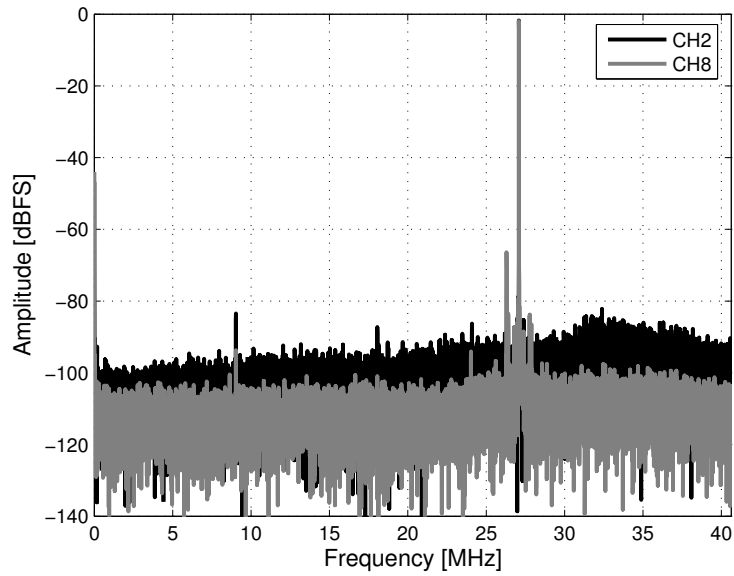
Figure 6.17: Spectra of cavities 2 and 8; cavity probe signal is connected to the detector. The spectral line close to the carrier at 27 MHz is the $8/9\pi$-mode, which is 800 kHz below the carrier.
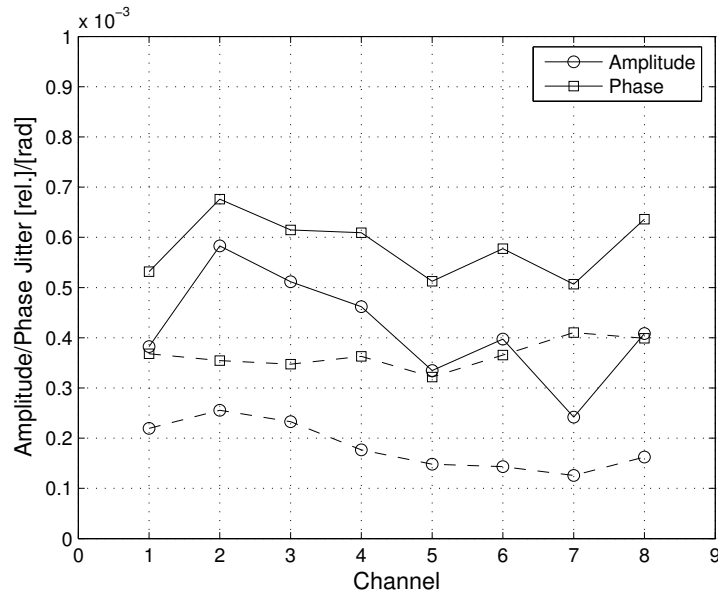

Figure 6.18: Rms amplitude and phase stability of the detected cavity probe signal during the flat-top phase for a detection bandwidth of 9 MHz (solid) and of 1 MHz (dashed)
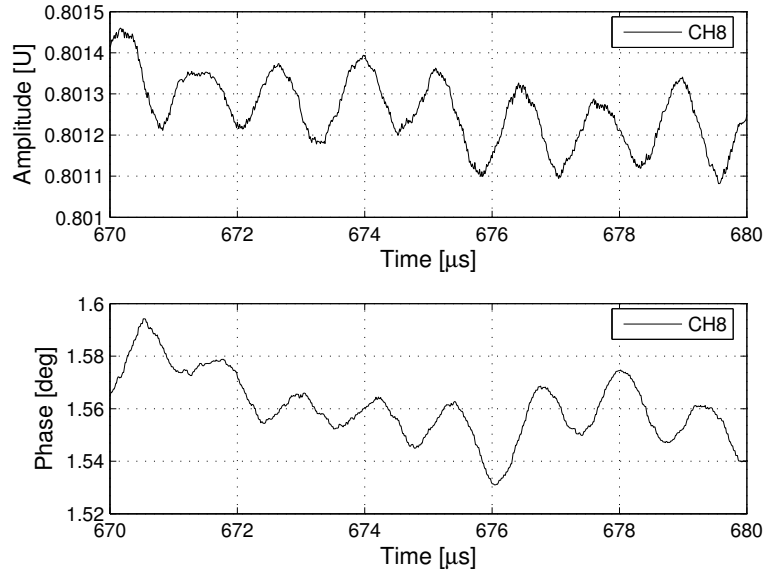
Figure 6.19: The oscillation of the $8/9\pi$-mode is still present on the amplitude and phase of the cavity field for a detection bandwidth of $1\,\text{MHz}$.

standard deviation of this difference yielded the high frequency rms fluctuations. The amplitude noise was normalized to the mean value of the flat-top phase amplitude. The field flatness was calculated by the difference between the maximum and the minimum of the amplitude and phase during the flat-top phase, while the pulse-to-pulse fluctuations were determined by the variance of the flat-top mean values measured from pulse-to-pulse. The rms fluctuations are mainly high frequency noise from the actuator, MO, and detector. The main contribution is from the MO and detector, because the actuator noise is filtered by the cavity. The field flatness is affected by the Lorentz force detuning, which leads to a time and gradient dependent detuning during the pulse. The pulse-to-pulse fluctuations are caused by microphonics.

For the single cavity, a maximum loop gain of 40 was observed. It was limited due to instabilities in the control loop. The spectrum of the amplitude and phase (Fig. 6.21) at the maximum gain value shows the excited and increased $8/9\pi$-mode. The updated rate of the controller is set to $1\,\text{MHz}$. The $8/9\pi$-mode is aliased from $820\,\text{kHz}$ down to $180\,\text{kHz}$. As depicted in Fig. 6.22, the rms fluctuations are affected by the excited oscillation of the $8/9\pi$-mode. They increase for higher loop gain. For a moderate gain value of up to 20, the rms field fluctuations are

$$\left(\frac{\Delta A}{A}\right)_{\text{rms}} = 2 \cdot 10^{-4} \qquad \Delta\varphi_{\text{rms}} = 3 \cdot 10^{-4}\,\text{rad}.$$

The amplitude of the $8/9\pi$-mode in the spectrum of -63 dBFS leads to an rms
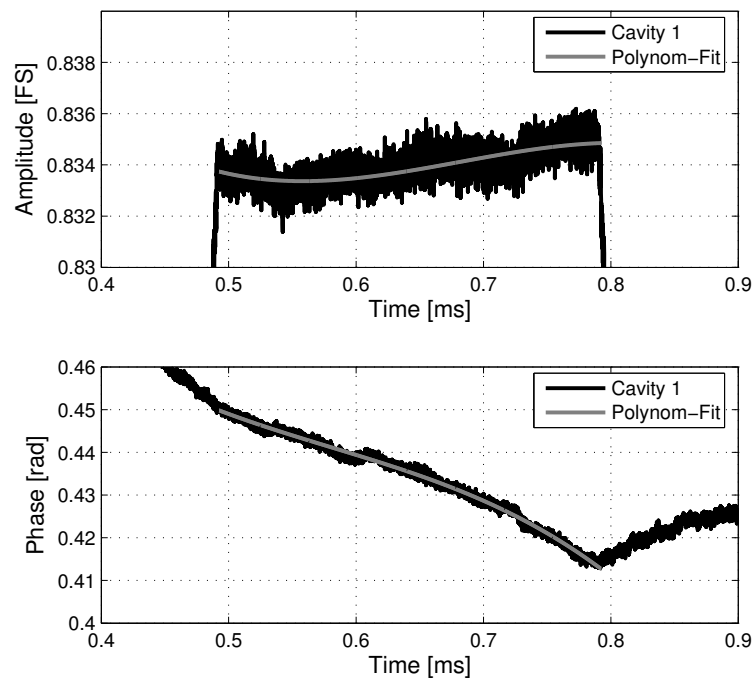
Figure 6.20: Amplitude and phase of cavity no. 1 with polynomial fit in order to determine high frequency rms noise and field flatness.
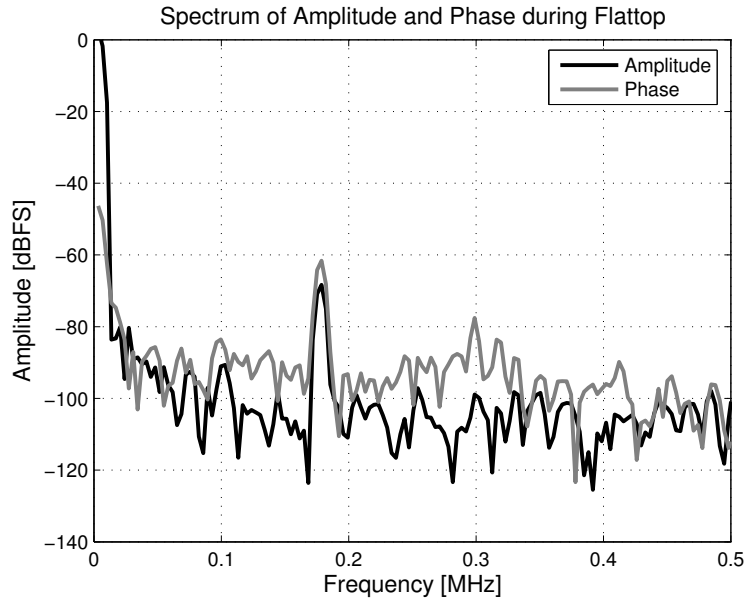
Figure 6.21: Spectrum of the vectorsum during the flat-top phase for maximal gain value of 40; $8/9\pi$-mode is visible and reason for an increased rms value. The $8/9\pi$-mode is aliased from $820\,\mathrm{kHz}$ down to $180\,\mathrm{kHz}$.
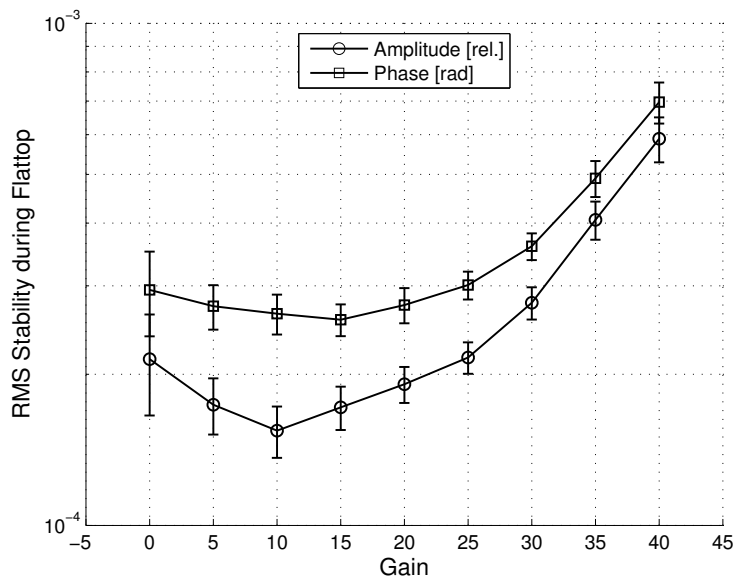

Figure 6.22: Measured rms field stability of cavity 6 as function of loop gain at a detection bandwidth of $1\,\mathrm{MHz}$.

fluctuation of approximately $7 \cdot 10^{-4}$ at a loop gain of 40 which is visible in Fig. 6.22. For the field flatness (Fig. 6.23), a value of $1.3 \cdot 10^{-3}$ for the amplitude and
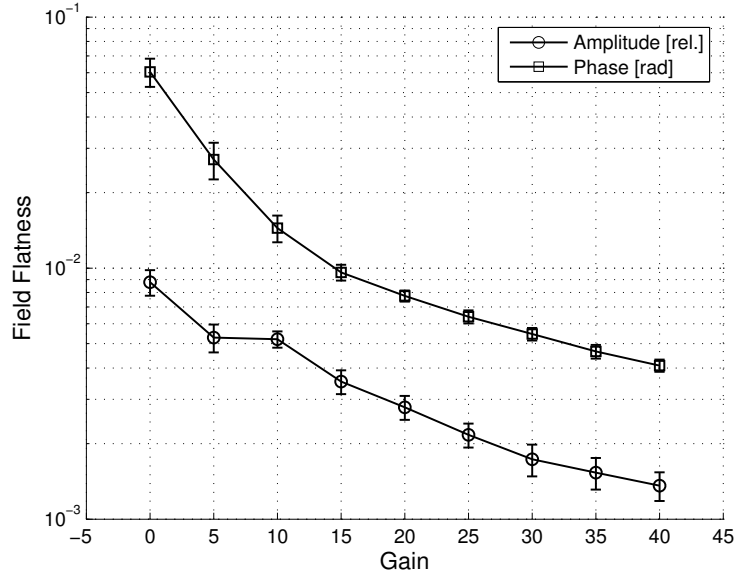

Figure 6.23: Measured field flatness of cavity 6 as function of loop gain

$4 \cdot 10^{-3}$ rad for the phase were reached, while for a loop gain of 20 the corresponding values are

$$\left(\frac{\Delta A}{A}\right)_{\mathrm{ff}} = 2.8 \cdot 10^{-3} \qquad \Delta\varphi_{\mathrm{ff}} = 8 \cdot 10^{-3} \, \mathrm{rad}.$$

The fluctuation of the field flatness is caused by the Lorentz-force detuning, which is a repetitive error. It can be reduced by applying an adaptive feedforward [9] [10].

As mentioned before, the pulse-to-pulse fluctuations are caused by microphonics. These fluctuations can only be suppressed by feedback. They were suppressed down to $0.9 \cdot 10^{-4}$ for the amplitude and $3.3 \cdot 10^{-4}$ rad for the phase (Fig. 6.24). For a stable loop gain of 20, the corresponding values are

$$\left(\frac{\Delta A}{A}\right)_{\mathrm{p2p}} = 2.4 \cdot 10^{-4} \qquad \Delta\varphi_{\mathrm{p2p}} = 7.3 \cdot 10^{-4} \, \mathrm{rad}.$$

As described in section 3.3, the measured rms field stability is only an upper boundary of the real rms stability of the cavity field. Due to the small bandwidth of the cavity, the noise of the detector limits the resolution.

Slow changes in the field (pulse-to-pulse stability and field flatness), induced by Lorentz force detuning and microphonics, are measurable and can be suppressed by the feedback loop.
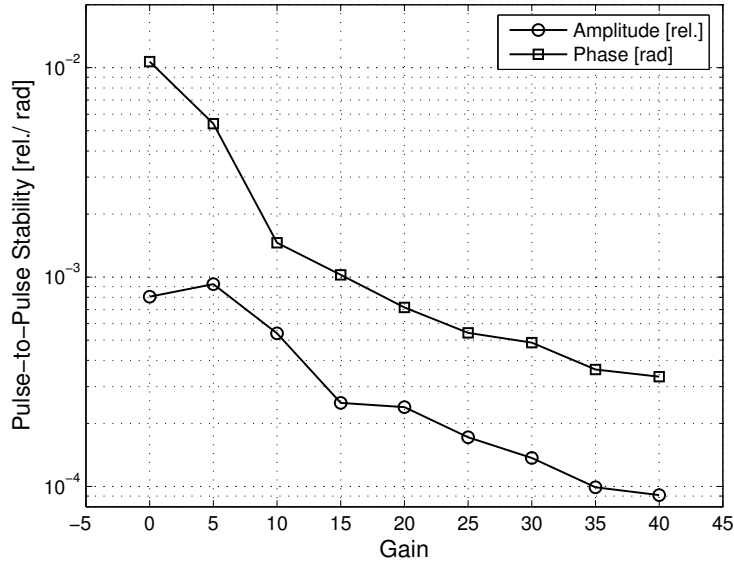
Figure 6.24: Measured pulse-to-pulse stability of cavity 6 as function of loop gain

6.2.3 Vectorsum Control

Finally, the vectorsum of eight cavities was detected and controlled. Before controlling a vectorsum of eight cavities, it has, however, to be calibrated.

Vectorsum Calibration

As described in section 3.6, the measured vectorsum does not correspond to the real vectorsum. Due to different cable lengths and variations of the detector gain, each amplitude and phase of the measured field vectors are different. Due to time dependent detuning induced by microphonics, these measurement errors lead to time dependent errors which limit the quality of field control. Additionally, for a certain constellation of the phases of the measured field vectors, the control loop already becomes unstable at small loop gain values. It is sufficient, if the ratio of the measured field vectors are equal to the ratio of the real field vectors. There is no need of absolute accuracy.

Two methods of vectorsum calibration will be presented and used. The first one is a coarse method, which is used to guarantee equal measured phases of each field vector with an accuracy of $\Delta\varphi_{cal} = \pm 10°$. It is used to get stable feedback loop operation. The amplitudes of the field vectors are assumed to be equal. In the ACC1-module, which was used for the detector tests, four cavities are operating at half of the gradient compared to the other four. This leads to an amplitude calibration error of $(\Delta A/A)_{cal} = 50\%$. Based on the calculations in

[9], the measurement accuracy of the vectorsum reads

$$\left(\frac{\Delta A}{A}\right)_{\text{VS}} = 1 \cdot 10^{-3} \qquad \Delta\varphi_{\text{VS}} = 1 \cdot 10^{-2} \, \text{rad}$$

for average microphonics of 10 Hz present at ACC1. The second method is described in detail in [8] and [9]. For this method, an electron beam with high beam loading (up to 4 nC and 30 bunches) is needed. The beam induces a transient of the field vector of each cavity in amplitude and phase. It is assumed, that the absolute transient of each cavity is equal. The calibration is based on measuring this transient in amplitude and phase and then calculating the ratio of the transient and the field vector of each cavity. The complex calibration factors are derived by these ratios. This beam based method leads to a calibration error of 0.5° in phase and 1% in amplitude. The resulting measurement accuracy is the required

$$\left(\frac{\Delta A}{A}\right)_{\text{VS}} = 1 \cdot 10^{-4} \qquad \Delta\varphi_{\text{VS}} = 1 \cdot 10^{-4} \, \text{rad}.$$

The determined calibration coefficients for the new detector are presented in Tab. 6.1. The calibration is based on the ratios of the field vectors against that of cavity 1, which is used as reference.

	CH1	CH2	CH3	CH4	CH5	CH6	CH7	CH8
A_{cal}	1	0.97	0.93	0.96	1.84	1.7	1.25	2.0
φ_{cal} [deg]	0	-16.3	-5.5	8.4	14.0	-23.7	26.3	0.4

Table 6.1: Calibration coefficients of the vectorsum based on the high beam charge transient method.

Vectorsum Results

The rms fluctuations, the pulse-to-pulse stability, and the field flatness are determined as function of the loop gain. For the vectorsum of eight cavities, a maximal loop gain of 170 was achieved. In the spectra of amplitude and phase (Fig. 6.25), the excited $8/9\pi$-mode is visible, which limits the achievable loop gain. Fig. 6.26 shows the rms field stability of the vectorsum. The amplitude fluctuation is slightly affected by the loop gain and reads

$$\left(\frac{\Delta A}{A}\right)_{\text{rms}} = 1 \cdot 10^{-4}$$

at a loop gain of 90, while the phase fluctuation is fixed to

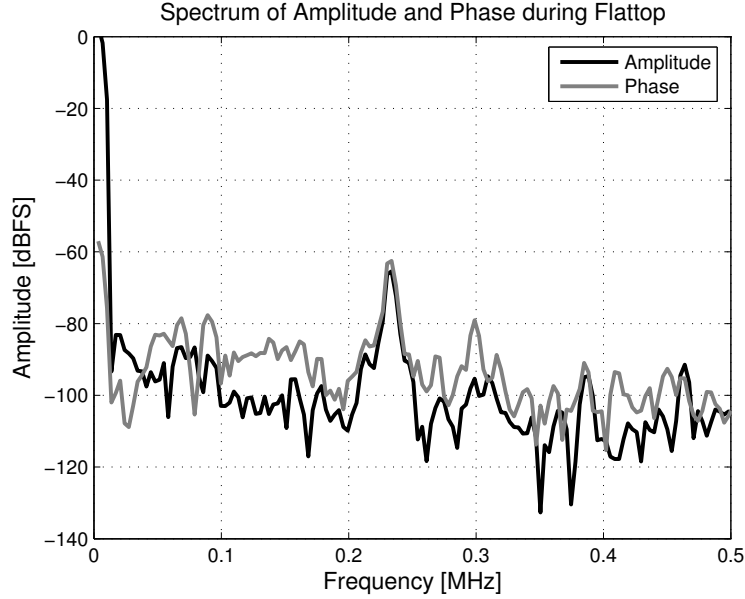$$\Delta\varphi_{\text{rms}} = 2 \cdot 10^{-4} \, \text{rad}.$$

Figure 6.25: Spectrum of flat-top phase for maximal gain value of 170; $8/9\pi$-mode is visible and the reason for increased rms value.

These results are close to the required field stability of 10^{-4} in amplitude and phase. For higher gain values, the fluctuations increase, due to the excited $8/9\pi$-mode. In comparison with the single cavity feedback, a four times higher loop gain can be reached. An explanation could be a destructive interference of the eight $8/9\pi$-modes of the single cavities.

For a loop gain of 90, the field flatness (Fig. 6.27) can be reduced to a value of

$$\left(\frac{\Delta A}{A}\right)_{\mathrm{ff}} = 2.3 \cdot 10^{-4} \qquad \Delta\varphi_{\mathrm{ff}} = 1.3 \cdot 10^{-3}\,\mathrm{rad}.$$

For further improvement of the field flatness, an adaptive feed forward has to be applied. The pulse-to-pulse stability (Fig. 6.28) reaches

$$\left(\frac{\Delta A}{A}\right)_{\mathrm{p2p}} = 1.3 \cdot 10^{-5} \qquad \Delta\varphi_{\mathrm{p2p}} = 7 \cdot 10^{-5}\,\mathrm{rad}.$$

6.2.4 Beam Based Stability Measurement

As shown in the previous section, the measured rms and pulse-to-pulse stability of the controlled vectorsum meets the specification, except for the rms phase. For an improvement of the field flatness, an adaptive feed forward can be applied.

As mentioned before, the measured vectorsum differs from the vectorsum seen by the beam because of the calibration errors. To evaluate the actual quality
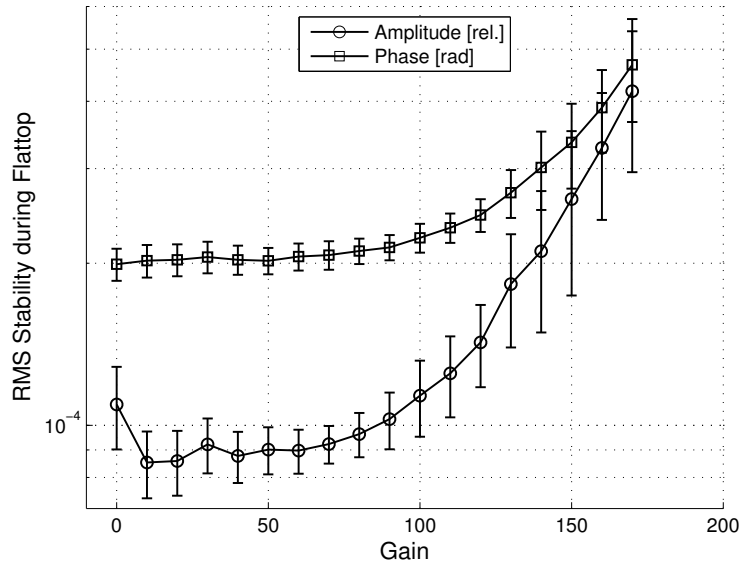
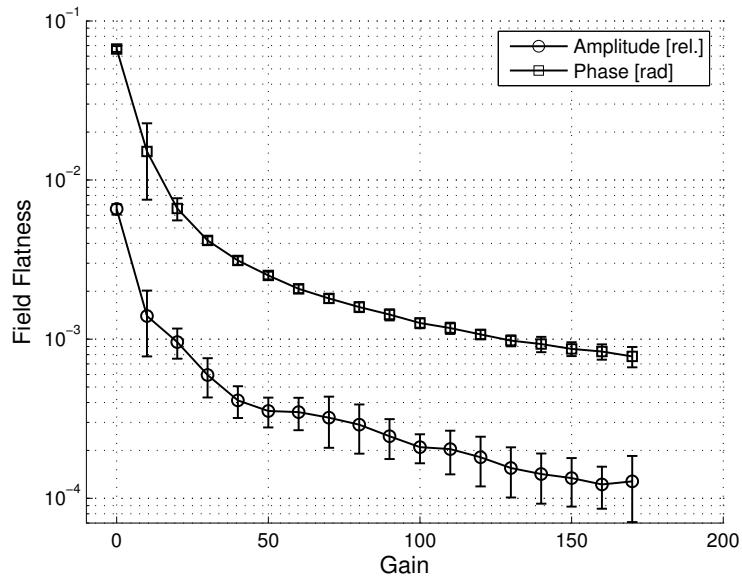Figure 6.26: Measured rms field stability of vectorsum as function of loop gain

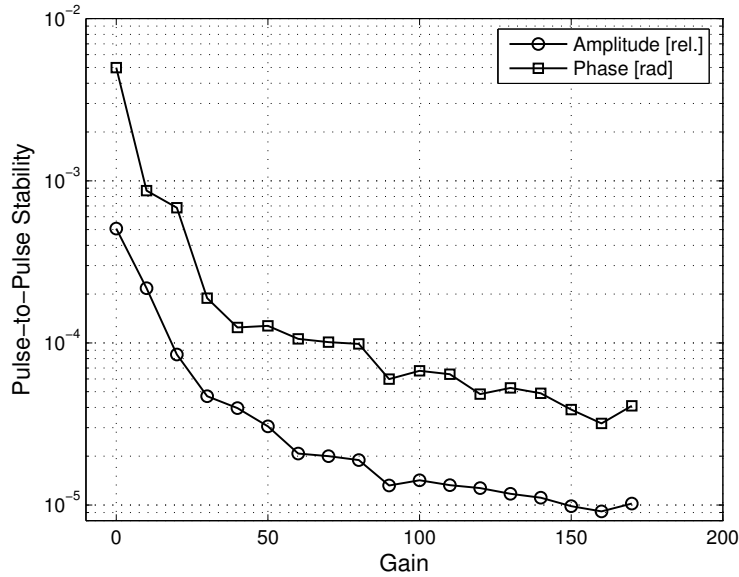Figure 6.27: Measured field flatness of vectorsum as function of loop gain

Figure 6.28: Measured pulse-to-pulse stability of vectorsum as function of loop gain

of the vectorsum control, methods of beam diagnostics have to be used. For this purpose, the stability of the beam energy is measured. Before the first bunch compression section (BC2), the energy spread of the beam is strongly dependent on the stability of the controlled vectorsum in the first accelerating module (ACC1). From Eqn. 3.74, the contribution of the amplitude and phase jitter of the vectorsum to the beam is dependent on the beam phase. For on-crest acceleration, only the amplitude jitter induces an additional energy spread to the beam, while for off-crest acceleration, also the phase jitter contributes to the energy spread. The method of measuring the energy spread is described by [41]. It uses the effect of the energy dependent deflaction of the electron beam by a magnetic field. The bunch is projected on a luminescent screen and recorded by a camera. By the energy dependent deflection of the beam, the position of the beam spot on the screen is dependent on the beam energy. With this method it is only possible to measure the pulse-to-pulse stability of the beam. For the measurement of the bunch-to-bunch stability, the method described in [28] can be used, which was not available during these tests.

The first measurement was done with coarse vectorsum calibration described before (section 6.2.3). For the second measurement, a beam based vectorsum calibration was used. The results of the measured energy stability are plotted in Fig. 6.29. For comparison, a measured energy stability is plotted, where the vectorsum were controlled by the old IQ sampling scheme with 250 kHz IF (Section 4.2.3). The first measurement with the coarse vectorsum calibration shows a gain
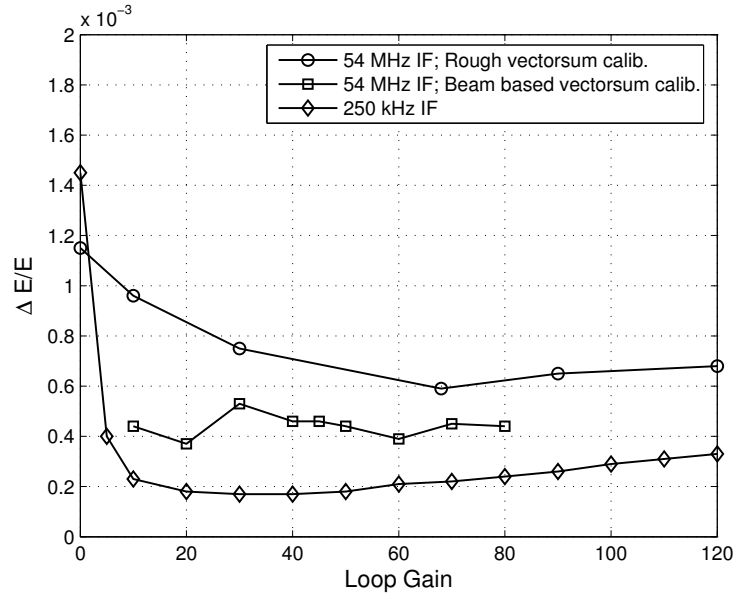
Figure 6.29: Measured energy spread $\Delta E/E$ as function of loop gain.

dependency with an optimum at gain of 70. The value of $(\Delta E/E)_{\mathrm{p2p}} = 5.9 \cdot 10^{-4}$ is 3 times higher than with the old system. The reason is the unsufficient vectorsum calibration. With the coarse calibration method, the calibration errors are $\Delta\varphi_{\mathrm{cal}} = \pm 10°$ and $(\Delta A/A)_{\mathrm{cal}} = 50\%$. This leads to an energy spread of $(\Delta E/E)_{\mathrm{p2p}} = 6 \cdot 10^{-4}$ for a beam phase uncertainty of $\varphi_b = \pm 5°$ and microphonics of $6\,\mathrm{Hz}$.

In the second measurement after the beam based vectorsum calibration, the stability is improved by a factor of 2 to read $(\Delta E/E)_{\mathrm{p2p}} = 3.8 \cdot 10^{-4}$ for a loop gain of 20. But there is no real gain dependency visible and the stability is still worse compared to the stability reached with the old system, except for lower gain values.

Chapter 7

Conclusion and Outlook

In this thesis, a multichannel RF field detector, based on an IF sampling scheme, has been developed and tested in the control loop of the LLRF system at FLASH, in order to control the vectorsum of eight superconductive cavities. The purpose of this investigation has been the development and evaluation of a new RF field detector and detection scheme for the vectorsum control.

Simulations have been performed with a predefined model to analyze the noise transport and behaviour of the control loop. For the model, uniform parameters for the noise description of the subsystems of the LLRF system have been composed. The noise contribution of each component of the LLRF system to the stability of the cavity field and the energy stability of the accelerated electron beam has been investigated. The simulation results have shown that the high frequency noise contribution (above $10\,\mathrm{kHz}$) of the detector is irrelevant for the stability of the cavity field, because of the small bandwidth of the cavity. The high frequency noise of the detector limits the accuracy of the detector output signal, which is used for monitoring the achieved field stability. A gain dependency of the induced beam energy spread was observed, at which the minimum was bounded by the actuator noise contribution (for low gain values) and by the detector noise contribution (for high gain values). For the contribution of the residual phase noise of one LLRF system to the beam energy spread, the bandwidths of all operating systems in the accelerator, which act on the beam, have to be considered. The fastest system with the highest locking bandwidth to the MO is the reference for all other systems.

In the context of the vectorsum control, requirements for the calibration of the field vectors and the linearity of the field detectors had to be derived. The requirements of the vectorsum calibration are treated and discussed in many theses and lead to a maximum allowable calibration error of $1\,\%$ in amplitude and $0.5°$ in phase. Both values have been overtaken here for the maximum tolarable amplitude and phase compression error. In the future, a measurable and reliable verification for the linearity requirements related to the vectorsum calibration should be done.

The first ansatz for the development of a new RF field detector was founded on a new modulation scheme of the IF (IF sampling), which allows to reduce the high frequency noise contribution of the detector by averaging and thereby improves the monitor signals. Because of the usage of a high level passive mixer, the 1/f-noise and the broadband noise were reduced. Initially, the linearity requirements of the detector were subordinated in favor of a better signal-to-noise ratio. The new IF modulation scheme allows to simplify the diagnostics of the IF signal by measurement techniques. With the new modular design and the new packaging, the influence of the before existing separation of the RF front-end and the ADC had to be investigated in terms of crosstalk and electromagnetic interference. Additionally, the platform was planned to be expandable for additional systems (bunch arrival time monitor, beam position monitor, etc.) and to be used as test environment for further prototyping.

The features of the developed RF field detector have been measured in the laboratory and at the accelerator. The detector has been used as multichannel detector for the vectorsum control. The required measurement accuracy of 10^{-4} in amplitude and phase for a measurement bandwidth of $1\,\mathrm{MHz}$ has been achieved for single channel tests in the laboratory. The specifications have not been reached for all eight channels in the multichannel application in the accelerator environment. The stability measurement of the controlled vectorsum showed the predicted gain dependency of the pulse-to-pulse stability, while the rms stability was limited by the high frequency noise of the detector. The measurement of the energy spread showed higher fluctuations of the beam energy than the stabilized vectorsum would suggest. This indicates additional measurement errors. Until now, the available methods of beam diagnostics are limited to measure the pulse-to-pulse stability of the beam energy. Hence it follows, that the low frequency noise of the detector from $1\,\mathrm{Hz}$ to $1\,\mathrm{kHz}$ is critical for the stability of the vectorsum control. Furthermore, calibration errors of the vectorsum lead to additional measurement errors. In further measurements, the influence of the detector linearity on these errors should be investigated.

According to the simulation, the induced energy spread is dependent on the gain. These results were confirmed by measurements with the old modulation scheme (IQ-sampling with switched LO). The gain dependency of the induced energy spread is due to the separation of the contribution of the LLRF system in an actuator and detector part.

The application of the new modulation scheme enables simplified diagnostics of the IF signal, but requires a complex LO generation set-up. This set-up is sensitive to phase drift caused by temperature changes. These phase drifts are responsible for disturbances of the vectorsum control. They cannot be reduced to the required value by temperature stabilization. One needs a drift compensation scheme, which can be additionally used for compensation of phase drifts in cables, e.g. from the cavity pickup to the detector, and for compensation of phase drifts of the detector itself.

Bibliography

[1] Frank Stulle. *A Bunch Compressor for small Emittances and high Peak Currents at the VUV Free-Electron Laser*. Doktorarbeit, Universität Hamburg, 2004.

[2] The Tesla Test Facility Team. SASE FEL at the TESLA Test Facility, Phase 2. TESLA-FEL 01-2002, DESY Print, 2002.

[3] E. L. Saldin, E. A. Schneidmiller, and M. V. Yurkov. *The Physics of Free-electron Lasers*. Springer, Berlin, Heidelberg, 2000.

[4] Henry N. Chapman, et al. Femtosecond diffractive imaging with a soft-X-ray free-electron laser. *nature physics*, 2006.

[5] Markus Hühning. *Selbstoptimierende Parametersteuerung der Hochfrequenz des supraleitenden Linearbeschleunigers TESLA Test Facility*. Diplomarbeit, Rheinisch-Westfälische Technische Hochschule Aachen, 1998.

[6] Krzysztof Czuba. *RF Phase Reference Distribution System for the TESLA Technology Based Projects*. PhD thesis, Warsaw University of Technology, 2007.

[7] B. Aune, et al. The superconductive TESLA cavities. *Phys. Rev. ST-AB*, 2001.

[8] Thomas Schilcher. *Vector-sum Control of Pulsed Accelerating Field in Lorentz Force detuned Superconductive Cavities*. Doktorarbeit, Universität Hamburg, 1998.

[9] Alexander Brandt. *Development of a Finite State Machine for the Automated Operation of the LLRF Control at FLASH*. Doktorarbeit, Universität Hamburg, 2007.

[10] Matthias Liepe. *Regelung supraleitender Resonatoren mit Strahlbelastung am TESLA-Test-Linearbeschleuniger*. Diplomarbeit, Universität Hamburg, 1998.

[11] A. Mosnier. Dynamic Measurements of the Lorentz Forces on a MACSE cavity. TESLA 93-09, DESY Print, 1993.

[12] Przemyslaw Sekalski. *Smart Materials as Sensors and Actuators for Lorentz Force Tuning System*. PhD thesis, Technical University of Lódz, Poland, 2006.

[13] S. Simrock, F. Ludwig, and H. Schlarb. Synchronization systems for ERLs. *NIM A*, pages 557:293–298, 2006.

[14] O. Zinke and H. Brunswig. *Hochfrequenztechnik 2*. Springer, Berlin, Heidelberg, New York, 5th edition, 1999.

[15] David M. Pozar. *Microwave Engineering*. Wiley John & Sons, 3rd edition, 2004.

[16] O. Zinke and H. Brunswig. *Hochfrequenztechnik 1*. Springer, Berlin, Heidelberg, New York, 6th edition, 2000.

[17] B. Schiek and H.-J. Siweris. *Rauschen in Hochfrequenzschaltungen*. Hüthig, Heidelberg, 1990.

[18] Walt Kester. *Analog-Digital Conversion*. Analog Devices, Inc., 2004.

[19] Enrico Rubiola. The Leeson effect - Phase noise in quasilinear oscillators. http://www.citebase.org/abstract?id=oai:arXiv.org:physics/0502143, 2005.

[20] Aeroflex Team. PN9000 Automated Phase Noise Measurement System. Application Note 1, Aeroflex, 2003.

[21] Kenneth V. Puglia. Phase Noise Analysis of Component Cascades. *IEEE Microwave Magazine*, 3:71–75, 2002.

[22] Enrico Rubiola. Tutorial on the double balanced mixer. http://www.citebase.org/abstract?id=oai:arXiv.org:physics/0608211, 2006.

[23] Frank Ludwig. *Nonlinear Dynamics and Far-Infrared Broadband Spetroscopy of YBa2Cu3O7 Josephson Junctions for the TESLA Test Facility Linac*. Doktorarbeit, Universität Hamburg, 2003.

[24] Charles L. Phillips and Roye D. Harbor. *Feedback Control Systems*. Prentice Hall, 2000.

[25] F. Ludwig, M. Hoffmann, H. Schlarb, and S. Simrock. Phase stability of the next generation RF field control for VUV- and X-Ray free electron laser. In *Proceedings of EPAC 2006, Edinburgh, Scotland*, 2006.

[26] Bastian Lorbeer. *Stability of the Master Oscillator for FLASH at DESY.* Studienarbeit, Technische Universität Hamburg-Harburg, 2006.

[27] F. Loehl,et al. A sub 100 fs electron bunch arrival-time monitor system for FLASH. In *Proceedings of EPAC 2006, Edinburgh, Scotland*, 2006.

[28] K. Hacker, F. Loehl, and H. Schlarb. Large horizontal aperture BPM for use in dispersive sections of magnetic chicanes. In *Proceedings of EPAC 2006, Edinburgh, Scotland*, 2006.

[29] H. Delsim-Hashemi, et al. Bunch compression monitor. In *Proceedings of EPAC 2006, Edinburgh, Scotland*, 2006.

[30] A. Mosnier and O. Napoly. Field stabilization study for TESLA. TESLA 94-16, DESY Print, 1994.

[31] B. Brannon and A. Barlow. Aperture uncertainty and ADC system performance. Application Note AN-501, Analog Devices Inc., 2006.

[32] I. N. Bronstein and K. A. Semendjaev. *Taschenbuch der Mathematik.* Verlag Harri Deutsch, 5th edition, 2000.

[33] Hittite Microwave Corporation. www.hittite.com, 2007.

[34] Linear Technologies. www.linear.com, 2007.

[35] Analog Devices Inc. www.analog.com, 2007.

[36] TTE Incorporated. www.tte.com, 2007.

[37] Mini-Circuits. www.minicircuits.com, 2007.

[38] Linear Technology Corporation. LTC2207/LTC2206 - 16-Bit, 105MSPS/80MSPS ADCs. www.linear.com, 2006. Datasheet.

[39] P. Stockwell, D. Green, C. McNeilage, and J.H. Searls. A low phase noise 1.3 GHz Dielectric Resonator Oscillator. In *International Frequency Control Symposium and Exposition, IEEE*, pages 882–885, 2006.

[40] K. Suchecki, F. Ludwig, and M. Hoffmann. Mixer noise characterization. Internal lab report, DESY, 2006.

[41] C. Gerth. Synchrotron radiation monitor for energy spectrum measurements in the bunch compressor at FLASH. In *Proceedings of DIPAC 2007, Venice, Italy*, 2007.

Acknowledgments

First and foremost, I gratefully acknowledge the constant support and encouragement of my doctoral supervisor Prof. K. Schünemann on the part of Technische Universität Hamburg-Harburg.

Furthermore, I would like to express my gratitude towards my supervisor at DESY, Dr. S. Simrock for his mentoring.

For the provision of financing of this thesis, I would like to thank the Swiss Staatssekretariat für Bildung und Forschung (Bundesamt für Bildung und Wissenschaft[1]) and the EU support program CARE (Coordinated Accelerator Research in Europe)[2].

A special thanks goes to my colleagues, who supported me at all times. I am especially grateful to A. Brandt, F. Ludwig, M. Felber, C. Schmidt, H. Weddig, V. Ayvazyan, W. Koprek, G. Möller, W. Jalmuzna, P. Stralkowski, A. Antoniewicz, K. Suchecki, K. Czuba, B. Lorbeer, J. Müller, T. Traber, B. Wendland, M. Götz, T. Schilcher, V. Schlott and the colleagues of the FLA and MHF-p group.

Finally, I would like to thank my family for their understanding, endless patience and encouragement when it was most required.

Lebenslauf

Persönliche Daten:	
	Matthias Hoffmann, geb. Schrader
	geboren am 16. September 1978 in Berlin
	verheiratet

Schulausbildung:	
1998	Julius-Leber-Schule, Hamburg, Gymnasiale Oberstufe
	Abschluss: Abitur (2,4)

Studium:	
Okt. 1998 - Nov. 2003	Technische Universität Hamburg-Harburg
	Studiengang Elektrotechnik (Nachrichtentechnik)
	Abschluss mit der Note: Gut (2,0)
Okt. 2002 - März 2003	Fachpraktikum bei Sennheiser electronic
	Tätigkeitsfeld: Simulation und Modellierung von
	Hochfrequenzschaltungen und Komponenten
April. 2003 - Nov. 2003	Diplomarbeit bei Sennheiser electronic
	Thema: Simulation und Entwurf eines linearen
	UHF-Verstärkers in SiGe-LDMOS-Technik

Beruflicher Werdegang:	
Jan. 2004 - Juni 2007	Deutsches Elektronen-Synchrotron, Hamburg
	Wissenschaftliche Hilfskraft mit Hochschulabschluss
	zum Zwecke der Vorbereitung auf die Promotion
	Thema: Development of a multichannel RF field
	detector for the LLRF control at FLASH